MNRAS 000, 1–37 (2018) Preprint 20 March 2022 Compiled using MNRAS LATEX style file v3.0

The ASAS-SN Catalog of Variable Stars II: *Uniform Classification of 412,000 Known Variables*

T. Jayasinghe[1,2]★, K. Z. Stanek[1,2], C. S. Kochanek[1,2], B. J. Shappee[3], T. W. -S. Holoien[4], Todd A. Thompson[1,2], J. L. Prieto[5,6], Subo Dong[7], M. Pawlak[8], O. Pejcha[8], J. V. Shields[1], G. Pojmanski[9], S. Otero[10], C. A. Britt[11], D. Will[1,11]

[1] *Department of Astronomy, The Ohio State University, 140 West 18th Avenue, Columbus, OH 43210, USA*
[2] *Center for Cosmology and Astroparticle Physics, The Ohio State University, 191 W. Woodruff Avenue, Columbus, OH 43210, USA*
[3] *Institute for Astronomy, University of Hawaii, 2680 Woodlawn Drive, Honolulu, HI 96822,USA*
[4] *Carnegie Observatories, 813 Santa Barbara Street, Pasadena, CA 91101, USA*
[5] *Núcleo de Astronomía de la Facultad de Ingeniería y Ciencias, Universidad Diego Portales, Av. Ejército 441, Santiago, Chile*
[6] *Millennium Institute of Astrophysics, Santiago, Chile*
[7] *Kavli Institute for Astronomy and Astrophysics, Peking University, Yi He Yuan Road 5, Hai Dian District, China*
[8] *Institute of Theoretical Physics, Faculty of Mathematics and Physics, Charles University in Prague, Czech Republic*
[9] *Warsaw University Observatory, Al Ujazdowskie 4, 00-478 Warsaw, Poland*
[10] *The American Association of Variable Star Observers, 49 Bay State Road, Cambridge, MA 02138, USA*
[11] *ASC Technology Services, 433 Mendenhall Laboratory 125 South Oval Mall Columbus OH, 43210, USA*

arXiv:1809.07329v1 [astro-ph.SR] 19 Sep 2018

Accepted XXX. Received YYY; in original form ZZZ

ABSTRACT

The variable stars in the VSX catalog are derived from a multitude of inhomogeneous data sources and classification tools. This inhomogeneity complicates our understanding of variable star types, statistics, and properties, and it directly affects attempts to build training sets for current (and next) generation all-sky, time-domain surveys. We homogeneously analyze the ASAS-SN V-band light curves of ∼412,000 variables from the VSX catalog. The variables are classified using an updated random forest classifier with an F_1 score of 99.4% and refinement criteria for individual classifications. We have derived periods for ∼44,000 variables in the VSX catalog that lack a period, and have reclassified ∼17,000 sources into new broad variability groups with high confidence. We have also reclassified ∼94,000 known variables with miscellaneous/generic classifications. The light curves, classifications, and a range of properties of the variables are all available through the ASAS-SN variable stars database (https://asas-sn.osu.edu/variables). We also include the V-band light curves for a set of ∼4,000 rare variables and transient sources, including cataclysmic variables, symbiotic binaries and flare stars.

Key words: stars:variables – stars:binaries:eclipsing – catalogues –surveys

1 INTRODUCTION

It is difficult to pinpoint the exact origin of the study of variable stars. Astronomy is the oldest natural science, and many ancient cultures carefully observed celestial objects. Records of transient sources such as supernovae date back to 185 AD, but variable sources are different in the sense that they persist over human lifetimes, rather than disappearing after a short while. It has been suggested that the ancient Egyptians first noted the variability of Algol, an eclipsing binary, over 3000 years ago (Jetsu et al. 2013). Recently, it has even been claimed that aboriginal Australians observed the variability of pulsating red giants long ago and incorporated this discovery into their culture and lore (Hamacher 2018) . This is not difficult to believe as the large variability amplitudes of pulsating red giants make them easy targets for visual, naked-eye observation (Schaefer 2018). It is possible that many other ancient cultures recorded the variability of bright sources without any record of it surviving to the modern day.

The first modern discovery of a periodic variable was made in 1638, when Johannes Holwarda recorded the peri-

★ E-mail: jayasinghearachchilage.1@osu.edu

© 2018 The Authors

odicity of the Mira variable Omicron Ceti. The number of known variable stars gradually increased to ~12 by 1786, ~175 by 1890, ~4000 by 1912 and ~28450 by 1983 (Roth 1994). In the modern era, surveys such as the All-Sky Automated Survey for SuperNovae (ASAS-SN, Shappee et al. 2014; Kochanek et al. 2017; Jayasinghe et al. 2018a,c), the All-Sky Automated Survey (ASAS; Pojmanski 2002), the Optical Gravitational Lensing Experiment (OGLE; Udalski 2003), the Northern Sky Variability Survey (NSVS; Woźniak et al. 2004), MACHO (Alcock et al. 1997), EROS (Derue et al. 2002), the Catalina Real-Time Transient Survey (CRTS; Drake et al. 2014), the Asteroid Terrestrial-impact Last Alert System (ATLAS; Tonry et al. 2018; Heinze et al. 2018), and Gaia (Gaia Collaboration et al. 2018a; Holl et al. 2018; Gaia Collaboration et al. 2018b) have collectively discovered $\gtrsim 10^6$ variables in the span of ~20 years.

ASAS-SN monitors the entire visible sky to a depth of $V \lesssim 17$ mag. The ASAS-SN V-band data used in this study were obtained on a cadence of 2-3 days, but with the addition of 3 new g-band units ASAS-SN has significantly improved its cadence to $\lesssim 1$ day. The ASAS-SN telescopes are hosted by the Las Cumbres Observatory (LCO; Brown et al. 2013) in Hawaii, Chile, Texas and South Africa. While ASAS-SN focuses on the detection of bright supernovae (e.g., Holoien et al. 2017), and other transients (e.g., Tucker et al. 2018; Rodríguez et al. 2018), we simultaneously build up well-sampled light curves for $\gtrsim 50$ million bright ($V < 17$ mag) sources across the whole sky. In Paper I (Jayasinghe et al. 2018a), we identified ~66,000 new variables, most of which are located in regions close to the Galactic plane or Celestial poles which were not well-sampled by previous surveys.

Existing catalogs of variable stars have been derived from a multitude of inhomogeneous data sources and classification tools. This inhomogeneity proves to be a challenge when analyzing populations of variable stars and directly affects the current (and next generation) of all-sky time domain surveys. The OGLE survey provides an excellent catalog of homogeneously classified variable stars in the Magellanic clouds and the Galactic bulge, but an analogous, all-sky catalog of variable stars does not exist. In order to tackle this need, we homogeneously analyze a sample of known variables in this work. While a more complete, all-sky search for variable stars in ASAS-SN is underway, known variables can provide an excellent training set for current and upcoming variability surveys if it can be homogenized.

Missions like the Transiting Exoplanet Survey Satellite (TESS; Ricker et al. 2015) are expected to produce a large numbers of high-quality light curves. For example, the TESS input catalog (TIC; Stassun et al. 2018) contains ~470 million sources. Outside of the 400,000 selected targets observed at a 2 min cadence, the remaining sources are observed with a cadence of 30 min. Each TESS sector will be observed for at least 27 days, thus one can expect each TESS light curve to consist of $\gtrsim 1300$ epochs. With such a short cadence, TESS light curves are expected to probe short period variability to great detail. On the other hand, it will be difficult or impossible for TESS to probe the long period variability of most sources. ASAS-SN provides complementary light curves, sampled at a cadence of $\sim 1-3$ days, to study variability at longer periods. For large scale time domain surveys like TESS, the need to automatically classify sources becomes critical. Crucial to most classification methods are a well-sampled, diverse and homogeneously analyzed *training set* of variables that can be used to 'teach' a classifier to identify new variable sources.

We extracted the ASAS-SN light curves of ~412,000 variable stars previously discovered by other surveys and in the VSX catalog. In this work, we homogeneously classify the entire sample. In Section §2, we discuss the ASAS-SN observations and data reduction procedure. Section §3 discusses the variability classification pipeline. It is based on random forest classification models with variability type refinements. We derive a training sample with sources from Paper I and a subset of the known VSX variables. In Section §4 we apply our variability classification pipeline to the sources that were not included in our training sample and discuss our approach to estimating variability amplitudes in Section §5. We discuss the overall catalog in Section §6 and present a summary of our work in Section §7.

2 OBSERVATIONS AND DATA REDUCTION

We started with list of previously discovered variables from the VSX (Watson et al. 2006) database available in April 2018. The VSX database contains over ~500,000 variables discovered by a large number of surveys and individuals and is the most complete all-sky catalog of known variables. At this time, variables from ATLAS (Heinze et al. 2018) and Gaia DR2 (Holl et al. 2018; Gaia Collaboration et al. 2018b) have not been included in the VSX catalog. We include the list of variables discovered by the Kilodegree Extremely Little Telescope (KELT; Oelkers et al. 2018; Pepper et al. 2007) and the ASAS-SN variables that are in the process of being included in the VSX catalog into our working list of variables. For now, we also remove transients (cataclysmic variables, flaring sources, etc.), sources hosting planets and very-low amplitude rotational variables (< 50 mmag) to arrive at a list of ~450,000 variable sources. Table 1 describes the different samples of variables referenced in this paper and the section where we discuss each sample.

The V-band observations made by the "Brutus" (Haleakala, Hawaii) and "Cassius" (CTIO, Chile) quadruple telescopes between 2013 and 2018 were used to produce the light curves for these sources. Each ASAS-SN field in the V-band has ~ 200-600 epochs of observation to a depth of $V \lesssim 17$ mag. Each camera has a field of view of 4.5 deg^2, the pixel scale is $8\farcs0$ and the FWHM is ~ 2 pixels. ASAS-SN saturates at $\sim 10-11$ mag (Kochanek et al. 2017).

The light curves used in this work were produced as described in Jayasinghe et al. (2018a). ASAS-SN data are analyzed using image subtraction (Alard & Lupton 1998; Alard 2000). The light curves were extracted using aperture photometry on the subtracted images using an aperture with a 2 pixel radius and the IRAF `apphot` package. Calibration was done using the AAVSO Photometric All-Sky Survey (APASS; Henden et al. 2015). Roughly, ~30,000 sources with < 30 V-band detections were removed from the list to leave us with ~420,000 variables. The light curve uncertainties were rescaled using a rescaling function and zero point offsets between the different cameras were corrected as described in Jayasinghe et al. (2018a).

Figure 1 illustrates the distribution of variables by their

Table 1. Descriptions of the different samples of variables used in this work.

Description	Number of Variables	Section
Starting VSX Catalog	~500, 000	§2
Selecting by the variability type and amplitude	~450, 000	§2
Selecting by the number of detections in the V-band (> 30 V-band detections)	~420, 000	§2
Training set for the V1 classifier (ASAS-SN variables from Paper I)	~66, 000	§3.3
Initial training set for the V2 classifier	~177, 000	§3.3
Final training set for the V2 classifier after classification refinement	~166, 000	§3.4, §3.5, §3.6
Variables with $11 < V < 17$ mag	~356, 000	§6.1
Variables with miscellaneous classifications	~94, 000	§4.1
OGLE variables in the VSX catalog	~52, 000	§4.2
Variables with low V1 classification probabilities	~47, 000	§4.3
Variables with definite classifications	~278, 000	§6.1
Variables with uncertain classifications	~78, 000	§6.1
Variables matched to Gaia DR2 variables	~23, 000	§6.4
Variables with Gaia DR2 A_G extinction and $E(BP-RP)$ reddening estimates	~169, 000	§6.5
Saturated/Faint VSX Variables	~56, 000	Appendix A
Variables classified by ASAS-SN	~412, 000	§6.1
Rare and transient variables	~4, 000	§6.2
Final catalog on the ASAS-SN Variable Stars Database	~416, 000	§6, §7

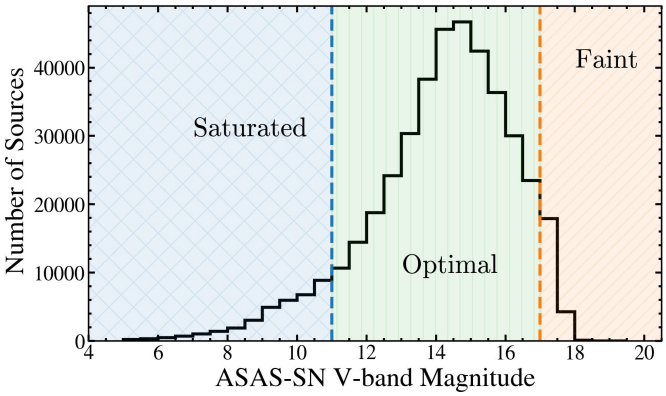

Figure 1. Distribution of variables in their average ASAS-SN V-band magnitude.

average V-band magnitude. In this work, we consider a variable to be saturated if $V \leq 11$ mag and faint if $V \geq 17$ mag. The optimal magnitude range for ASAS-SN is $11 < V < 17$ mag. We do not take into consideration blending/crowding effects when computing the average magnitudes. The main body of the paper focuses on the ~356, 000 variables with $11 < V < 17$ mag. In the Appendix we discuss the variables with $V \leq 11$ mag and $V \geq 17$ mag.

3 CONSTRUCTING A ROBUST VARIABILITY CLASSIFIER

Here we describe the procedure we used to construct a training set and develop a variability classification pipeline. In Section §3.1, we describe the cross-matches made to external catalogs. In Section §3.2, we describe the procedure we took to derive periods for these sources. In Section §3.3, we discuss the initial V1 random forest classifier model from Paper I and the steps we took to select variables for our training set. In Section §3.4, we describe our refinement criteria for the initial RF classifications and discuss our enhanced training set in section §3.5. We discuss our final V2 random forest classifier model in Section §3.6.

3.1 Cross-matches to external catalogs

We cross-matched the variables with Gaia DR2 (Gaia Collaboration et al. 2018a) using a matching radius of 5.″0. A significant fraction of these sources have large parallax errors and/or negative parallaxes, hence reliable distances cannot be derived. We utilize the probabilistic distance estimates from Bailer-Jones et al. (2018) in our pipeline. Even poor distance estimates aid in classification because they generally indicate that the source has to be a distant giant rather than a nearby dwarf.

We also crossmatch the variables with 2MASS (Skrutskie et al. 2006) and AllWISE (Cutri et al. 2013; Wright et al. 2010) using a matching radius of 10.″0. This provides near-infrared, mid-infrared and optical colors for use in classification. We used `TOPCAT` (Taylor 2005) both to query the Gaia DR2 database, and to cross-match our sources with the 2MASS and AllWISE catalogs .

3.2 Period Determination

Periods were derived for the ~420, 000 sources following the procedure described in Jayasinghe et al. (2018a). The Generalized Lombe-Scargle (GLS, Zechmeister & Kürster 2009; Scargle 1982), the Multi-Harmonic Analysis Of Variance (MHAOV, Schwarzenberg-Czerny 1996), and the Box Least Squares (BLS, Kovács et al. 2002) periodograms were used to search for periodicity. We use the `astrobase` implementation of the GLS, BLS and MHAOV periodograms (Bhatti et al. 2018). The `astropy` implementation of the GLS algo-

rithm (Astropy Collaboration et al. 2013) was used to derive the window function for each light curve.

In order to minimize the effect of outliers during the period search, we clip the light curve data to select only the epochs with magnitudes between the 1st and 99th percentiles. Periods were searched over the range $0.05 \leq P \leq 1000$ days. We initialized the MHAOV periodogram with $N_{harm} = 5$ harmonics to provide better sensitivity to complex variability signals, while the BLS periodogram was initialized with 200 phase bins and a minimum (maximum) transit duration of 0.1 (0.3) in phase. The 5 best periods from each periodogram were saved. BLS periods were only selected if the BLS power was < 0.3.

The observed periodogram for a given light curve is the convolution of a window function that depends on the survey and the 'true' periodogram (see the discussion in VanderPlas 2018). Ideally, one would want to retrieve the true periodogram by deconvolution, but this is difficult to achieve in practice. A good method to identify potentially false periodicity is to examine the window function. The Lombe-Scargle window function (Astropy Collaboration et al. 2013) is found using a light curve with the same temporal sampling as the data but with the magnitude measurements set to a constant. The 10 strongest peaks in this window function are saved and are considered to be the possible aliased periods for the light curve.

Comparisons of the window function and the GLS periodogram for the RRAB variable ASASSN-V J102525.66+284707.1 (top panel) and the irregular variable ASASSN-V J005200.56+404837.9 (bottom panel) are shown in Figure 2. The false alarm probability (FAP) levels corresponding to 1×10^{-5} and 1×10^{-15} are also shown. The false alarm probability is an estimate of the probability that a light curve with no periodicity results in a periodogram peak of a given power and it is a good indicator of the significance of a periodogram peak. In the case of strongly periodic variables like ASASSN-V J102525.66+284707.1, we see that the underlying window function is suppressed and the true period of P = 0.5439 d dominates the periodogram peaks. For irregular sources and sources with weak periodicity like ASASSN-V J005200.56+404837.9, the window function can dominate the observed periodogram and result in aliases being retrieved as periods.

After running the GLS, BLS and MHAOV periodograms, we have 15 possible periods. To select the best period from these 15 periods, we used the `gatspy` implementation of the Supersmoother algorithm (Vanderplas 2015; Reimann 1994). Supersmoother is an algorithm that performs nonparametric regression based on local linear regression with adaptive bandwidths (Reimann 1994). Each of the retrieved periods are compared with the aliases derived from the associated window function, and those periods within 10^{-3} of an alias and with a FAP $< 1 \times 10^{-15}$ are removed from consideration. We generate a Supersmoother fit to the light curve and calculate the Supersmoother model score from `gatspy` for each of the remaining periods. The period with the highest Supersmoother score is chosen as the best period. We use the Supersmoother model to further refine this period within a range $0.995\,\mathrm{P_{best}} \leq \mathrm{P} \leq 1.005\,\mathrm{P_{best}}$. We find that this approach generally works well, except in cases where the Supersmoother model prefers a multiple of the true period over the true period. We will identify and correct most of these cases in §3.4.

We refined this process of period selection using the Lafler-Kinmann string length statistic (Lafler & Kinman 1965; Clarke 2002). We use the definitions of

$$\Theta(P) = \frac{\sum_{i=1}^{N}(m_{i+1} - m_i)^2}{\sum_{i=1}^{N}(m_i - \overline{m})^2}, \quad (1)$$

and

$$T(\phi|P) = \Theta(P) \times \frac{(N-1)}{2N} \quad (2)$$

from Clarke (2002) where the m_i are the magnitudes sorted by phase and $\overline{m}$ is the mean magnitude. The original Lafler-Kinmann string length statistic ($\Theta(P)$) is derived using the sum of the squares of the vector lengths required to connect re-ordered measurements in phase sequence (Clarke 2002). This is scaled by a factor of $(N-1)/2N$ to normalize the result and remove sample-size bias (Clarke 2002), resulting in the $T(\phi|P)$ statistic used in this work. We use $T(\phi|P)$ to assign a score to each period after sorting the light curve by ascending phase.

Aliases are removed in a similar fashion to the Supersmoother approach, but the tolerance was made absolute and allowed to vary based on the period being tested. For $0.05 \leq P \leq 10$ d, tol = 0.005 d, for $10 \leq P \leq 300$ d, tol = 0.05 d, and for $P > 300$ d, tol = 1 d. The best period in this case is the period with the smallest $T(\phi|P)$.

We also use the Gaia DR2 $G_{BP} - G_{RP}$ color and $T(t)$ calculated on the light curves as in equations 1 and 2 but with the data ordered by time instead of phase to rule out shorter periods for redder, long period variables (LPVs). $T(t)$ is sensitive to the structure and clustering of sorted data points. For the unphased light curves of variables with short periods, $T(t)$ is larger (worse) than for the unphased light curves of LPVs. We can rule out short periods ($P < 25$ d) for LPVs by using their location on the $T(t)$ vs. $G_{BP} - G_{RP}$ diagram (Figure 3). Periods shorter than 25 d are only allowed for the variables falling into the red shaded region. This process effectively eliminates the common aliases of a sidereal day that are frequently found for the light curves of red, irregular variable sources.

3.3 Initial Random Forest Classification

We built a variability classifier in Paper I based on a random forest model using `scikit-learn` (Pedregosa et al. 2012; Breiman 2001). We will refer to this as the V1 classifier. The set of variables used to train this classifier consisted of ~56,000 variables that passed visual inspection of their light curves. We augmented this classifier with the remaining ~10,000 variables in Paper I to increase the diversity of our training set from Paper I. The goal was to provide general classifications into broad groups: CEPH (Cepheids), RRAB (RR Lyrae, type ab), RRC/RRD (RR Lyrae, types c/d), SR/IRR (Semi-regular/irregular variables), M (Mira variables), DSCT (DSCT/HADS variables) and ECL (Eclipsing Binaries). These broad classes were selected to reduce the complexity of the classifier, and to provide an accurate initial classification prior to refining classifications in the next stages.

We choose a sample of known variables with optimal

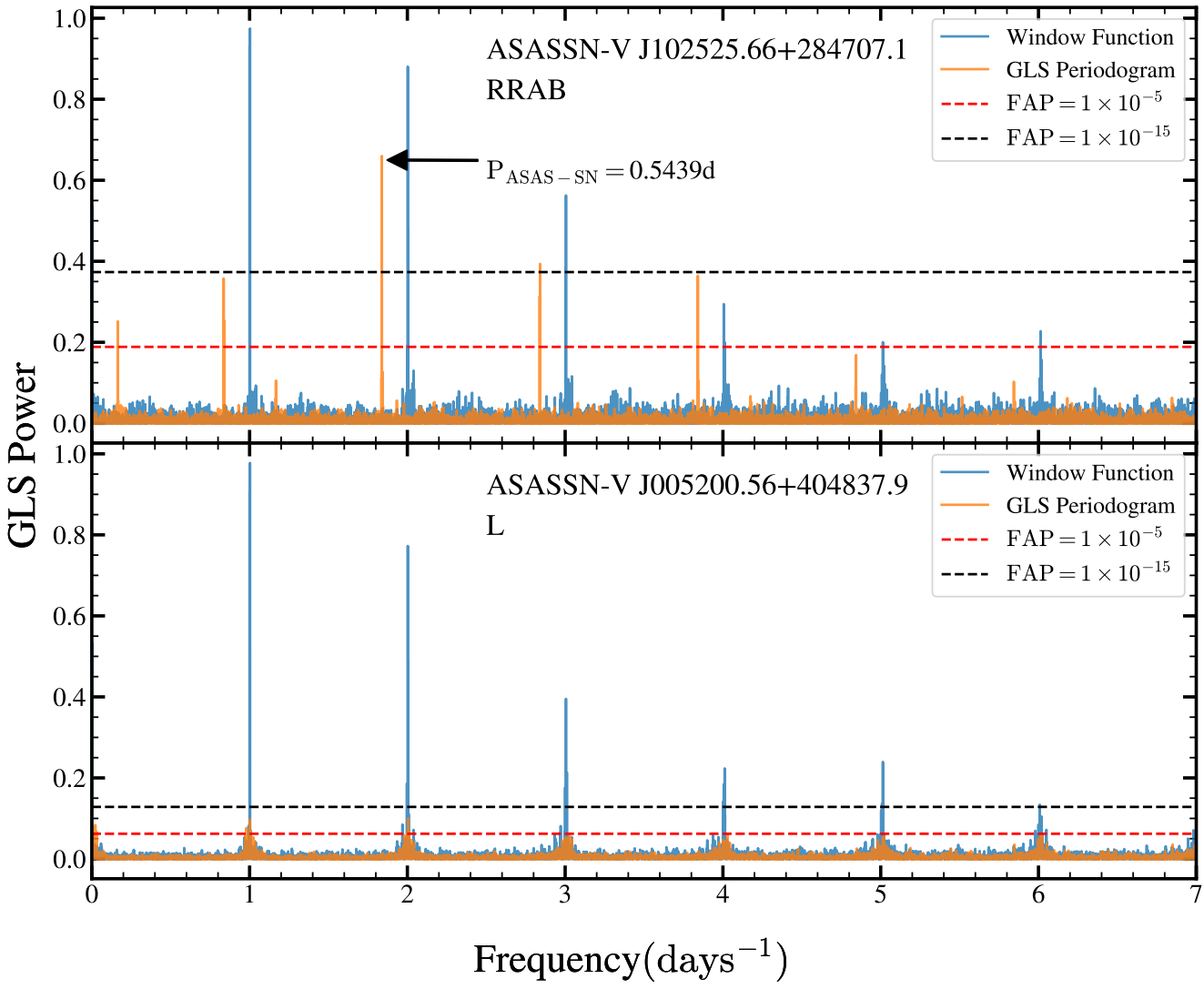

Figure 2. The GLS periodogram (gold) and the associated window function (blue) for the RRAB variable ASASSN-V J102525.66+284707.1 (top) and the irregular variable ASASSN-V J005200.56+404837.9 (bottom). The best period of P = 0.5439 d for ASASSN-V J102525.66+284707.1 is marked, along with the false alarm probability levels corresponding to 1×10^{-5} (red) and 1×10^{-15} (black).

ASAS-SN magnitudes ($11 \leq V \leq 17$) for classification with the V1 random forest classifier. Sources with an OGLE identifier in their name were not selected at this point, and are classified later. To this sample of variables, we fit a Fourier model of variable order,

$$M(\phi) = m_0 + \sum_{i=1}^{N} (a_i \sin(2\pi i\phi) + b_i \cos(2\pi i\phi)) \quad (3)$$

where m_0 is fixed to be the median magnitude for each source, $4 \leq N \leq 16$ is the order of the Fourier model and ϕ is the phase at a given epoch. The amplitude of the ith harmonic is $A_i = (a_i^2 + b_i^2)^{1/2}$ and the phase angle is $\Phi_i = \tan^{-1}(-b_i/a_i)$. We define the amplitude ratios of the harmonics as $R_{ij} = A_i/A_j$ and the difference in phase angle between two harmonics as $\Phi_{ij} = \Phi_i - i\Phi_j$. The best fit Fourier model of order $N_{\rm best}$ is the Fourier model that minimizes $\chi^2_{\rm DOF}$. Through this process, we find that a Fourier model of order 6 is sufficient to describe most periodic variables and provide features for classification. During this initial round of classification, we derived distances by simply inverting the Gaia DR2 parallax. In the cases with very large parallax uncertainties, and/or negative parallaxes, an arbitrarily large integer was assigned to the distance to signify that they are very distant. Distance estimates from Bailer-Jones et al. (2018) are used in the V2 classifier (Section §3.6). The complete list of features and their importances in the random forest classifier are summarized in Table 2. Feature importances are calculated using the mean decrease impurity algorithm (Gini importances) implemented in the `scikit-learn` version of the Random Forest Classifier (Pedregosa et al. 2012). Compared to the RF classifier from Paper I, we introduced 12 new Fourier features (a_2, a_4, b_2, b_4, R_{41}, R_{32}, R_{42}, R_{43}, Φ_{41}, Φ_{21}, $N_{\rm best}$ and $\chi^2_{\rm DOF}$) and 11 other features ($1/\eta$, σ, MAD, $1/\eta$, $m_{\rm slope}$, $J-K_s$, $G_{BP}-G_{RP}$, $W1-W2$,

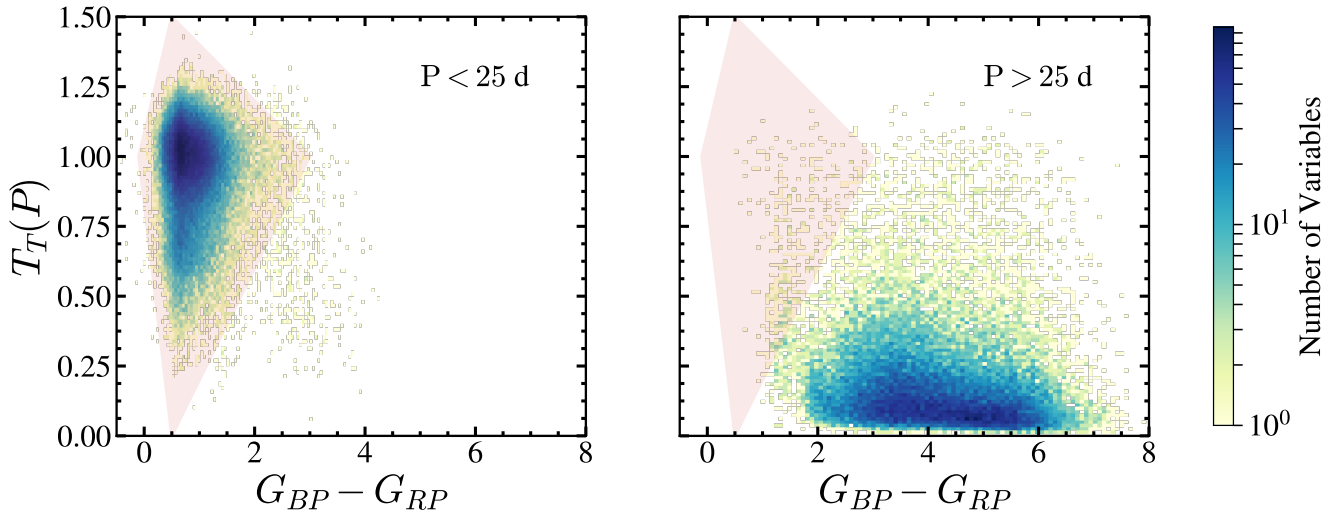

Figure 3. $T(t)$ for short period variables (P < 5 d, left) and long period variables (right) as a function of the Gaia DR2 $G_{BP} - G_{RP}$ color. The selection region for short period variables is shaded in red.

M_G, $W_{\rm RP}$ and W_{JK}) in this work. We set the number of decision trees in the forest as `n_estimators=800`, pruned the trees at a maximum depth of `max_depth=16` to prevent overfitting, set the number of samples needed to split a node as `min_samples_split=10` and set the number of samples at a leaf node as `min_samples_leaf=5`. To further reduce overfitting, weights were assigned to each class by initializing `class_weight='balanced_subsample'`.

The overall results can be evaluated based on the

$$\text{precision} = \frac{\alpha}{\alpha + \beta}, \tag{4}$$

$$\text{recall} = \frac{\alpha}{\alpha + \gamma}, \tag{5}$$

and the harmonic mean of the two,

$$F_1 = 2\left(\frac{\text{precision} \times \text{recall}}{\text{precision} + \text{recall}}\right), \tag{6}$$

where α, β and γ are the number of true positives, false positives and false negatives respectively. The sample of ASAS-SN variables from paper I were split for training (80%) and testing (20%) in order to evaluate the performance of the RF classifier. The performance of the classifier is summarized in Table 3. We noted that this version of the classifier needed improvement, particularly for the CEPH, ROT and RRC/RRD classes. We suspect that this is due to the small number of these variables in our Paper I training set. The classification of sources into the remaining classes is accurate enough for our purposes. The overall F_1 score for version V1 of the classifier is 93.3%.

We want to apply this version of the classifier to the ~150,000 other VSX variables with $11 < V < 17$ and VSX classifications that could be explicitly matched with the outputs of our classifier. For example, we do not include objects with MISC/VAR classifications. We first select ~110,000 variables where the VSX and V1 classifications agree. Next, we compare the ASAS-SN periods and the VSX periods. If any of the periods retrieved from the ASAS-SN light curve are comparable to the VSX period to a tolerance $\Delta P/P_{\rm VSX}$ given in Table 4, and depending on the variable class, we assign that ASAS-SN period as the best period for the source. The tolerance was made to vary by variable class due to the differences in periodicity amongst the different variable types. Certain semi-regular variables, rotational variables and Mira variables tend to have poorly defined periods, and in some cases display changes in their period over time. These classes were given a higher matching tolerance to account for this behavior.

In the case of eclipsing binaries, we also check to see if a multiple of the VSX period is retrieved, and in such cases, we correct the ASAS-SN period by multiplying it by the appropriate constant. We report the results of the period matching as well as the number of sources in this sample of variables without an associated VSX period in Table 4. The ~94,000 variables that have matching classes and matching periods are assumed to be good. The ~11,000 variables with matching classes and discrepant periods were visually reviewed to verify or correct the new periods before including them in the training sample.

There were ~39,000 variables with discrepant classifications. For these objects, we kept those with V1 classification probabilities of Prob > 0.5 for $|b| > 25$ deg and Prob > 0.7 for $|b| < 25$ deg. The Galactic latitude is included because crowding and blending will be an increasing problem for ASAS-SN at low latitudes. This left ~9,000 variables which we visually inspected and corrected (46%), remained unchanged (19%) or dropped (35%). This added ~5,000 additional variables to the training sample.

These procedures provide us with a first pass at a new training set of ~177,000 sources, including ~66,000 ASAS-SN variables. To build V2 of the classifier, we will first refine these classifications using light curve characteristics, distance measurements from Bailer-Jones et al. (2018) and multi-band photometry from Gaia DR2, 2MASS and WISE (Gaia Collaboration et al. 2018a; Skrutskie et al. 2006; Cutri et al. 2013; Wright et al. 2010).

Table 2. Variability features and their importances across the two versions of the ASAS-SN random forest variability classifier

Feature	Description	V1 Importance	V2 Importance	Reference
logP	Base 10 logarithm of the period	18%	25%	-
$J-K_s$	2MASS $J-K_s$ color	9%	5%	Skrutskie et al. (2006)
$J-H$	2MASS $J-H$ color	-	7%	Skrutskie et al. (2006)
$G_{BP}-G_{RP}$	Gaia DR2 $G_{BP}-G_{RP}$ color	8%	5%	Gaia Collaboration et al. (2018a)
$W1-W2$	WISE $W1-W2$ color	-	0%	Cutri et al. (2013); Wright et al. (2010)
M_G	Absolute Gaia DR2 G-band magnitude	7%	-	Bailer-Jones et al. (2018); Gaia Collaboration et al. (2018a)
W_{RP}	Absolute Wesenheit Gaia DR2 G_{RP}-band magnitude	-	8%	Bailer-Jones et al. (2018); Skrutskie et al. (2006); Madore (1982)
W_{JK}	Absolute Wesenheit 2MASS K_s-band magnitude	-	6%	Bailer-Jones et al. (2018); Skrutskie et al. (2006); Madore (1982)
a_2	Fourier component a_2	1%	-	-
b_2	Fourier component b_2	1%	-	-
a_4	Fourier component a_4	1%	-	-
b_4	Fourier component b_4	0%	-	-
R_{41}	Ratio between the amplitudes of the 4th and 1st harmonics	2%	4%	-
R_{31}	Ratio between the amplitudes of the 3rd and 1st harmonics	2%	3%	-
R_{21}	Ratio between the amplitudes of the 2nd and 1st harmonics	3%	9%	-
R_{32}	Ratio between the amplitudes of the 3rd and 2nd harmonics	1%	-	-
R_{42}	Ratio between the amplitudes of the 4th and 2nd harmonics	1%	-	-
R_{43}	Ratio between the amplitudes of the 4th and 3rd harmonics	1%	-	-
Φ_{41}	Difference between the phase angle of the 4th and 1st harmonics	1%	-	-
Φ_{31}	Difference between the phase angle of the 3rd and 1st harmonics	1%	-	-
Φ_{21}	Difference between the phase angle of the 2nd and 1st harmonics	2%	-	-
$N_{\rm best}$	Best fit order of the Fourier model	0%	-	-
$\chi^2_{\rm DOF}$	Reduced χ^2 statistic of the best fit Fourier model	2%	-	-
A	Amplitude of the light curve (between the 5th and 95th percentiles)	7%	6%	-
Skew	Skewness of the magnitude distribution	5%	3%	-
Kurt	Kurtosis of the magnitude distribution	3%	-	-
T_m	M-test statistic	3%	-	Kinemuchi et al. (2006)
IQR	Difference between the 75th and 25th percentiles in magnitude	6%	3%	-
$A_{\rm HL}$	Ratio of magnitudes brighter or fainter than the average	6%	3%	Kim & Bailer-Jones (2016)
rms	Root-mean-square statistic of the light curve	7%	5%	-
σ	Standard deviation of the light curve	-	4%	-
MAD	Median absolute deviation of the light curve	-	4%	-
$1/\eta$	Inverse of the η (Von Neumann index) value for the light curve	4%	-	Von Neumann et al. (1941)
$m_{\rm slope}$	Slope of a linear fit to the light curve	1%	-	-

Table 3. Performance of the ASAS-SN random forest classifiers

Class	V1 Precision	V1 Recall	V1 F_1 score	V2 Precision	V2 Recall	V2 F_1 score
δ Scuti	94%	94%	94%	100%	100%	100%
RR Lyrae (Type ab)	97%	99%	98%	100%	100%	100%
RR Lyrae (Types c and d)	90%	92%	91%	99%	99%	99%
Cepheids	100%	70%	82%	99%	100%	99%
Eclipsing Binaries	98%	98%	98%	100%	100%	100%
Semi-regular/Irregular variables	100%	100%	100%	100%	100%	100%
Rotational variables	82%	95%	88%	97%	100%	98%
Mira	95%	100%	97%	98%	100%	99%

Table 4. Tolerance when matching periods. The percentage of matching periods and discrepancies given the corresponding tolerance are reported. The number of sources that lack a VSX period in each variability group are also listed.

Class	Tolerance ($\Delta P/P_{\rm VSX}$)	Matches	Discrepancies	Unreported VSX periods
δ Scuti	0.001%	55%	45%	26
RR Lyrae (Type ab)	5%	99%	1%	760
RR Lyrae (Types c and d)	5%	99%	1%	56
Cepheids	5%	100%	0%	9
Eclipsing Binaries	0.1%	93%	7%	906
Semi-regular/Irregular variables	25%	79%	21%	9374
Rotational variables	20%	79%	21%	74
Mira	25%	91%	9%	406

3.4 Refining Classifications

While the initial classifications assigned by the RF classifier are generally accurate, we are able to correct some misclassifications and refine some of the broad groups into sub-types using the period, light curve statistics, colors, photometry from external catalogs and distance measurements. We apply these both to the updated training set and to the final sample. Distance estimates from Bailer-Jones et al. (2018) were used to derive absolute magnitudes during the refinement process. To account for interstellar extinction in the absolute Gaia DR2 G_{RP} and 2MASS K_s band magnitudes, we use the reddening-free Wesenheit magnitudes (Madore 1982; Lebzelter et al. 2018)

$$W_{RP} = M_{\rm G_{RP}} - 1.3(G_{BP} - G_{RP}), \quad (7)$$

and

$$W_{JK} = M_{\rm K_s} - 0.686(J - K_s) \quad (8)$$

instead of the uncorrected absolute magnitudes in V2 of the RF classifier and the classification refinement process. A similar reddening-free formulation of color requires at least 3 different photometric measurements. This is difficult to do with just the two Gaia DR2 bands (G_{BP} and G_{RP}), thus we do not use reddening-free colors in this work. However, we discuss the effects of extinction on color and the ASAS-SN classifications in Section §6.5.

Here we discuss the refinement criteria used on the different broad groups that are assigned to the variables classified with the RF classifier.

3.4.1 Delta Scuti

δ Scuti stars pulsate at high frequencies (P< 0.3 d) and are located towards the lower end of the instability strip (Breger 1979). δ Scuti variables are also known to follow a period-luminosity relationship (Lopez de Coca et al. 1990). High amplitude δ Scuti variables (HADS) are a sub-type of the δ Scuti stars that have amplitudes $A > 0.15$ mag. HADS variables are more commonly discovered by sky surveys like ASAS-SN than the lower amplitude DSCT variables.

To refine the HADS/DSCT classifications, we use the period-luminosity relation (PLR) in absolute Wesenheit W_{JK} magnitude (Figure 4). A common classification error that reduces the purity of the HADS/DSCT sample is when contact eclipsing binaries at half their true period are mistaken for HADS/DSCT variables. This commonly happens in the period range $0.1 \leq$ P ≤ 0.25 d. In the period-luminosity diagram, it is easy to distinguish the two variable types. Contact eclipsing binaries (EW) have a tight PLR (Chen et al. 2018) and are fainter than the HADS/DSCT at any given period. Therefore, contact eclipsing binaries with half their true periods form a fainter PLR locus than the HADS/DSCT PLR (left panel in Figure 4). We empirically isolate the misclassified EW variables in W_{JK} vs. $\log$P space. We double their periods and change their classifications. After doubling the periods, these variables fall along the well-defined EW PLR (Right panel in Figure 4).

In a few cases, the RF classifier assigns longer period RR Lyrae to the DSCT class. We reclassify longer period variables ($P > 0.25$ d) in the DSCT class into one of the RR Lyrae sub-types (RRAB/RRC) depending on their period. Sources that do not lie on an empirically defined locus for valid HADS/DSCT sources are assigned an uncertainty flag (i.e., DSCT:).

3.4.2 RR Lyrae

RR Lyrae stars are sub-divided as RRAB, RRC and RRD variables. RRAB variables are fundamental mode, high am-

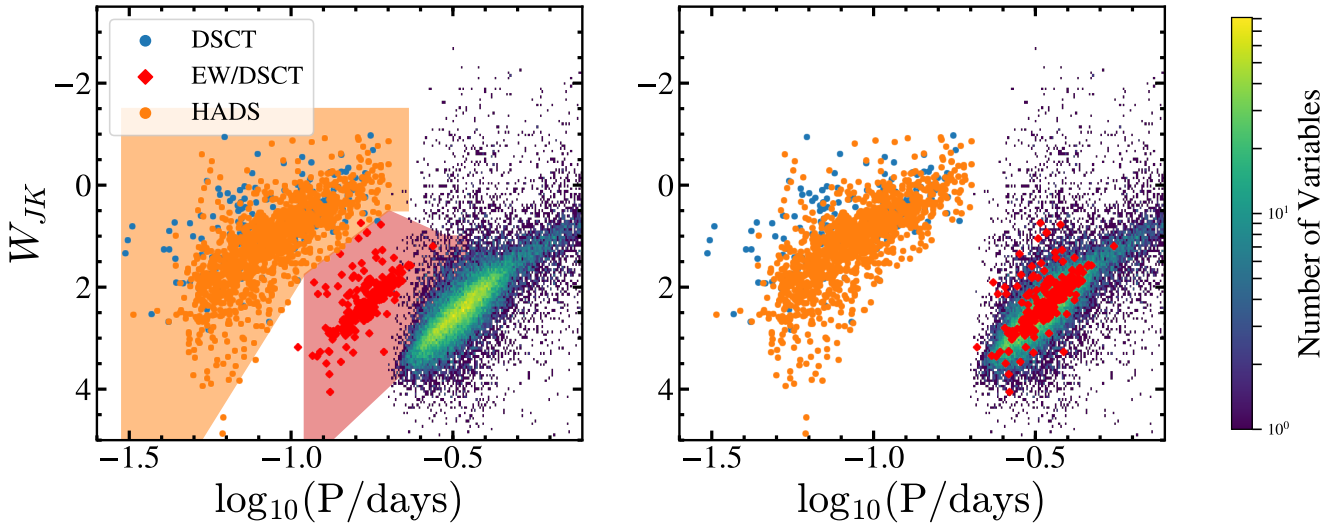

Figure 4. The PLR for δ Scuti variables (HADS as orange, DSCT as blue) and EW eclipsing binaries (blue to yellow density shading) in the absolute W_{JK} Wesenheit magnitude. The red points in the left panel are EW binaries given half of their correct period and then misidentified as HADS variables. We take objects in the red shaded region and double their periods, which moves them into the locus of EW binaries (right panel).

plitude pulsators with typical periods in the range 0.3 ≤ P ≤ 1.2 d. RRC variables are overtone pulsators with nearly symmetric light curves and have typical periods in the range 0.2 ≤ P ≤ 0.5 d. RRD variables are double-mode radial pulsators with fundamental periods P_{FO}~0.5 d and period ratios in the range 0.742 < P_{1O}/P_{FO} < 0.748 (Poleski 2014). The light curves of RRD variables are less regular due to the presence of both the fundamental and overtone modes of pulsation.

We discussed the issue of cross-contamination between RRC variables and short period contact binaries (EW) in Paper I. Using the period-luminosity space to distinguish between RRC variables and EW variables is difficult since the probabilistic distances to RR Lyrae stars from Bailer-Jones et al. (2018) have such a broad distribution in W_{JK} that many RR Lyrae overlap with the PLR for EW variables. Instead we look at the W_{RP} vs. G_{BP} - G_{RP} color-magnitude space to separate these variables (Figure 5). The EW variables have a tight relationship in the W_{RP} vs. G_{BP} - G_{RP} color-magnitude space which is distinct from the distribution of RRC variables beyond G_{BP} - G_{RP}~0.5 mag. We empirically isolate the locus of EW binaries in this color-magnitude space to identify misclassified RRC variables. We change the classification of the RRC variables that fall in this region to EW and double their periods. These misclassified sources then lie on the contact binary PLR (right panel in Figure 5).

To identify RRD candidates, we searched all the sources classified as RRAB/RRC for secondary periods, and those with period ratios 0.72 < P_{1O}/P_{FO} < 0.78 were classified as RRD variables. We also require that the fundamental period lie in the range 0.45 < P_{FO} < 0.60 d. As in Paper I, we chose this range in P_{1O}/P_{FO} to account for variations observed in RRD populations (Olech & Moskalik 2009) and dispersion due to noise. We report the fundamental period for all the RRD candidates.

There is likely some cross-contamination between RRAB and RRC variables in the period range 0.3 ≤ P ≤ 0.5 d. RRAB variables in crowded regions will tend to have lower amplitudes as result of blending, and therefore have a non-negligible chance of being classified as RRC variables owing to their smaller amplitudes.

We also check all the RRAB variables with $P > 1$ ($P > 0.9$) d to see if they follow the PLR for Classical (Type II Cepheids) respectively. RRAB variables falling into these PLR locii have their classifications changed to reflect their correct type.

To further improve the purity of the RRAB and RRC samples, we require $-3 < W_{JK} < 5$ mag in order to account for the large observed dispersion in absolute Wesenheit magnitudes, and that the RRAB/RRC variables follow the period constraints mentioned above. Uncertain classifications are followed by a ':' (i.e., RRAB: and RRC:). RR Lyrae with uncertain classifications may include sources without Gaia DR2 data. RRAB/RRC sources with $P < 0.2$ d are reclassified as HADS/DSCT/EW through the DSCT classification routine.

3.4.3 Cepheids

Cepheids are pulsators that form an important rung in the distance ladder. The first Cepheids discovered in the Magellanic clouds numbered in the few hundreds (Leavitt 1908; Leavitt & Pickering 1912), but owing to the extensive modern sky surveys toward the Magellanic Clouds, close to 10,000 Cepheids (Soszyński et al. 2017) have now been identified. In the Milky Way, only ~1000 Cepheids were discovered by 2011 (Windmark et al. 2011), but thanks to recent variability studies, there are now ~2100 (Clementini et al. 2018).

Fundamental mode Cepheids (DCEP) obey a period-luminosity relation (Leavitt & Pickering 1912) and their

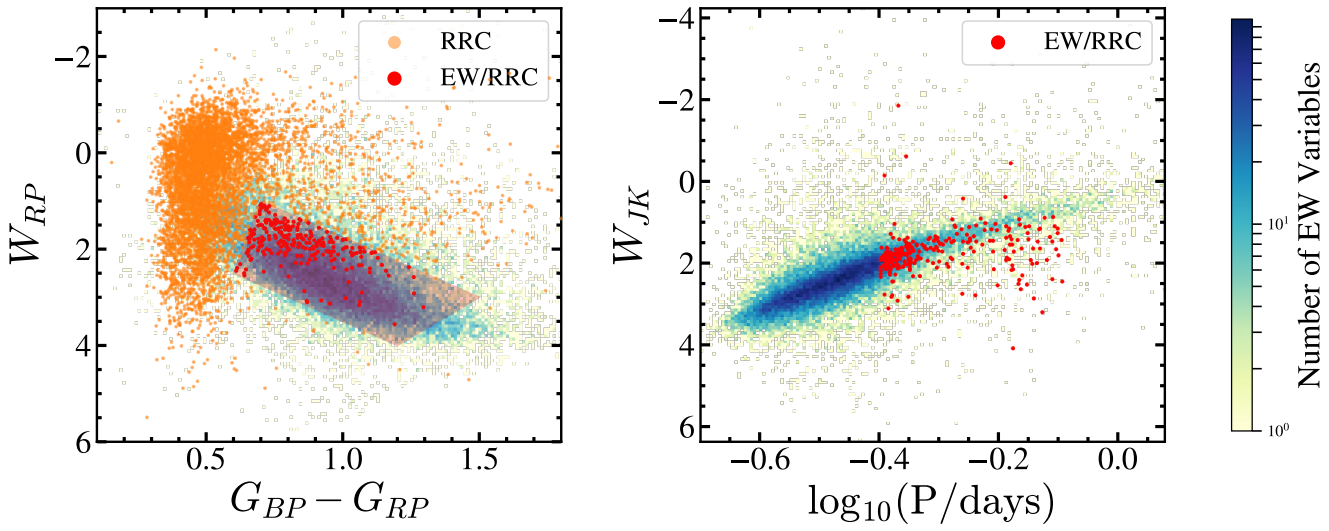

Figure 5. *Left*: The Wesenheit W_{RP} vs. G_{BP} - G_{RP} color-magnitude diagram for the RRC and EW variables. The locus of misclassified RRC variables is highlighted by the red shaded region. RRC variables whose classifications were changed to that of a contact eclipsing binary are shown in red. The color-magnitude relationship for the EW variables is plotted as a 2-d histogram (blue). *Right*: The W_{JK}-band PLR for the reclassified RRC variables after doubling the period. The distribution of the EW variables is shown as a 2-d histogram (blue).

light curve morphologies depend on the pulsation period (see for e.g., Pejcha & Kochanek 2012 for physically motivated multi-band light curve models for Cepheids). First overtone Cepheids (DCEPS) have periods $P < 7$ d and tend to have smaller variability amplitudes than a DCEP variable of the same period.

Type II Cepheids are intrinsically less luminous than classical Cepheids and commonly have light curves that are morphologically different from classical Cepheids at similar periods (e.g., Matsunaga et al. 2006). The type II Cepheids are categorized based on their periods: BL Herculis (CWB) variables have periods $P < 8$ d while W Virginis variables (CWA) have periods $P > 8$ d. RV Tauri variables (RVA/RVB) tend to have periods $30 < P < 150$ d and have alternating primary/secondary minima of different depths.

To classify Cepheids, we empirically group them into regions for Classical (red) and Type II (orange) pulsators (Figure 6). Previously derived PLRs for first overtone Cepheids (Baraffe & Alibert 2001), fundamental mode Cepheids (Storm et al. 2011) and Type II Cepheids (Matsunaga et al. 2006) are shown for reference. Cepheids are broadly classified into one of these two classes. Those variables classified as Cepheids that are less luminous than the Type II locus are classified as rotational variables (ROT).

In order to identify overtone pulsators, we look at the position of the Cepheids in the Fourier amplitude ratio R_{21} vs $\log P$ space (Figure 7). In this space, the DCEPS variables are well-separated from the fundamental mode DCEP variables. The overlapping CWB variables cause no problems because the PLRs distinguish the two classes.

We also looked more carefully for RV Tauri variables among the $P > 16$ d CWA and $P > 30$ d DCEP variables. We look for a minimum at phase ~0.5 in the light curve. If a minimum does not exist, we double the period. We then calculate the ratio between the secondary minimum at phase ~0.5 and the primary minimum at phase ~0 ($R_{\rm peaks}$). We call the source an RV Tauri variable if $R_{\rm peaks} < 0.9$, $A > 0.5$ mag and $16 \leq P \leq 180$ d. Cepheids that do not meet this criteria are reclassified into the CWA and DCEP groups. Periods are updated or halved based on the results of the automated period doubling.

We also suspected that RV Tauri variables are frequently classified as semi-regular variables. To examine this possibility, we ran all the semi-regular variables with classification probabilities Prob < 0.75, infrared colors $J - H < 1$ mag, amplitudes $A > 0.25$ mag, and periods $8 \leq P \leq 180$ d through the Cepheid pipeline. If the variable falls into the defined classical/Type II PLR regions, we change their classification to reflect their membership as Cepheids and then check to see if they are RV Tauri variables. RV Tauri variables of type b (RVB) are not distinguished from RV Tauri variables of type a (RVA). Examples of newly identified RV Tauri variables are shown in Figure 8.

A shortcoming of our Cepheid classification routine is the identification of anomalous Cepheids (ACEP). Anomalous Cepheids form PLRs (fundamental mode and overtone) with luminosities larger than CWB variables and less than DCEP variables of the same period. ACEP variables have periods $0.35 \leq P \leq 2.5$ d (Clementini et al. 2018), and therefore contaminate the RR Lyrae, CWB and DCEP classes. Some fraction of the short period CWB variables are indeed ACEP variables, but we have not implemented a classification scheme for these variables. Cepheids are largely located towards the Galactic disk and are likely to suffer from considerable reddening. This makes it a challenge to distinguish the PLRs of ACEPs from those of CWB and DCEP variables. In this context, it is also virtually impossible to distinguish short period ($P < 0.8$ d) overtone anomalous Cepheids

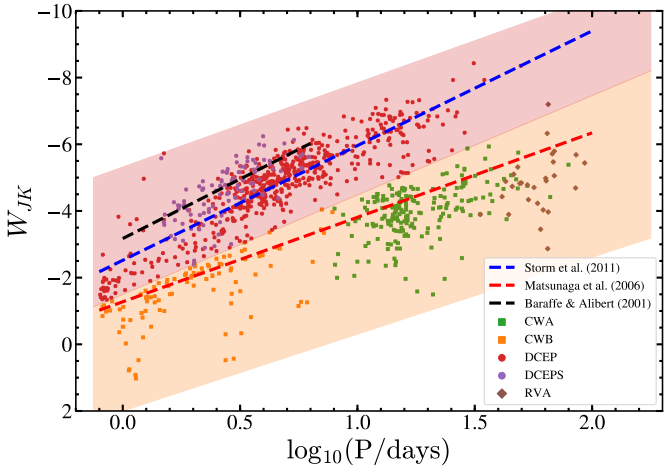

Figure 6. The Wesenheit W_{JK} magnitude PLR for Cepheids. The locus of classical Cepheids (both fundamental and overtone) is highlighted by the region shaded in red. The locus of Type II Cepheids is highlighted by the region shaded in orange. The Wesenheit W_{JK} magnitude PLR is plotted in black for first overtone Cepheids (Baraffe & Alibert 2001), in blue for classical fundamental mode Cepheids (Storm et al. 2011) and in red for Type II Cepheids (Matsunaga et al. 2006).

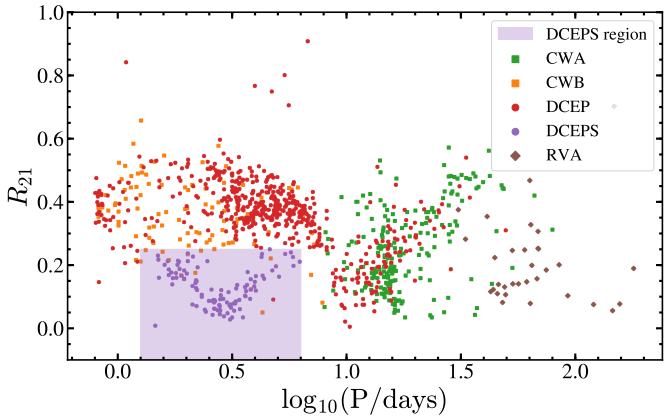

Figure 7. R_{21} vs log P for Cepheids. The points are colored according to the final classifications. The region occupied by first overtone Cepheids is shaded in purple.

toward the Galactic disk from RRC/RRAB variables without visual inspection of the light curves.

3.4.4 Rotational Variables

Rotational variables have light curves that show evidence of rotational modulation. We choose to retain the generic classification of ROT for variables in this class without defining sub-groups and instead focus on refining the membership within this class. The ROT variables are likely to be a diverse sample of rotational variable types, including α^2 Canum Venaticorum variables (ACV), RS Canum Venaticorum-type (RS) binary systems, BY Draconis-type variables (BY), FK Comae Berenices-type variables (FKCOM), rotating ellipsoidal variables (ELL) and spotted T Tauri stars showing periodic variability (TTS/ROT).

The location of these rotational variables in the Wesenheit W_{JK} period-luminosity space is shown in Figure 9, grouped into the sub-groups BY, ACV, RS and TTS/ROT based on the existing VSX classifications. Different clusters are visible — main sequence/pre-main sequence dwarfs (e.g., BY, TTS/ROT) cluster at W_{JK}~4 mag and rotating giants (e.g., RS) cluster both at W_{JK}~1 mag and W_{JK}~ − 1. Note that there seem to be significant numbers of misclassified BY variables that are giants rather than dwarfs. The distinction between the rotational variables and semi-regular variables (black points) at similar periods is evident.

In order to refine the sample of rotational variables, we set the classification of variables classified as ROT with periods $P > 30$ d that fall into the region occupied by red giants (§3.4.6) to semi-regular variables (SR). Rotational variables are those sources that are periodic, with $0.2 \leq P \leq 150$ d. Outbursting Be stars and other Gamma Cassiopeia variables (GCAS) are commonly classified into the broad ROT class by our V1 RF classifier. Therefore, we looked at the non-periodic sources in this group to look for GCAS variables. We change the classification of a non-periodic ROT variable to GCAS if it falls along the region defined for GCAS variables in §3.4.6 and has $J - K_s < 1.1$ mag, G_{BP} - $G_{RP} < 1.4$ mag, $J - H < 0.5$ mag and $A > 0.25$ mag. We also check for young stellar objects (YSOs) with rotational modulation using the criteria defined in §3.4.6. An uncertainty flag is added to the remainder of the sources that do not meet any of these criteria (i.e, ROT:).

We caution the reader that the ROT: class is a 'catch-all' class for sources with amplitudes of variability below the ASAS-SN threshold, including eclipsing binaries in crowded fields with artificially shallow eclipses due to blending. The smallest detectable variability amplitude in ASAS-SN varies as a function of mean magnitude, from A_{min}~0.02 mag at V~12 mag, to A_{min}~0.1 mag at V~16 mag (see Figure 6 in Paper I). While we removed sources with variability amplitudes $A \lesssim 0.05$ mag regardless of magnitude, sources with variability below the detection threshold at a given mean magnitude (usually rotational variables and eclipsing binaries) tend to be classified into the ROT: class in our pipeline, largely based on their Wesenheit magnitudes and colors. Sources that have poor ASAS-SN light curves with outliers are also likely to be included in this class. Care must be taken when interpreting the variability results for these sources.

3.4.5 Eclipsing Binaries

Eclipsing binaries allow observers to probe fundamental physical characteristics, including the masses and radii of stars and they span a diverse range of stellar systems (see Torres et al. 2010, and references therein). Most main-sequence stars have a companion, hence eclipsing binaries are abundant compared to most kinds of variable stars. Recently, the OGLE survey cataloged a combined ~500,000 eclipsing binaries in the Magellanic Clouds and the Galactic bulge (Pawlak et al. 2016; Soszyński et al. 2016). Eclipsing binaries are also used to estimate extragalactic distances (Pietrzyński et al. 2013; Bonanos et al. 2003) .

We aim to categorize the light curves of eclipsing binaries into the VSX photometric classes: EW, EB and EA.

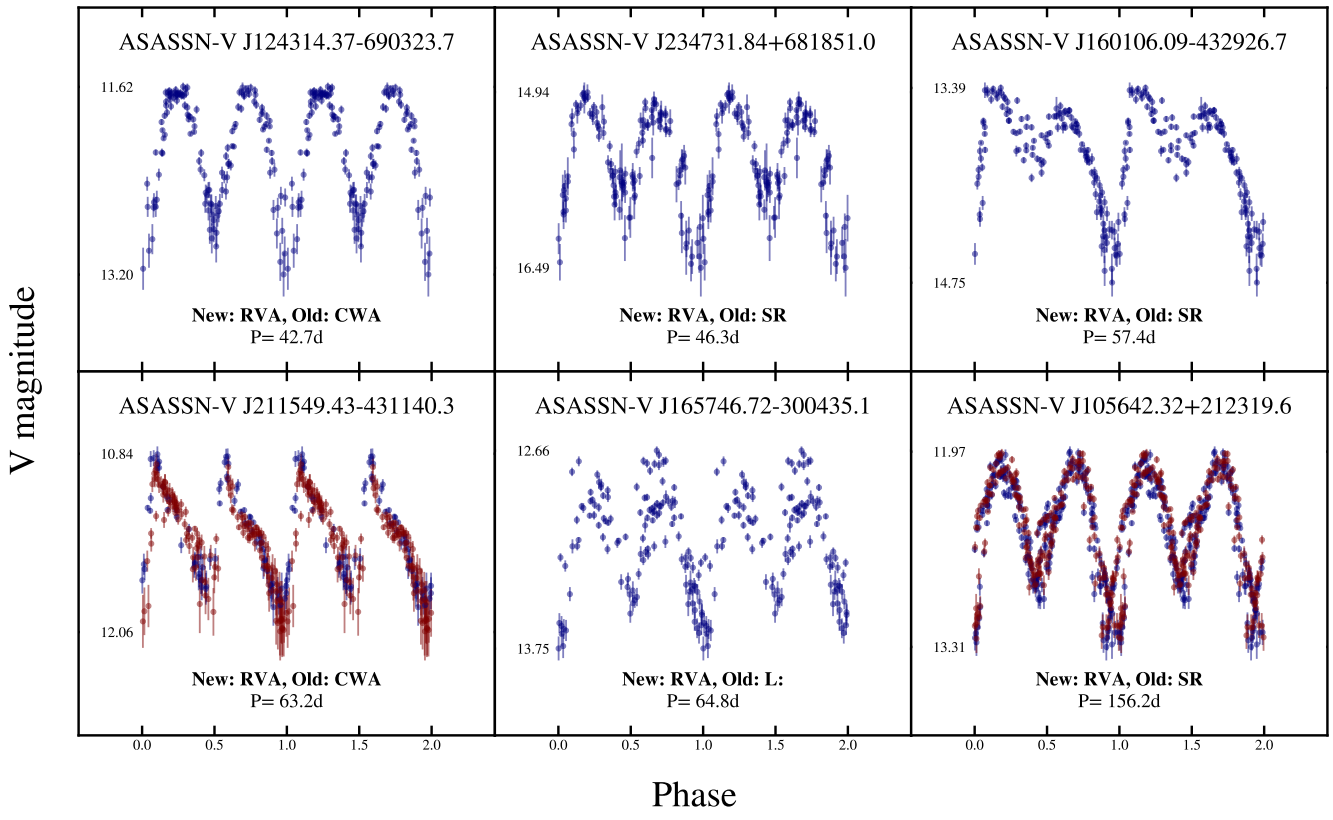

Figure 8. Phased light curves of new RV Tauri variables. The light curves are scaled by their minimum and maximum V-band magnitudes. Different colored points correspond to data from the different ASAS-SN cameras.

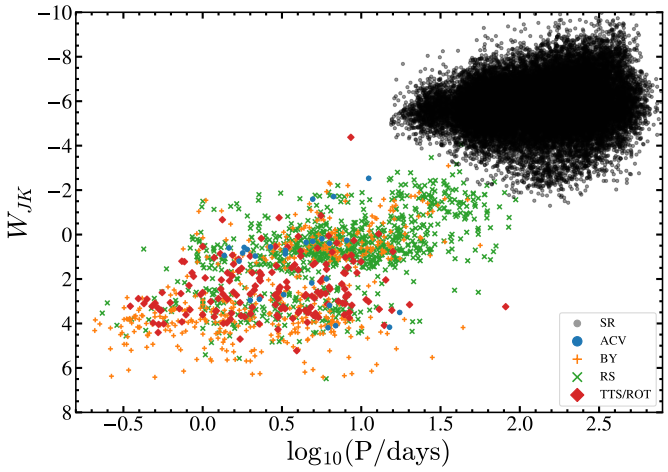

Figure 9. Wesenheit W_{JK} vs $\log$P for the rotational variables grouped by their existing VSX type. The SR variables are also shown in black.

EW (W UMa) binaries have light curves with minima of similar depths and EB (β-Lyrae) binaries have minima of significantly different depths. Both EW (contact) and EB (contact/semi-detached) binaries transition smoothly from the eclipse to the out-of-eclipse state. EA (Algol) binaries are detached systems where the exact onset and end of the eclipses are easily defined. EA systems may or may not have a secondary minimum.

Eclipsing binaries have also been divided into the contact, semi-detached and detached binary configurations with the use of a Fourier model (Pojmanski 2002; Paczyński et al. 2006). In Paper I, we noted the difficulty of separating the photometric classes through visual review alone. In order to improve classification and reduce human intervention, we implement an additional RF classifier dedicated to the classification of eclipsing binaries into the three photometric classes.

We updated our automated period doubling routine described in Paper I for this work. Each light curve is divided into 25 bins, phase folded by the best period with the primary minimum at phase 0, and normalized by the global minimum and maximum. We search for a secondary minimum in the phase interval $[0.2, 0.8]$, updated from the interval of $[0.3, 0.7]$ used in Paper I to improve our sensitivity to eccentric binaries. We identify the local minimum and check to see if the derivative $d(\text{mag})/d(\text{phase})$ within ± 0.15 in phase changes sign and is at least 0.25σ from the mean value of the light curve. If such a minimum is not found, we automatically double the period for that source. We visually reviewed a sample of eclipsing binaries that had their period doubled through this approach and find that it works very well except when the light curves are exceptionally noisy.

Figure 10 illustrates these results. The analytic expression for the PLR derived by Chen et al. (2018) is shown in

red for reference. The left panel illustrates the existing VSX periods for the EW type binaries. A second locus of binaries is seen displaced in period by a factor of two. The results of our automated period doubling routine are shown in the right panel. The secondary locus of EW binaries with half their true period has vanished.

In addition, the periods of over ~15,000 eclipsing binaries were visually reviewed by the authors in order to better familiarize themselves with the shapes of the light curves. We selected a sub-sample of ~5,000 sources, removed noisy light curves, and manually classified them into the three photometric classes (EW, EB and EA) to obtain a training set of ~4,300 eclipsing binaries.

We trained a dedicated RF classifier for the eclipsing binaries using this training set. We use the following features in the ECL classifier, where the importance of each feature is listed in parentheses (see Table 2 for descriptions): Skew (8%), Kurt (10%), $A_{\rm HL}$ (3%), $\log P$ (15%),R_{41} (5%), R_{21} (10%), R_{32} (5%), R_{42} (31%) and the ratio of minima $R_{\rm minima}$ (14%). The features derived from the Fourier model play a heavy role in the classifier, with a combined importance of 51%. The precision, recall and F_1 scores for each binary type is summarized in Table 5. The EA and EW classes are very well classified with $F_1 \gtrsim 95\%$. The EB class has a lower score of $F_1 = 91\%$ due to confusion with EW binaries, as illustrated in the confusion matrix shown in Figure 11. The eclipsing binary classifier has an overall F_1 score of 95.1%.

Figure 12 shows the distribution of the training set binaries in the three most important classification features — R_{42}, $\log P$ and $R_{\rm minima}$. The left panel shows the distribution in R_{42} and $\log P$, and it is immediately clear why this is the most important feature in this classifier. EW variables are strongly clustered at $(\log P, R_{42})\sim(-0.5, 0.2)$, with the EB variables offset towards longer periods. EA variables are easily distinguished from both EW and EB types, as they predominantly occupy the region with $R_{42} \gtrsim 0.5$. The right panel illustrates the distribution of the peak ratio $R_{\rm minima}$ against $\log P$. Once again, EW variables are strongly clustered towards $(\log P, R_{\rm minima})\sim(-0.5, 0.95)$, as is expected given their eclipse profiles. EB variables are offset towards longer periods and typically have $R_{\rm minima} \lesssim 0.8$. EA variables are "randomly distributed" in this space since it is not unusual for detached eclipsing binaries to have minima of very similar depths.

In Figure 13, we show the distribution of the eclipsing binaries in our training sample in the Fourier components a_2 and a_4. These are commonly used to classify eclipsing binaries into the three physical configurations. Rucinski (1993) defined a relationship to separate contact binaries from semi-detached/detached binaries as

$$a_4 = a_2(0.125 - a_2), \tag{9}$$

which is shown in black. We have also shaded the locii of the contact and semi-detached/detached configurations in orange and blue respectively. This relationship is able to seperate contact binaries (EW) efficiently. EB types live in both the contact and semi-detached/detached regions, suggesting that the EB class is an intermediary class to both the EW and EA classes with respect to the physical configuration. EA binaries all lie in the semi-detached/detached space as is expected.

Both classification schemes (i.e., the photometric classes and the physical configurations) have been used by previous variability studies, and the mappings between the classifications are not homogeneous. With the use of this eclipsing binary classifier, we are able to homogeneously refine the classifications given to eclipsing binaries in the VSX catalog. Example light curves are shown in Figure 14. It is clear that our pipeline is able to break common degeneracies in eclipsing binary classifications. For example, the ASAS survey had a large number of classifications with degenerate classifications. We have provided updated classifications in many such cases.

Table 5. Precision,Recall and F_1 score Values by class for the eclipsing binary classifier.

Class	Precision	Recall	F_1 score
EA	93%	98%	95%
EB	95%	87%	91%
EW	100%	99%	99%

We show the Wesenheit W_{JK} PLR for each class of eclipsing binary using our complete sample of ~53,000 binaries in Figure 15. Lines denoting the 1st and 99th percentiles in period are drawn for each class. EW binaries span periods of $0.23 \leq P_{1-99} \leq 0.98$ d. The distribution of EB binaries start at slightly longer periods and extend to to periods longer than a day with $0.28 \leq P_{1-99} \leq 9.1$ d. We see a similar distribution in periods for the EA types, with these spanning the range $0.32 \leq P_{1-99} \leq 13.30$ d. The PLRs for EW and EB types are distinctly sharper and better defined than the PLR of EA binaries. To further refine the eclipsing binaries, we impose an upper limit of $P < 100$ d to the sources that have classification probabilities Prob < 0.9. Variables that have $P > 100$ d and Prob < 0.9 are reclassified as semi-regular variables if they fall into the red giant region (§3.4.6), otherwise they are assigned the generic variability class ('VAR').

3.4.6 Semi-regular and Irregular Variables

Most semi-regular variables are pulsating red giants that show varying levels of periodicity in their light curves. Multi-periodic behavior is commonly seen in the light curves of semi-regular variables and can be used to study the dynamics of stellar interiors (Kiss et al. 1999). OGLE discovered a new class of low amplitude semi-regular variable in the Magellanic clouds, the OGLE small amplitude variable red giants (OSARGs; Soszynski et al. 2004), that follow a set of period-luminosity relations (Soszynski et al. 2007). GCAS variables are eruptive irregular variables with early spectral types (O9-A0 III-Ve) and have mass outflows from their equatorial zones (Watson et al. 2006; Bernhard et al. 2018). SRD variables are yellow semi-regular variables that are giants and supergiants with spectral types of F/G/K.

In order to refine the classifications of semi-regular/irregular variables, we look at their positions in the Wesenheit W_{RP} vs. $G_{BP} - G_{RP}$ color-magnitude diagram (Figure 16). We empirically define regions for red giants, YSO/ROT variables, and GCAS variables and shade these in red, green, and blue respectively. Similar regions were found by Mowlavi et al. (2018) for YSOs and red giants.

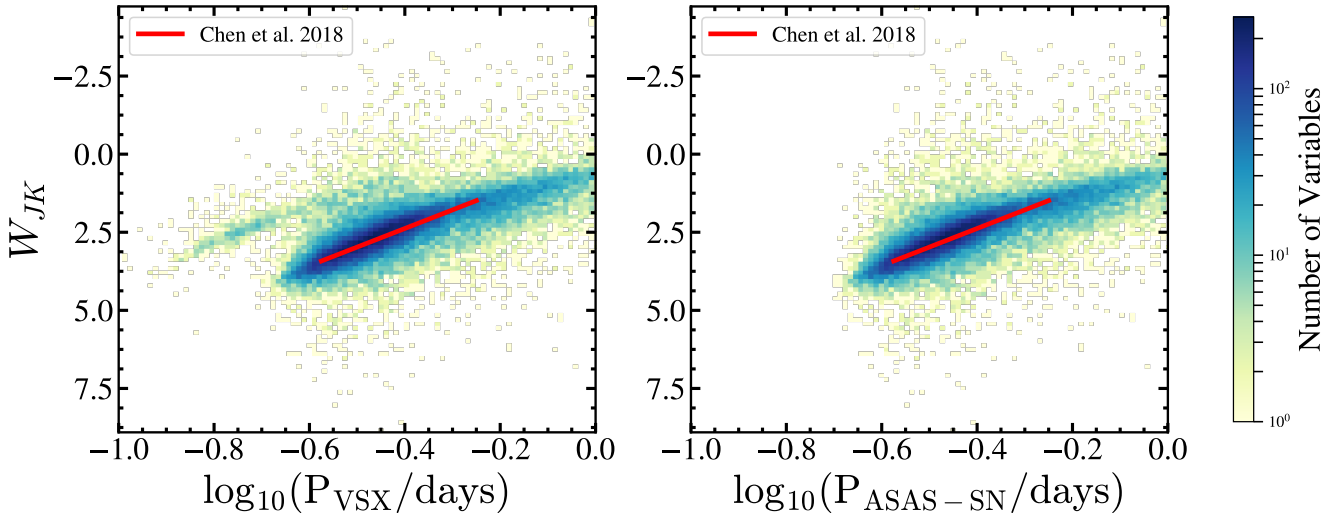

Figure 10. The Wesenheit W_{JK} period-luminosity relationship (PLR) for EW binaries. The PLR for the eclipsing binaries is shown as a system density. The analytic expression for the PLR derived by Chen et al. (2018) is shown in red. *Left*: The existing VSX periods for the EW binaries, *Right*: The same sample of EW binaries using the updated periods.

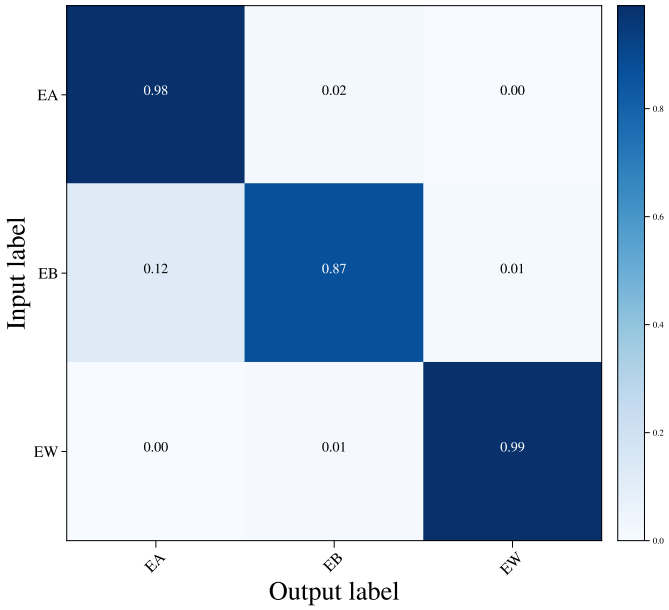

Figure 11. The normalized confusion matrix derived from the trained eclipsing binary random forest classifier. The y-axis corresponds to the 'input' classification given to a variable, while the x-axis represents the 'output' prediction obtained from the trained random forest model.

Variables that are classified as SR/IRR by the RF classifier are first sorted into one of these three sub-groups.

For the SR/IRR sources that lack Gaia data but have complete 2MASS photometry, we use the following criteria for classification. Variables are assigned the red giant class if they have $J-K_s > 1.1$ mag and $J < 10$ mag. Variables are given the GCAS classification if $J-K_s < 1.1$ mag and $J-H < 0.2$ mag. Variables are assigned the YSO VSX class if they have $J-K_s > 1.1$ mag and $J > 10$ mag OR $J-K_s < 1.1$ mag and $J-H > 0.2$ mag. If these sources have WISE photometry, we implement the additional criteria of $W1-W2 > 0.15$. Sources with $W1-W2 < 0.15$ are classified as VAR variables. Any other sources that do not specifically fall into these classes are also assigned the VAR classification.

Variables that are classified as red giants with periods $P > 5$ d and with at least two cycles in the ASAS-SN light curve are classified as semi-regular (SR) variables. Those that do not meet this criteria or have no period are classified as a red irregular variables (L). Variables that fall into the red giant region meeting the periodicity criteria defined above are classified as SRD variables if $W_{RP} < -5$ mag, $J-K_s < 1.1$ mag, and $G_{BP}-G_{RP} < 2$ mag.

Variables need to meet the following criteria in order to be classified as GCAS variables: $J-K_s < 1.1$ mag, $G_{BP}-G_{RP} < 1.4$ mag, $J-H < 0.5$ mag and $A > 0.25$ mag. If they have $J-K_s > 1.1$ mag and $G_{BP}-G_{RP} > 1.4$ mag, they are classified using the criteria defined for red giants. The remainder of the sources in this region are assigned an uncertainty flag (i.e., GCAS:).

We use AllWISE photometry to separate main sequence rotational variables from young stellar objects on the pre-main sequence. Variables that are grouped into the YSO/ROT sub-class are empirically sorted into the YSO class based on their position in the W_{RP} vs. $W1-W2$ color-magnitude diagram (Figure 17). In the left panel, rotational variables form two clusters comprised of dwarfs (W_{RP}~4 mag) and giants (W_{RP}~0 mag). In the right panel, YSOs form two clusters largely comprising of Class II YSOs ($W3-W4$~0.8 mag) and Class I/III YSOs ($W3-W4$~2.2 mag). We essentially look for evidence of an infrared excess for the YSO variables. This is similar to our approach in Paper I but is significantly more accurate due to the use of WISE and Gaia DR2 data. When comparing the AllWISE color-color diagram shown in the right panel in Figure 17 (this work) to Figure 7 of from Koenig & Leisawitz (2014) , we see that this method is very useful in identifying YSOs.

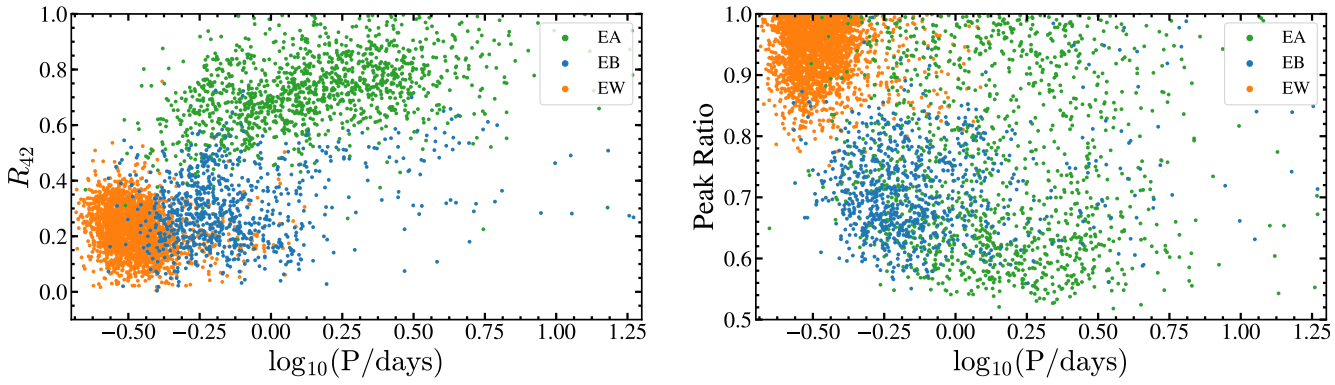

Figure 12. Distribution of the eclipsing binary training set in R_{42} vs $\log P$ (*left*), and the peak ratio $R_{\rm minima}$ vs $\log P$ (*right*). The points are colored by the eclipsing binary class assigned to them.

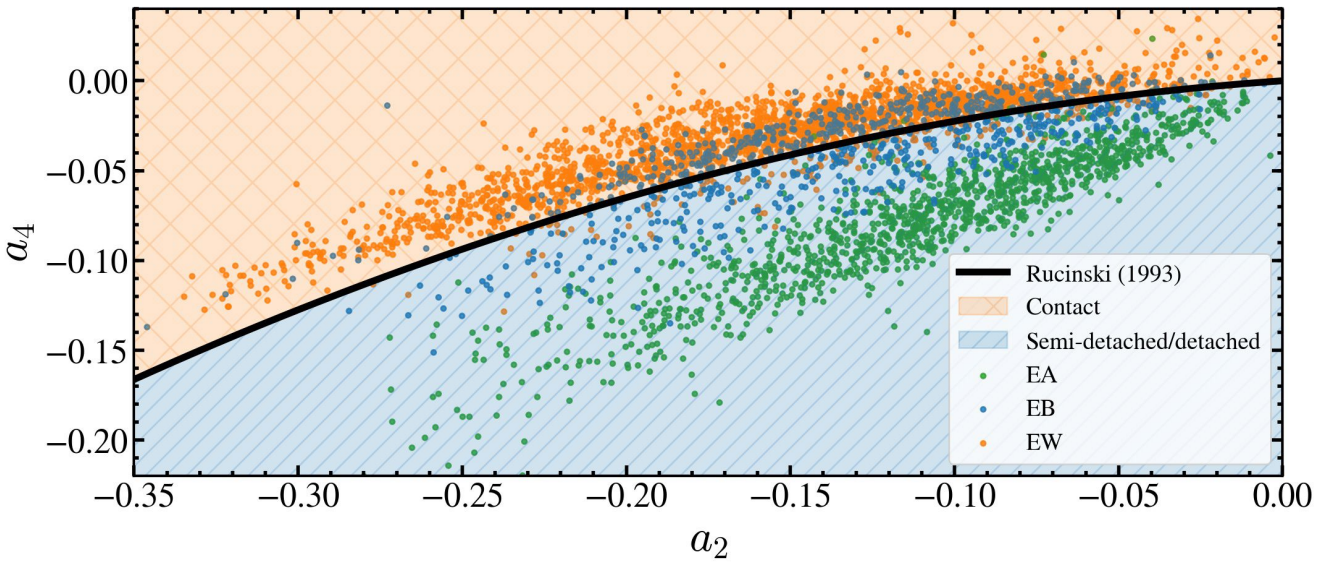

Figure 13. Distribution of the training sample of eclipsing binaries in the Fourier components a_2 and a_4. The relationship used by Rucinski (1993) to seperate contact binaries from semi-detached/detached configurations is shown in black. The regions occupied by contact and semi-detached/detached binaries based on this relationship are shaded in orange and blue respectively.

We successfully classify YSOs of different types, including sources that are consistent with the YSO classes I/II/II and YSOs with transition disks (Koenig & Leisawitz 2014). If the YSO sources are periodic, we check to see if the period satisfies $1 \leq \mathrm{P} \leq 100$ d and that we have at least two cycles in the ASAS-SN light curve before assigning a period. YSOs that do not meet this periodicity criteria are not assigned a period. Variables in the YSO/ROT region that are not classified as YSOs are classified as rotational variables (ROT). The criteria used to refine these rotational variables are the same as in Section §3.4.4.

Variables with missing photometric information and variables that do not meet any of the classification criteria described above are assigned the VAR classification. This makes the VAR variable class a catch all for unusual sources that do not fit into standard variable star classification criteria, sources with bad nearest neighbor cross-matches to other catalogs and sources with one or more pieces of missing information.

In Figure 18, we look at the distribution of rotational and semi-regular/irregular variables in the Gaia DR2-2MASS $G_{BP} - G_{RP}$ vs $J - K_s$ color-color diagram. For reference, we also show the sources from the Catalog of Galactic Carbon Stars (Alksnis et al. 2001) in black. The carbon stars form a sharp locus in this color-color space and have larger values of $J - K_s$ for a given G_{BP}-G_{RP} once $G_{BP} - G_{RP} \gtrsim 2$ mag than any other semi-regular/irregular variable source. Some fraction of the semi-regular and irregular sources fall along this Carbon star locus, suggesting that these are carbon enriched sources. The positions of the semi-regular and irregular sources in this space are clearly distinct from that of the carbon stars, which implies a difference in stellar chemistry for the majority of these sources when compared to the carbon rich sources. At bluer colors

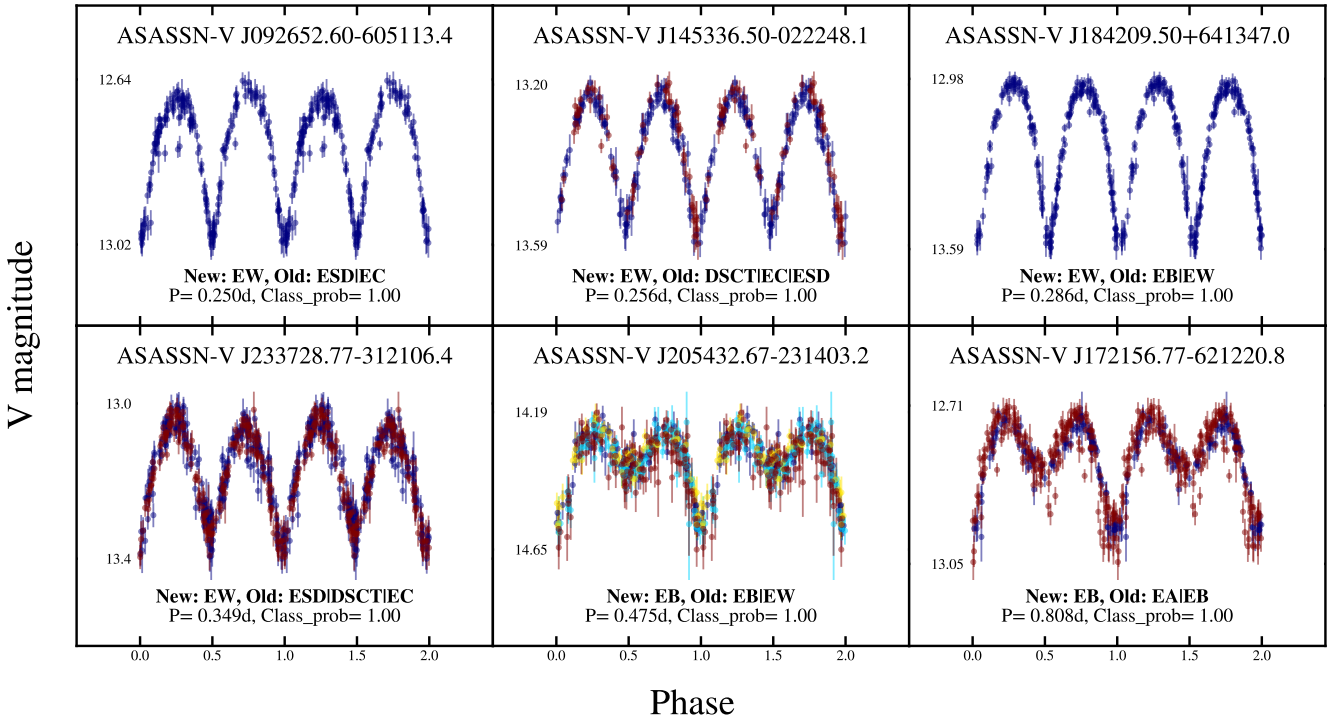

Figure 14. Phased light curves of eclipsing binaries with refined classifications. The format is the same as Figure 8.

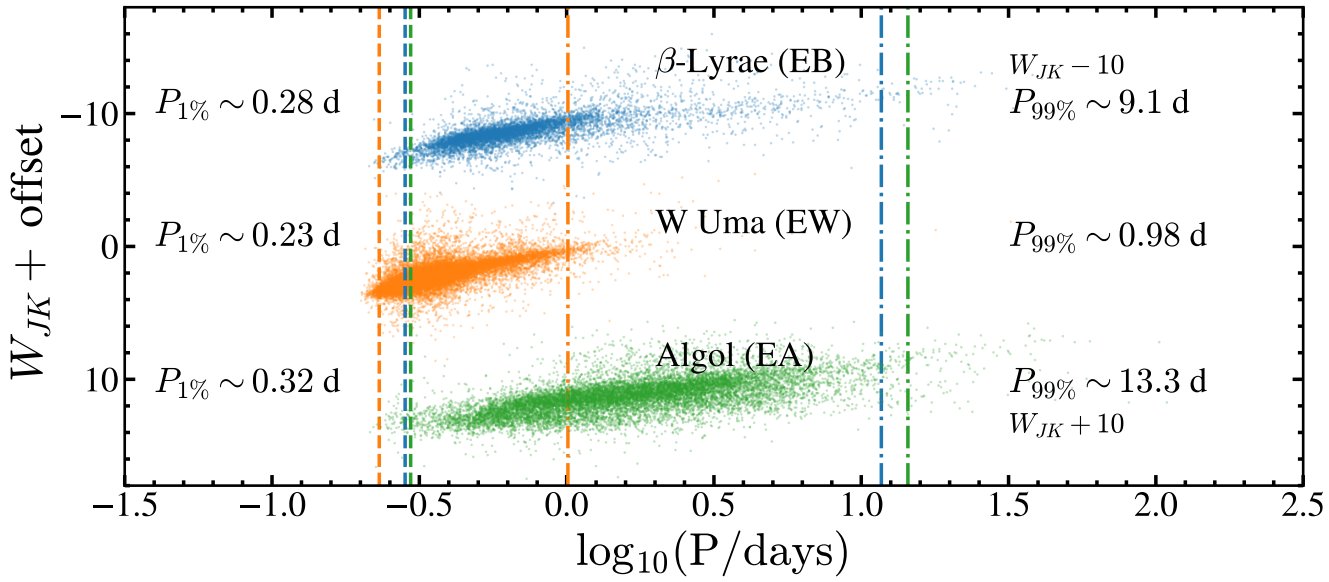

Figure 15. The Wesenheit W_{JK} PLR for the different classes of eclipsing binaries. Lines denoting the 1st and 99th percentiles in period are drawn for each class.

($G_{BP} - G_{RP} \lesssim 2$ mag), it becomes harder to distinguish the different variable classes. The position of the rotational variables is particular interesting — it remains distinct from the locus of semi-regular/irregular sources and plateaus at a color of $J - K_s$~0.8. Most GCAS variables also lie away from the ROT locus, with a large number of these sources having $G_{BP} - G_{RP} < 0.5$ mag and $J - K_s < 0.5$ mag.

3.4.7 Mira Variables

Mira variables (M) are asymptotic giant branch (AGB) stars that show high amplitude (typically $A \gtrsim 2.5$ mag in the V-band and decreasing with wavelength) variability with typical periods $P > 100$ d. Mira variables have also been found to follow a period-luminosity relationship (Whitelock et al.

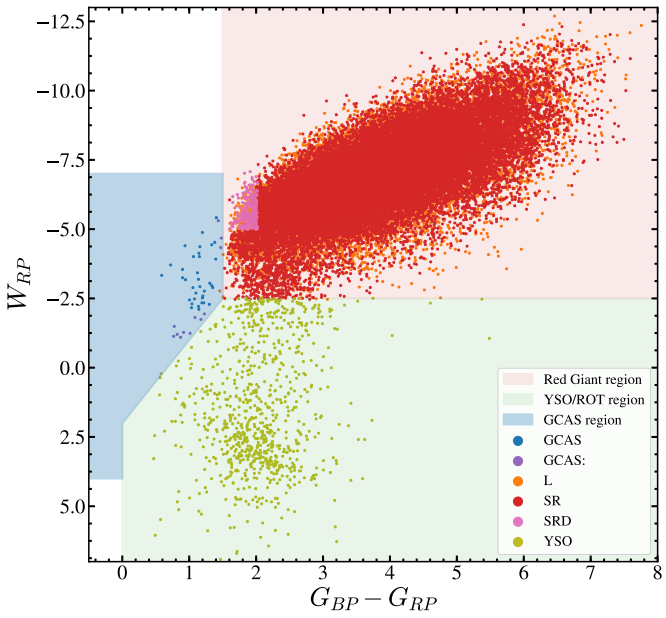

Figure 16. The Wesenheit W_{RP} vs. G_{BP}−G_{RP} color-magnitude diagram used in the classification of semi-regular variables. The empirically defined regions for red giants, YSO/ROT variables, SRD variables and GCAS variables are shaded in red, green, pink and blue respectively. The points are colored according to the final classifications assigned to each variable.

2008) and are useful distance indicators owing to their large intrinsic luminosities. However, Mira variables can undergo changes in their period over time (Percy & Colivas 1999), so one must be cautious about using these variables when deriving precise distances. Recently, oxygen-rich Mira variables have also been used to study age gradients in Galactic populations, noted in Grady et al. (2018).

As in Paper I, some of the Mira variables can dip below the detection limits for ASAS-SN ($V \gtrsim 17$ mag), resulting in underestimated variability amplitudes. This can also result in inadequately sampled light curves that result in incorrect periods. Mira variables in crowded fields, particular towards the bulge and Galactic disk, can be misclassified as semi-regular variables owing to the reduction in variability amplitudes due to blending (Mowlavi et al. 2018).

To refine the classifications of Mira variables, we use the red giant region defined in Section §3.4.6. A Mira variable (M) is one which falls into the red giant region and has an amplitude $A > 2$ mag in the V-band. We choose to relax this amplitude criteria from the standard of $A > 2.5$ mag in the V-band to better deal with blended and underestimated amplitudes. Variables that are classified as MIRA through the RF classifier and fall into the red giant region but have amplitudes $A < 2$ mag are classified as semi-regular (SR) variables. Other sources that are given the MIRA class but do not fall into the red giant region are assigned the generic VAR class. Mira variables without a period are given an uncertainty flag.

3.5 Properties of the Final Training Sample

All of the refinements from §3.4 are applied to the enlarged training set from §3.3 before building V2 of the RF variability classifier. Sources that were assigned uncertain or generic variability classifications and those with V1 probabilities Prob < 0.8 were removed from the training sample, resulting in a final training set of 166,000 variables.

In Figure 19, we compare the periods derived through the ASAS-SN variability analysis pipeline ($P_{\rm ASAS-SN}$) to the periods in the VSX catalog ($P_{\rm VSX}$) for the training set. A large majority (66%) of the sources have ASAS-SN periods within ±5% of the VSX periods. Most of the differences are for longer ($P > 100$ d) period variables that are typically semi-regular and Mira variables. The light curves of semi-regular variables are likely to be multi-periodic and have loosely defined periods. However, 2% are assigned ASAS-SN periods that are twice the VSX period, largely due to our better treatment of eclipsing binaries. We also see some evidence that ASAS-SN provided better periods for sources that have aliases of a sidereal day as the VSX period. Examples of sources with different ASAS-SN and VSX periods are illustrated in Figure 20.

Due to the refinements in §3.4, ∼5,000 sources out of the ∼166,000 sources were assigned to a different broad class. Of these, ∼1,800 variables were reclassified as eclipsing binaries, with the vast majority being reclassified as EW binaries. Reclassifications to and from the broad classes RRAB and RRC/RRD are also common, with the vast majority being RRAB variables reclassified as RRD variables. Examples of these reclassified sources are shown in Figure 21.

The Gaia DR2 M_G vs. $G_{BP} - G_{RP}$ color-magnitude diagram for all the sources in the training sample is shown in Figure 22. We have sorted the variables into groups to highlight the different classes of variable sources after refinement. To highlight the variable types other than the red giants and Mira variables, we show the same color-magnitude diagram in Figure 23. Using the same color scheme, the combined Wesenheit W_{JK} PLR diagram for the periodic variables in our training sample is shown in Figure 24.

In Figure 25, we show the distribution of RR Lyrae, δ Scuti and Cepheid variables in the Gaia DR2-2MASS $G_{BP} - G_{RP}$ vs $J - K_s$ color-color diagram. The locus of Cepheids (both classical and Type II) is sharp and near $G_{BP} - G_{RP}$∼0.5. There is some overlap with the RR Lyrae locii. RRC, DSCT and HADS variables are typically bluer in their $G_{BP} - G_{RP}$ colors than RRAB variables. The locus of HADS variables is slightly different from that of the DSCT variables.

Figure 26 shows the distribution of the training sample in the space of $T(\phi|P)$ and classification probability Prob for the ∼127,000 periodic variables in the training set. Values for $T(\phi|P)$ or $T(t)$ and Prob are provided on the ASAS-SN Variable Stars Database for users to fine-tune their queries and retrieve high confidence classifications. $T(\phi|P)$ and $T(t)$ are very sensitive to outliers and is a probe of light curve quality, especially for strictly periodic variable types like RR Lyrae and Cepheids. $T(\phi|P)$ will be larger for sources with noisy light curves, those with outliers and less regular periodic variables. We illustrate the sensitivity of $T(\phi|P)$ to outliers and noise in Figure 27. While we choose to use all ∼127,000 variables in our classifier, a very clean sub-sample of ∼90,000

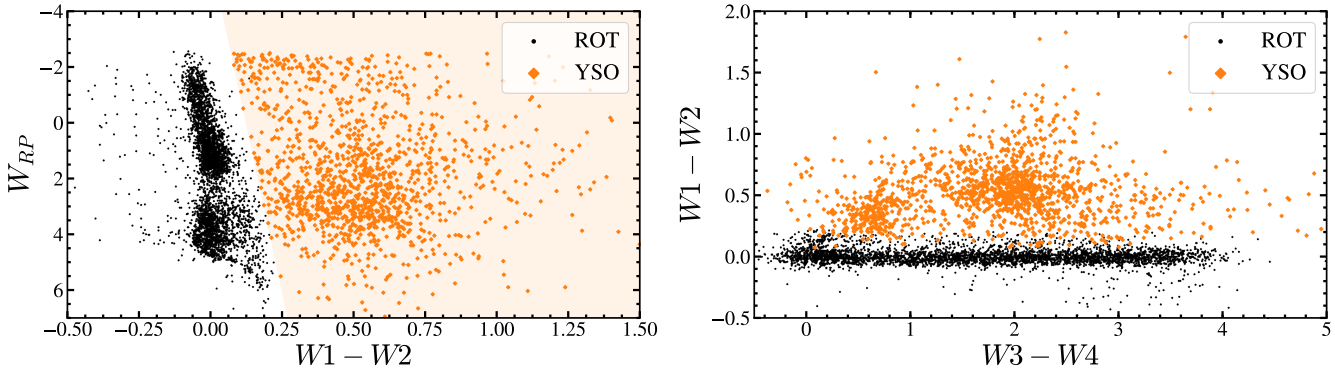

Figure 17. *Left*: The Wesenheit W_{RP} vs. $W1-W2$ color-magnitude diagram used in the classification of YSO variables. The empirically defined locus for the YSO variables is shaded in orange, *Right*: The WISE $W3-W4$ vs $W1-W2$ color-color diagram highlighting the YSO variables. The ROT class shown here is derived from the rotational variables classified separately from the SR/IRR sources in order to highlight the distinction between YSO and ROT variables. The YSO variables shown here were drawn from the SR/IRR class.

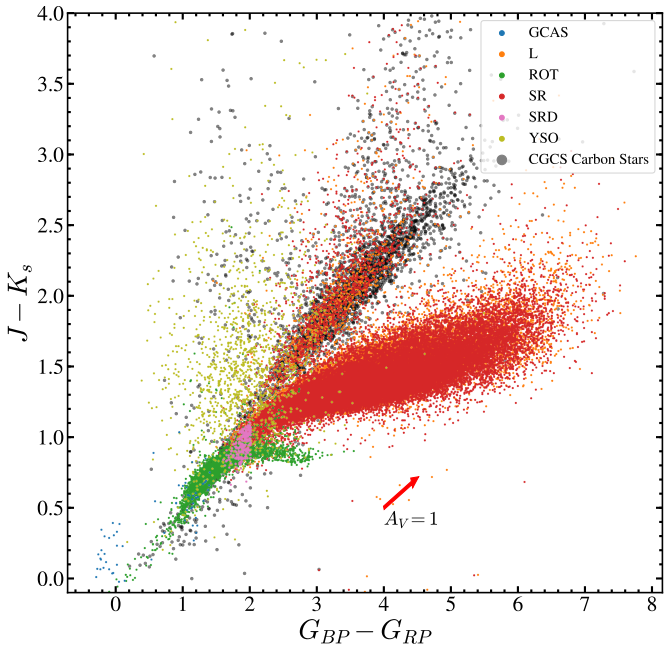

Figure 18. The Gaia DR2-2MASS $G_{BP}-G_{RP}$ vs $J-K_s$ color-color diagram for the rotational and semi-regular/irregular variables. Carbon stars from Alksnis et al. (2001) are plotted in black. The reddening vector corresponding to an extinction of $A_V = 1$ mag is shown in red.

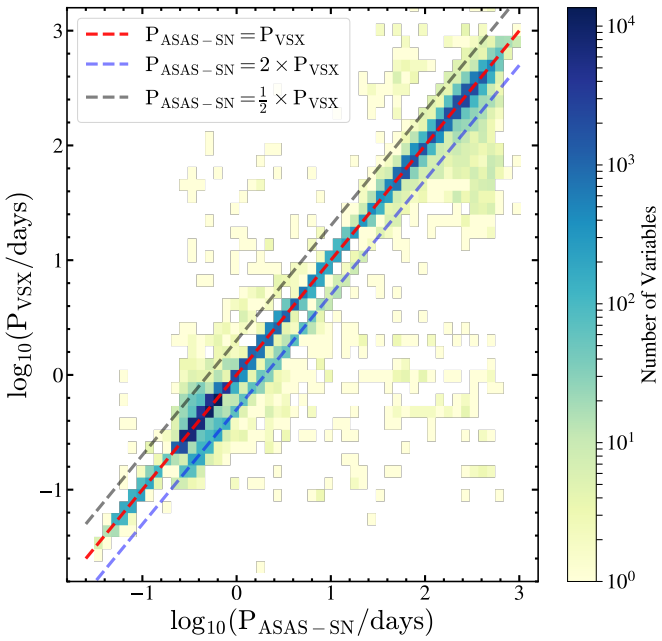

Figure 19. A comparison of the ASAS-SN periods $P_{\rm ASAS-SN}$ to the existing, VSX periods $P_{\rm VSX}$ for the variables in the training set. Dotted line are shown to represent ASAS-SN periods that are the same (red), twice (blue) and half (black) the VSX period.

periodic sources having high classification probabilities and well phased light curves with minimal noise/outliers can be obtained by selecting the variables with Prob > 0.9 and $T(\phi|P) < 0.5$.

Table 6 shows how $T(\phi|P)$ and $T(t)$ depend on the type of variability. For periodic variables, $T(\phi|P)$ is calculated on the light curve sorted by phase. While for non-periodic sources, $T(t)$ is calculated on the light curve sorted by time. It is clear that the variable types expected to have larger dispersions in the phased light curve (ex: ROT, RRD, SR) have larger median values for $T(\phi|P)$ when compared to variable types that have more regular light curves (ex: DCEP, DCEPS, RRAB).

The distribution of the variables in our training sample with the ASAS-SN V-band, Gaia DR2 G-band, G_{BP}-band and G_{RP}-band magnitudes are shown in Figure 28. The distribution of sources in the G_{BP}-band closely follows the distribution in the ASAS-SN V-band. A small fraction of these sources are consistent with issues from cross-matching. Nearest neighbor matching can result in errors, however through our refinement process, most of the sources with

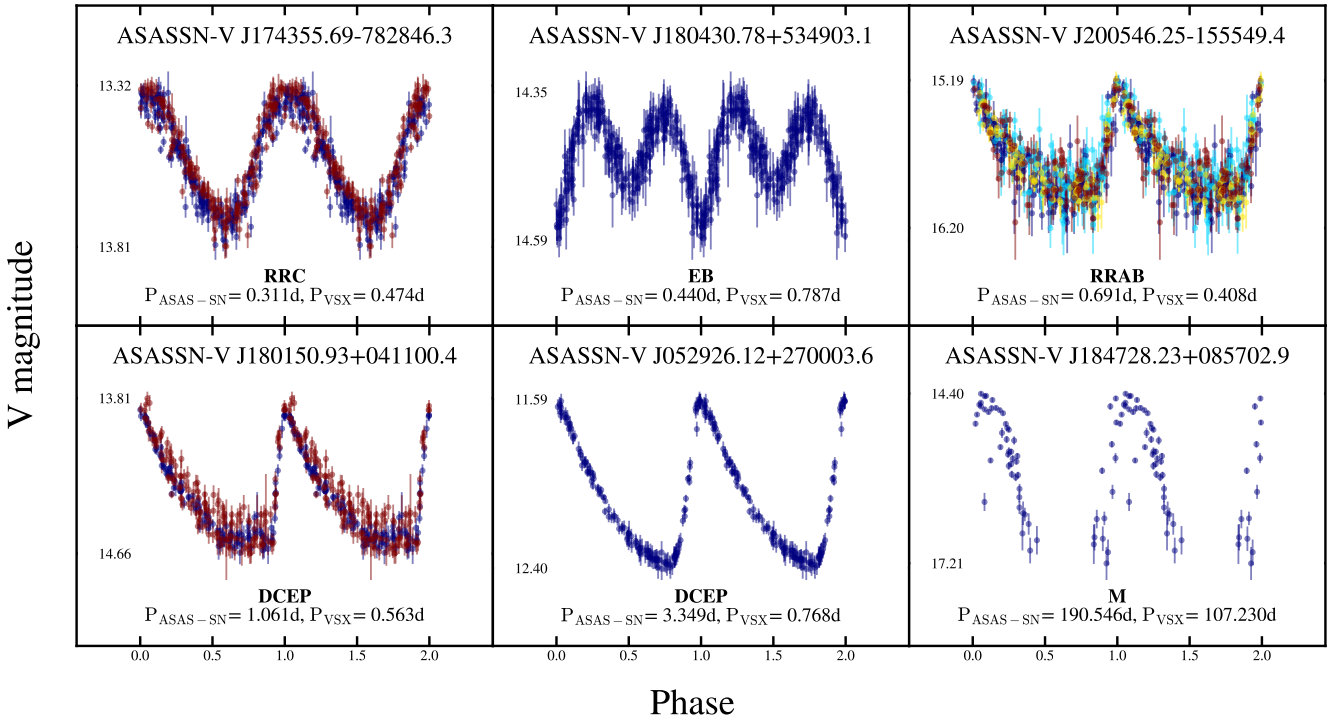

Figure 20. Examples of variables with different ASAS-SN and VSX periods. The format is the same as Figure 8.

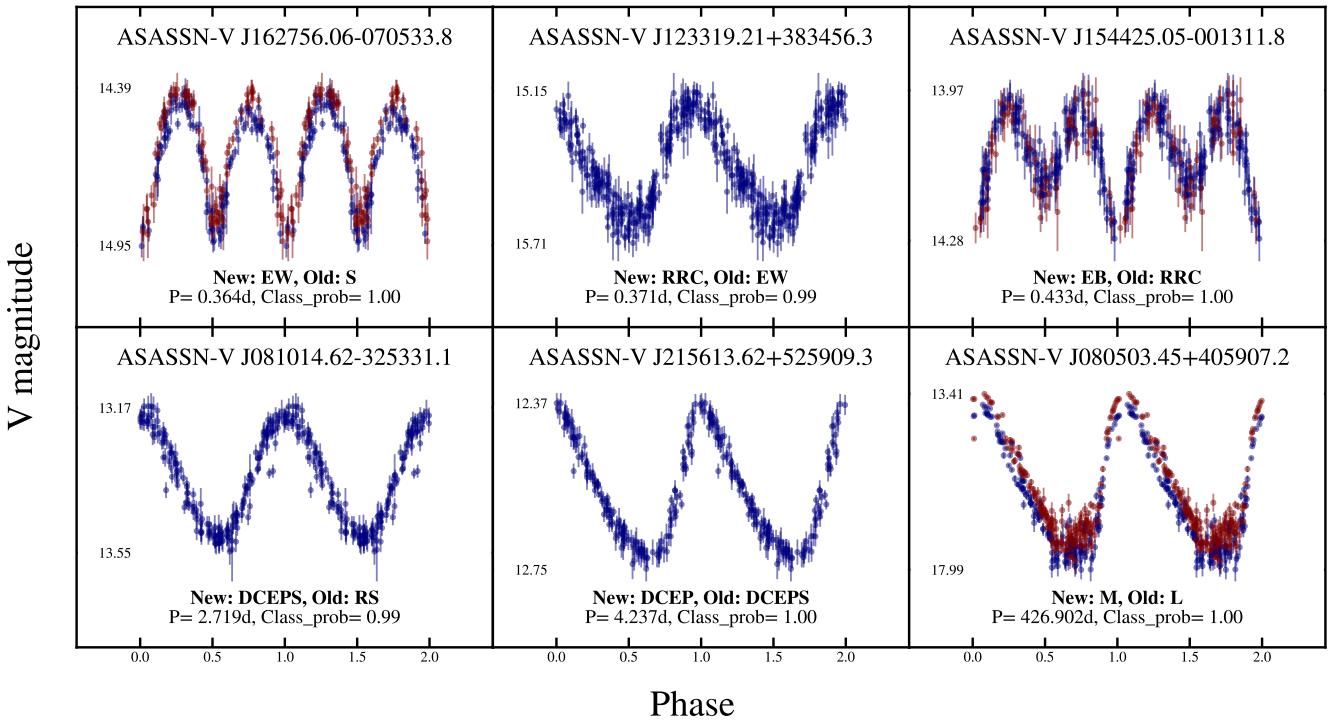

Figure 21. Examples of variables with new classifications. The format is the same as Figure 8.

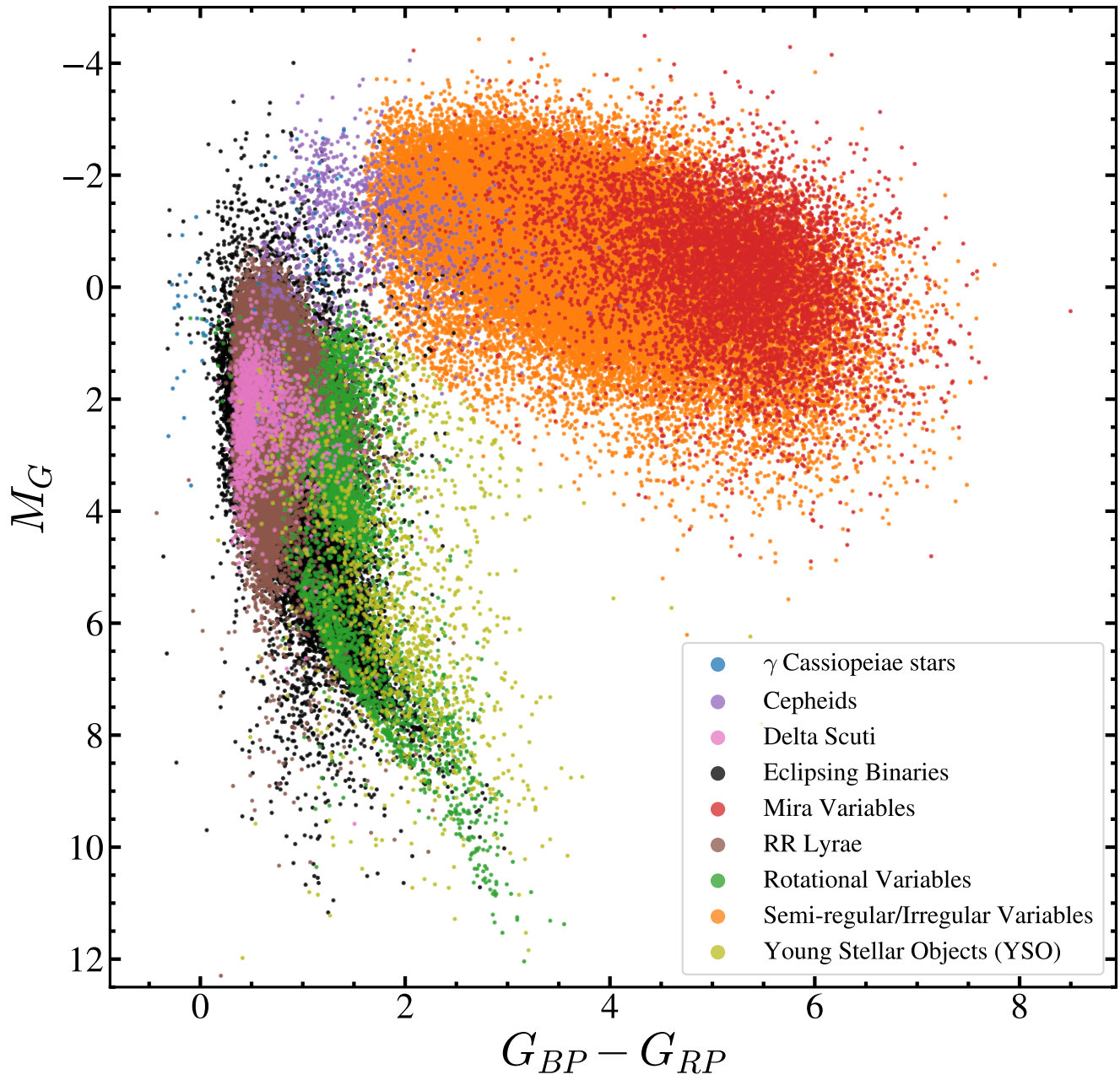

Figure 22. The Gaia DR2 M_G vs. $G_{BP} - G_{RP}$ color-magnitude diagram for the variables in the training sample. The points are sorted into the groups described in the legend, and are colored accordingly.

cross-matching errors are given a VAR or uncertain classification.

3.6 V2 of the ASAS-SN Variability Classifier

Next, we create an updated version of our RF classifier. The random forest model parameters used to define the V2 RF classifier were the same as that used for V1. The variables in our training sample were assigned the same broad classes based on their refined classifications: CEPH, RRAB, RRC/RRD, SR/IRR, M, DSCT and ECL. To calculate Fourier features, we use a Fourier model of order 6. Distance estimates from Bailer-Jones et al. (2018) were used to calculate absolute Wesenheit magnitudes. The complete list of classification features and their importances for the V2 RF classifier is summarized in Table 2. Overall, we only use 17 features here compared to the 28 used in the first version. Features that can be extracted without the use of external catalogs account for ~70% of the importance value.

As in Paper I, the training set was split for training (80%) and testing (20%) in order to evaluate its performance. The performance of the V2 classifier is summarized in Table 3. There is an improvement over V1 in F_1 scores across the board. All of the classes have F_1 scores greater

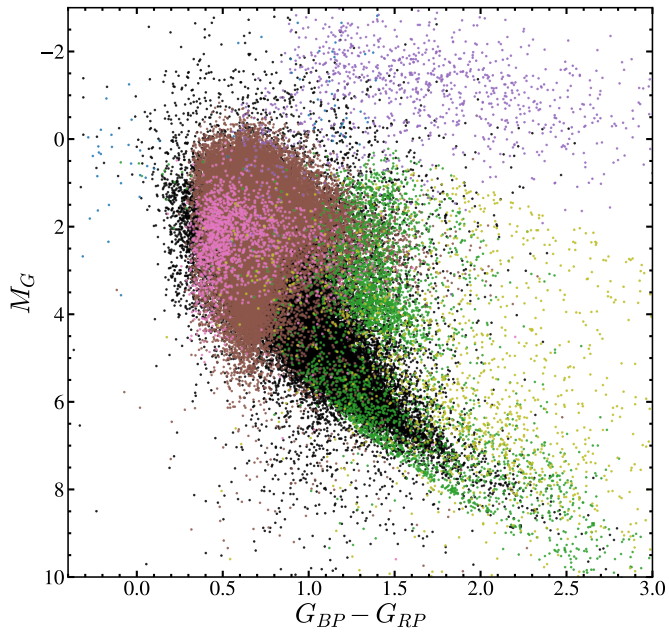

Figure 23. The Gaia DR2 M_G vs. $G_{BP} - G_{RP}$ color-magnitude diagram for the variables in the training sample, excluding red giants and Mira variables. The points are colored as in Figure 22.

Table 6. Behavior of $T(\phi|P)$ and $T(t)$ with variability type. For periodic variables, $T(\phi|P)$ is calculated on the light curve sorted by phase. For non-periodic sources, $T(t)$ is calculated on the light curve sorted by time. The median, and standard deviation for $T(P)$ in each class is shown.

VSX Type	Median $T(\phi\|P)$ or $T(t)$	σ
CWA	0.03	0.15
CWB	0.06	0.15
DCEP	0.03	0.18
DCEPS	0.04	0.22
DSCT	0.76	0.30
EA	0.18	0.28
EB	0.13	0.24
EW	0.22	0.26
HADS	0.16	0.25
M	0.10	0.19
ROT	0.67	0.26
RRAB	0.21	0.22
RRC	0.24	0.23
RRD	0.72	0.30
RVA	0.14	0.32
SR	0.52	0.29
SRD	0.45	0.24
L	0.19	0.18
GCAS	0.18	0.19
YSO	0.51	0.27

than 99%. The overall F_1 score for the V2 classifier is 99.4%, a significant improvement from the the overall F_1 score of 93.3% for V1.

We illustrate the ability of the RF model to classify new objects with the confusion matrix shown in Figure 29. The greatest confusion (1%) is between the RRC/RRD and RRAB classes. After making this test, we rebuilt the classifier using all the variables in the training set for use on the full data set.

4 CLASSIFYING OTHER SOURCES

We integrated the V2 RF classifier described in Section §3.6 with the refinement criteria in Section §3.4 to create a coherent pipeline for variability classification. In this pipeline, periods are assigned to the sources if $T(\phi|P) < 0.55$ for periods P < 40 d, and $T(\phi|P) < 1.0$ for periods P > 40 d. We expect the SR variables that are common at longer periods to have larger values of $T(\phi|P)$. With the V2 RF classifier built, we can now classify the sources excluded when creating the training set. The variables excluded from the training set were those with miscellaneous classifications, those identified by the OGLE survey, the set of variables with low V1 probabilities (see §3.3) and those with mean magnitudes outside of the optimal ASAS-SN range ($11 < V < 17$ mag).

4.1 Variables with Miscellaneous Classifications

We applied our variability classifier to the ~94,000 miscellaneous/generic variables with mean magnitudes in the range $11 < V < 17$ mag. This includes ~12,000 variables identified by the KELT survey that do not currently have specific classifications (Oelkers et al. 2018).

The distribution of the ASAS-SN period $\log \mathrm{P}$ and $T(\phi|P)$ for the miscellaneous variables is shown in Figure 30. Features due to diurnal aliases are clearly visible. In some cases, when a light curve is phased with an alias, some spurious structure is present and minimizes $T(\phi|P)$ for that aliased period. In most such cases, these variables do not have strong periodicity.

In Figure 31, we show these variables in the Gaia DR2 M_G vs. $G_{BP} - G_{RP}$ color-magnitude diagram divided into bins of classification probability for comparison with the distribution of the training sample shown in Figure 22. The VSX MISC category is clearly dominated by luminous, red variables. Examples of these newly classified miscellaneous variables are shown in Figure 32. Most of these sources have good classifications: ~60% (~64%) of the miscellaneous variables have classification probabilities of >0.9 (>0.75). However, ~28,000 of the variables with miscellaneous VSX classifications do not have definite classifications in ASAS-SN, and are classified either to the VAR class or to one of the uncertain classifications (i.e., GCAS:, RRAB:, ROT:, and DSCT:).

4.2 OGLE Variables

We also apply the variability classification pipeline to the ~52,000 OGLE variables in the VSX catalog. For the OGLE sources with an 'LMC' ('SMC') identifier, we use a distance of $d = 49.97$ (62.1) kpc (Pietrzyński et al. 2013; Graczyk et al. 2014). We use the distance estimates from Bailer-Jones et al. (2018) for the remainder. These variables are illustrated in the Gaia DR2 M_G vs. $G_{BP} - G_{RP}$ color-magnitude diagram (Figure 33).

The OGLE sample is dominated by sources at low

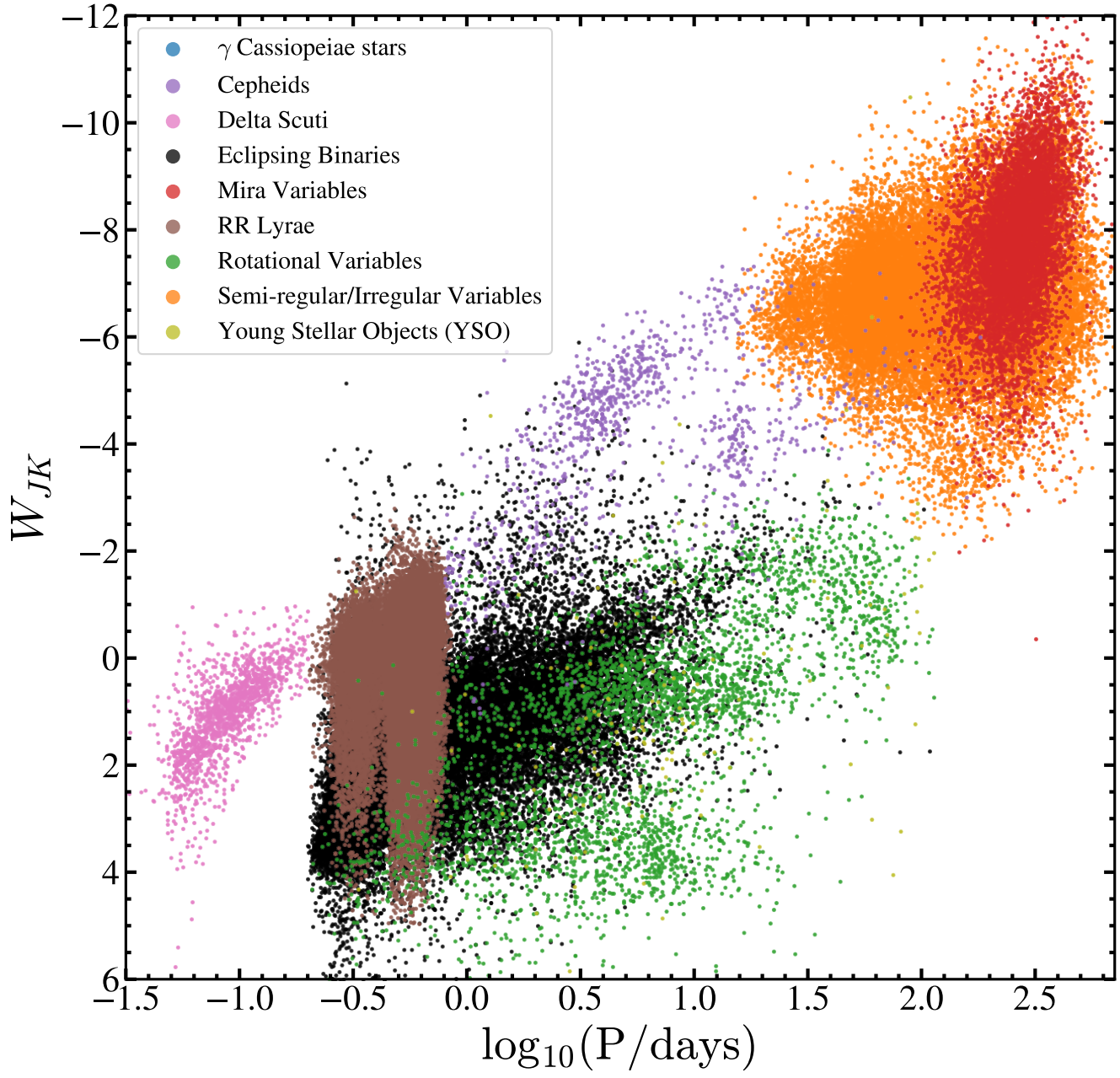

Figure 24. The Wesenheit W_{JK} PLR for the different classes of periodic variables in our training sample. The points are colored according as in Figure 22.

Galactic latitudes ($|b| < 10$ deg) and sources in the Magellanic clouds that are heavily affected by crowding and blending. Multiple stellar sources are likely to be found within the ASAS-SN FWHM (~16.″0) towards these regions. The cross-matching error rate to external photometric catalogs also increases towards crowded fields. Thus, crowding/blending can significantly affect the classification of variables.

The reclassification of these sources is more likely to be correct for those variables with high amplitude variability signals in the ASAS-SN light curves than for the low amplitude variables that are significantly affected by crowding/blending. This problem is evident in the small numbers of OGLE variables that have high classification probabilities— only ~50% (~51%) of these variables have classification probabilities of >0.9 (>0.75). Most of the variables with classification probabilities Prob > 0.9 are red giants with large variability amplitudes, as expected. Of the OGLE variables, 41% have matching variability classes and 93% of the OGLE variables with matching variability classes fall into the SR/IRR class. Of the OGLE variables with discrepant variable classes, 73% have uncertain classifications in ASAS-SN. Of the OGLE variables with discrepant classes, 67% are originally classified into the RRAB, RRC/RRD and

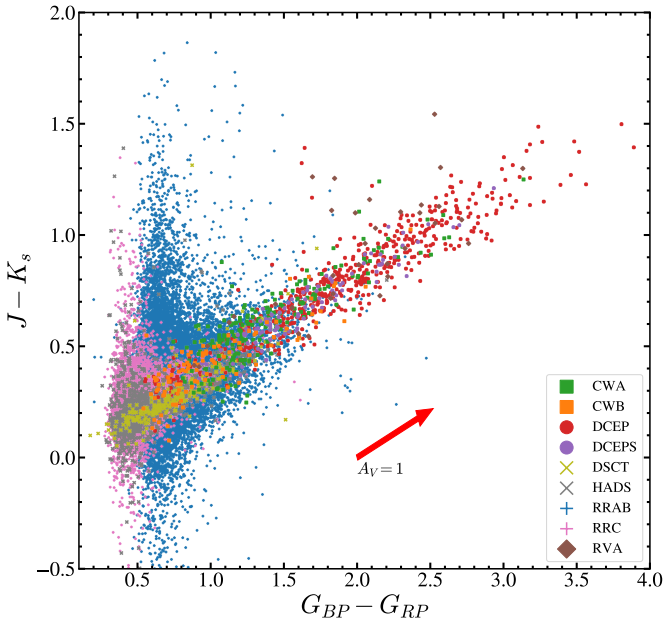

Figure 25. The Gaia DR2-2MASS $G_{BP}-G_{RP}$ vs $J-K_s$ color-color diagram for the RR Lyrae, Delta Scuti and Cepheid variables. The reddening vector corresponding to an extinction of $A_V = 1$ mag is shown in red.

ECL classes, further indicative of the blending and crowding issues towards these fields.

4.3 Sources with low V1 classification probabilities

Finally, we analyzed the ~47,000 variables that had discrepant classifications between VSX and the V1 classifier or were excluded from the initial training set due to low V1 classification probabilities (§3.5). A large fraction of these variables are assigned uncertain classifications (37%) by the V2 classifier and only 25% (31%) of these variables have classification probabilities of >0.9 (>0.75). A large fraction (40%) of these sources are located towards low Galactic latitudes ($|b| < 10$ deg) and so they will be more affected by crowding and extinction.

5 ESTIMATING VARIABILITY AMPLITUDES THROUGH RANDOM FOREST REGRESSION

In Paper I, we calculated the variability amplitude A as the difference between the 5th and 95th percentiles in magnitude. While this is well defined, it is not ideal as it ignores 10% of the data. Simply consider the case of eclipsing binaries—this approach will ignore the deepest parts of narrow eclipses and thus underestimate the variability amplitude.

In our new analysis, we instead use Random Forest Regression to estimate the amplitudes. A Random Forest regressor uses decision trees (much like a random forest classifier) to fit a model to the data (Breiman 2001; Klusowski 2018). This technique is useful because it does not assume a particular model when fitting the data. Unlike Fourier models, one can use RF regression for multi-periodic or irregular sources. RF regression models are also likely to work better for the light curves of detached eclipsing binaries.

We use different RF regression models to fit the light curves of periodic and irregular sources. For the light curves of periodic variables, we fit a RF regression model to the phased light curve. In this case, we prune the trees at a depth of `max_depth=10` and set `min_samples_leaf=2`, to minimize the effect of outliers. For the light curves of irregular variables, we fit a RF regression model to the temporal light curves. The trees were pruned at a depth of `max_depth=16`. The light curves of irregular variables are sparsely populated in time when compared to the phased light curves of periodic variables in phase space, so we choose to keep `min_samples_leaf=1`. Similarly, we choose to increase the depth of the trees in the irregular RF regression model to better fit complex light curves. In both RF regression models, the number of decision trees in the forest was set to `n_estimators=800`.

The variability amplitude ($A_{\rm RFR}$) is calculated from a RF regression model $R(x)$ as

$$A_{\rm RFR} = R(x)_{max} - R(x)_{min}, \tag{10}$$

where x is either the phase or date. Each RF regression fit is assigned a score

$$R^2 = 1 - \frac{\sum_{i=1}^{\rm N}\left[(m_{\rm true} - m_{\rm pred})\right]}{\sum_{i=1}^{\rm N}\left[(m_{\rm true} - \overline{m}_{\rm true})^2\right]}, \tag{11}$$

where $m_{\rm true}$ is the ASAS-SN V-band magnitude and $m_{\rm pred}$ is the predicted magnitude for the same point from the RF regression model. The RFR score is in the range $0 \leq R^2 \leq 1$, with a perfect model having a RFR score of $R^2 = 1$. Example of these RF regression models for the light curves of periodic variables are shown in Figure 35. RF regression model fits for irregular sources are shown in Figure 36. The models are not perfect, but they are correctly estimating the variability amplitudes even for the irregular light curves shown in Figure 36.

We use the variability amplitudes derived from RF regression fits to illustrate the training sample in period-amplitude space (Figure 37) grouped by the variable groups described in Figure 22. The left panel illustrates the amplitudes calculated using RF regression, whereas the right panel shows the amplitudes for the same sources calculated based on the prescription in Paper I. It is clear that the biggest difference between these two methods lie in the calculation of variability amplitudes for eclipsing binaries. $A_{\rm RFR}$ clearly provides better estimates for the depths of eclipses than the competing method. We do not see major differences between the two methods for other variable types.

Table 7 shows the dependence of the amplitude $A_{\rm RFR}$ with the VSX type for the variables in the V2 training sample. In general, rotational variables have smaller variability amplitudes, with $A_{\rm RFR} < 0.5$ mag, than other variables at similar periods. The majority of the δ-Scuti sample consists of HADS variables rather than the lower amplitude DSCT variables. Eclipsing binaries with deep eclipses usually consist of two stars with very different temperatures, and such systems are relatively rare. Only 5% of the detached EA systems have $A_{\rm RFR} > 1.3$ mag. The distinction between semi-regular variables and Mira variables is simply set by the

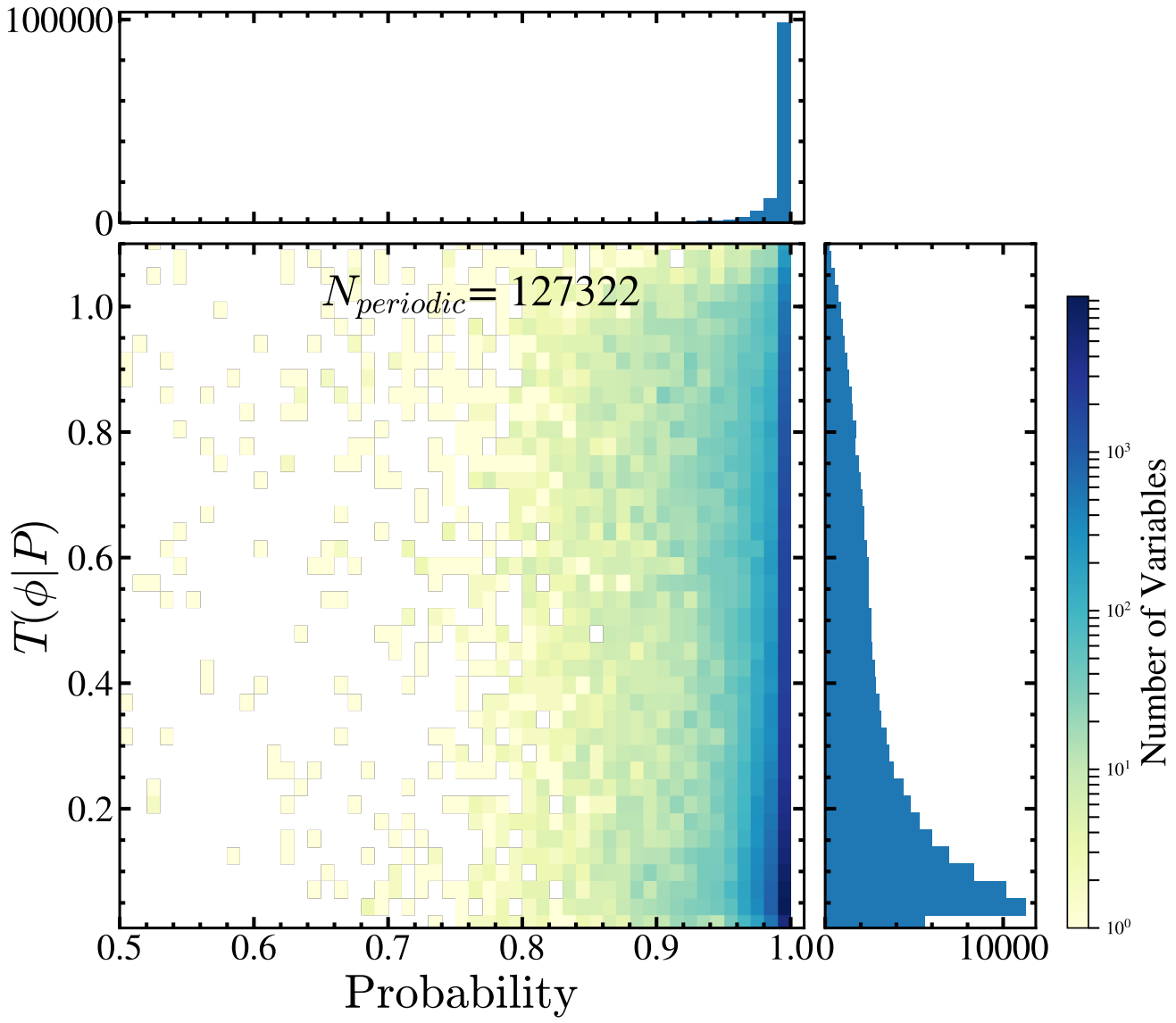

Figure 26. The distribution of the periodic variables in the training sample in $T(\phi|P)$ and classification probability.

amplitude cut ($A_{\rm RFR}$ > 2 mag) used in this work. The amplitudes of Mira variables can be as high as $A_{\rm RFR}$~5 mag. We reclassify high-amplitude ($A_{\rm RFR}$ > 2 mag) semi-regular variables as Mira variables provided that they also have a period P > 80 d.

We identify light curves that are likely to have problematic outliers if they satisfy either $\log {\rm P} < -0.7$ and $A_{\rm RFR} > 1.1$ mag OR $-0.7 \leq \log {\rm P} \leq 1.9$ and $A_{\rm RFR} > 2$ mag. These light curves are removed from our catalog if they also have an RFR score $R^2 < 0.8$ and $T(\phi|P)$>0.5. Only ~250 light curves were removed through this procedure.

We perform an additional check to identify problematic light curves by looking at the distribution of sources with uncertain classifications in the ($G_{BP} - G_{RP}$)-$A_{\rm RFR}$ color-amplitude space (Figure 38). The left panel shows the sources in the training sample and the right panel illustrates the ~115,000 sources with uncertain classifications. There is an abundance of sources that have uncertain classifications with $A_{\rm RFR} > 2$ mag and $G_{BP} - G_{RP} < 2.5$ mag. We visually verified that the light curves of these blue, high amplitude variables possess significant outliers. When looking at the distribution of the sources in the training sample in this region, we do not see this behavior. These variables were removed from our final catalog if their classification probabilities are Prob < 0.9. We removed ~3,000 such light curves through this procedure. The majority of the sources with $A_{\rm RFR} > 2$ mag and $G_{BP} - G_{RP} > 2.5$ mag are Mira variables without an ASAS-SN period.

6 DISCUSSION

We have homogeneously classified ~412,000 variables using our V2 variability classification pipeline. The classifier combines the ASAS-SN light curves with the data from Gaia

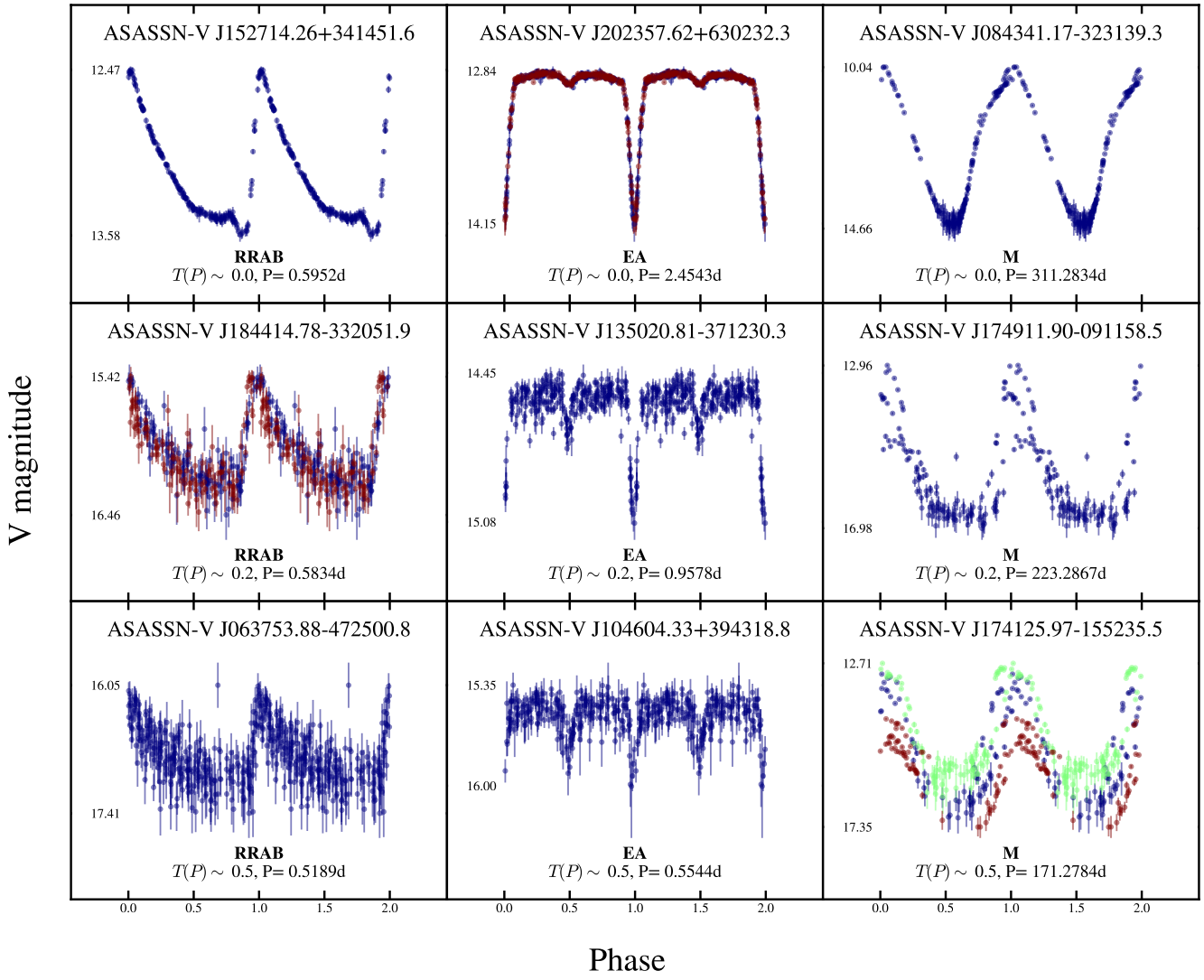

Figure 27. Examples of RRAB (left), EA (middle) and Mira (right) variables with varying $T(\phi|P)$. The format is the same as Figure 8.

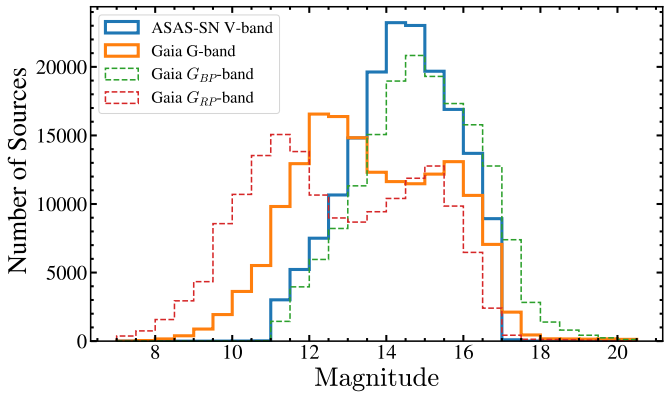

Figure 28. The distribution of the training sample in magnitude.

DR2, 2MASS and AllWISE surveys. This catalog provides a set of variables suitable for training automated variability classifiers for both existing and future variability surveys. We have refined the periods and classifications of ~356,000 variables with V-band magnitudes in the range $11 < V < 17$ mag, some of which were cataloged over ~50 years ago. The homogeneity of our classifications provides a useful point of comparison to the results from other projects. We also make the V-band light curves of the variables in this catalog available online at the ASAS-SN Variable Stars Database (https://asas-sn.osu.edu/variables). We started with ~440,000 variables with $11 < V < 17$ mag in the VSX catalog, and the final sample of ~356,000 is contained in the database. This includes both the ASAS-SN light curves and the ancillary data used in the classifications. The ~84,000 VSX variables that were dropped includes the sources with < 30 detections in the V-band, sources with excessively noisy or bad light curves, sources with variability types not included in this work (e.g., supernovae and exoplanet hosts), and the sources with variability amplitudes < 50 mmag. We also classified the ~56,000 sources with V-band magnitudes outside the range $11 < V < 17$ (see Appendix A). In §6.1,

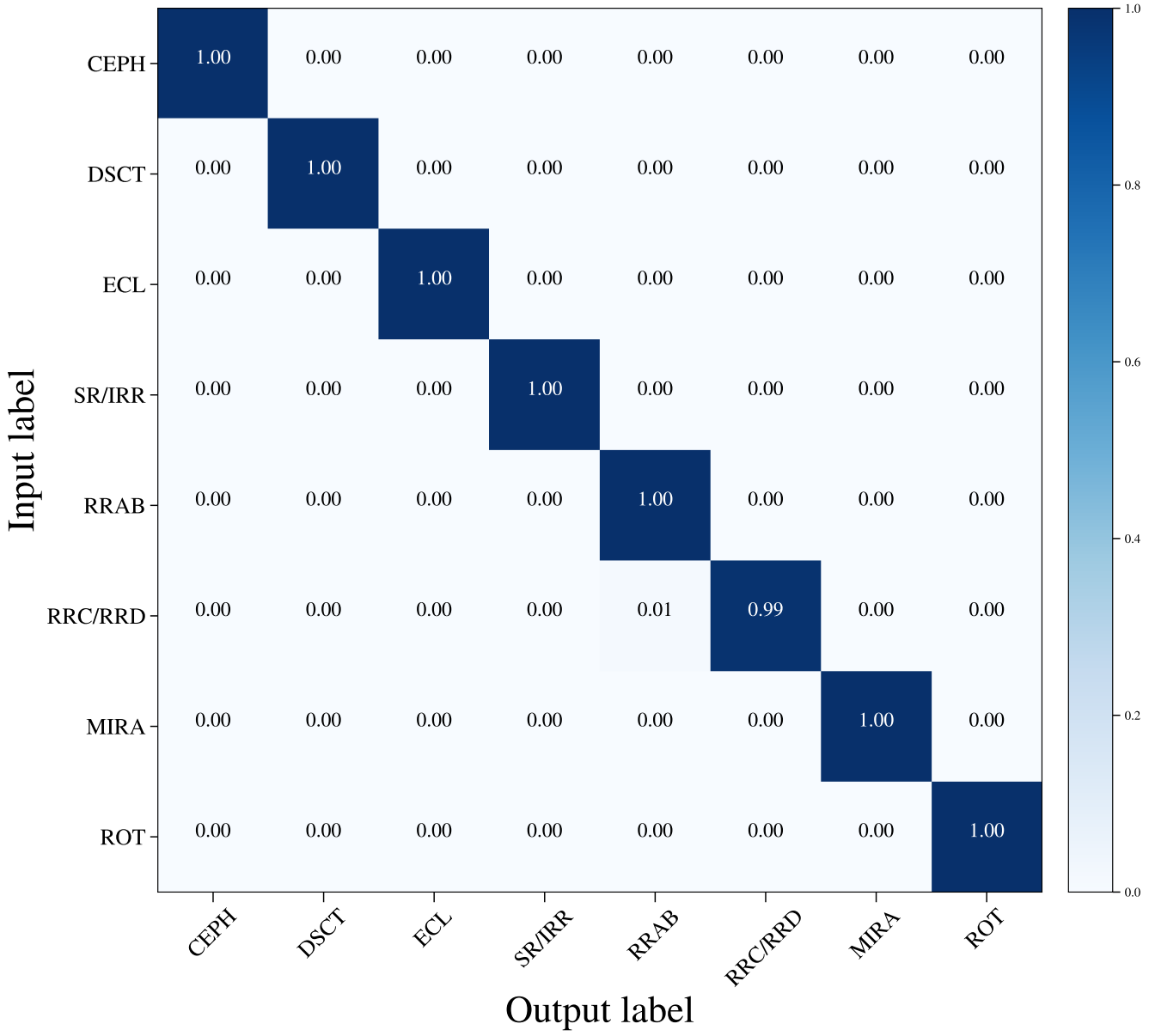

Figure 29. The normalized confusion matrix derived from the final version of the trained random forest classifier. The y-axis corresponds to the 'input' classification, while the x-axis is the 'output' prediction obtained from the trained random forest model.

we discuss the catalog of known variables. We discuss the rare variables added to our catalog in §6.2 and examine the spatial distribution of the variables in §6.3. For the subset of sources with both ASAS-SN and Gaia DR2 classifications, we compare the results of our classifier to the Gaia DR2 results in §6.4 and we discuss the implications of interstellar extinction on the classification pipeline in §6.5.

6.1 Catalog Properties

Here we discuss the catalog of ~356,000 variables with V-band magnitudes in the range $11 < V < 17$ mag. The catalog of known variables with V-band magnitudes outside this range is discussed in Appendix A. Definite classifications are the VSX types without the uncertainty flag ':'. Uncertain classifications include the variables classified as VAR and the VSX types with an uncertainty flag.

Table 8 lists the variability types from our classifier and the distribution of the ~278,000 variables with definite classifications by variability type. we also provide the number of high probability classifications (Prob > 0.9), good classifications (Prob > 0.5), and low scatter light curves ($T(\phi|P)$ or $T(t) < 0.5$). There are ~255,000 sources with Prob > 0.9, which forms a sample that is more than adequate to create a training set for future variability studies. In addition, there are ~177,000 variables with very good quality light curves where $T(\phi|P)$ or $T(t) < 0.5$.

Of the ~80,000 sources assigned uncertain classifications, ~2,000 were removed because of problems in the ASAS-SN light curves (see §5) to leave ~78,000 variables

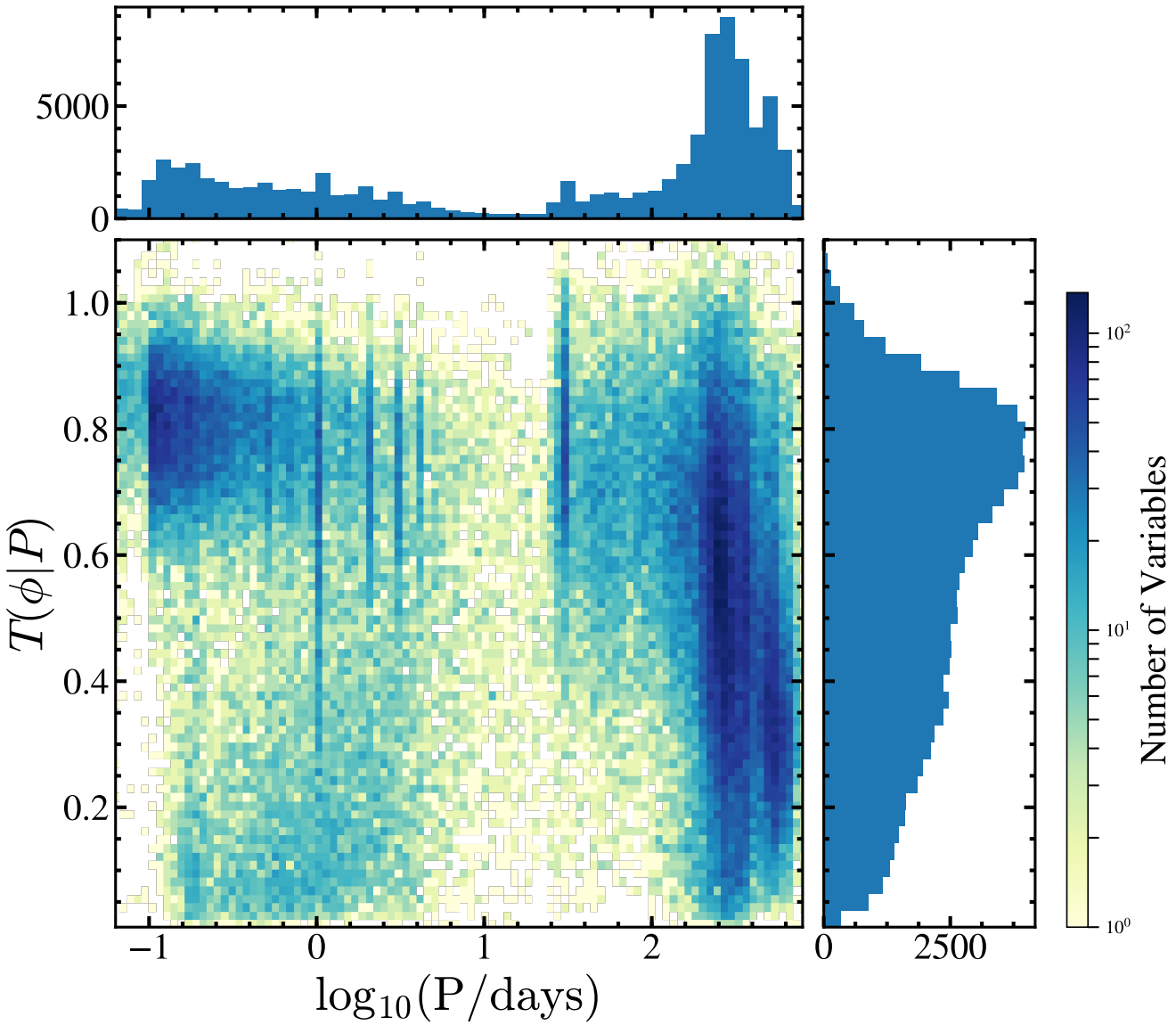

Figure 30. The distribution of the miscellaneous VSX variables with $T(\phi|P)$ and ASAS-SN log P.

with uncertain classifications. Table 9 presents their distribution by classification along with the number that do not have a Gaia DR2 parallax, a 2MASS match, a WISE match, a period in ASAS-SN, or have faint Gaia DR2 G_{BP}-band magnitudes ($G_{BP} > 19$ mag). The number of sources with $G_{BP} > 19$ mag is an indicator of the frequency of errors in cross-matching. Figure 28 suggests that the G_{BP}-band closely follows the ASAS-SN V-band magnitudes, hence very faint G_{BP}-band magnitudes likely arise from matches to the wrong source. The ROT: and VAR classes have the largest number of sources with $G_{BP} > 19$ mag, suggesting that these are the classes with the greatest amount of cross-matching errors.

A number of sources in the VSX catalog do not have previously derived periods, and we derive periods for ∼44,000 such sources. Of these, 81% have V2 classification probabilities Prob > 0.9 and 52% (18%) have $T(\phi|P) < 0.5$ ($T(\phi|P) < 0.2$). In the VSX catalog, most (73%) of these sources were classified as VAR variables, however, 67% of the ∼44,000 variables without a VSX period are classified as SR variables through our V2 classifier. A significant fraction (17%) were classified as eclipsing binaries.

Of the ∼291,000 VSX variables in our catalog with $11 < V < 17$ mag (excluding the variables from Paper I), ∼200,000 have definite VSX classifications. Out of the variables with definite VSX classifications, ∼65,000 sources have different broad variability classes than the ones assigned to them in the VSX catalog. ∼18,000 of these discrepant sources have high classification probabilities of Prob > 0.9.

Out of this set of ∼200,000 variables with definite VSX classifications, if we only consider just the ∼153,000 variables with definite ASAS-SN classifications, ∼23,000 sources have discrepant broad classes and ∼17,000 of these have classification probabilities of Prob > 0.9. We find that ∼4,700 (∼1,800)

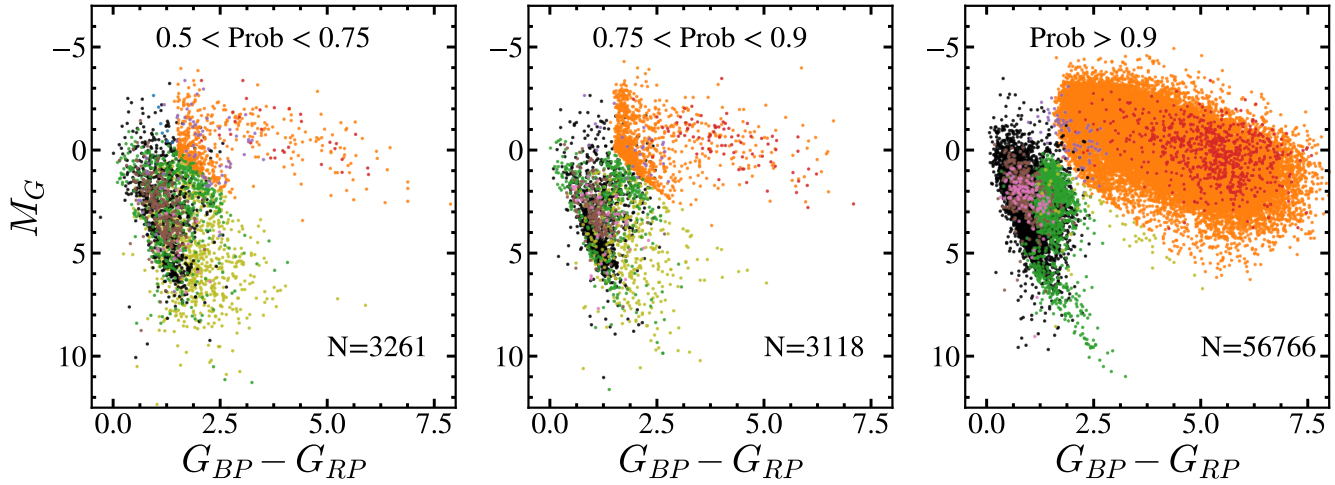

Figure 31. The Gaia DR2 M_G vs. $G_{BP} - G_{RP}$ color-magnitude diagram for the variables with miscellaneous classifications in VSX. *Left*: Variables with classification probability 0.5 < Prob < 0.75, *Middle*: Variables with classification probability 0.75 < Prob < 0.9, *Right*: Variables with classification probability Prob > 0.9. The points are colored as in Figure 22.

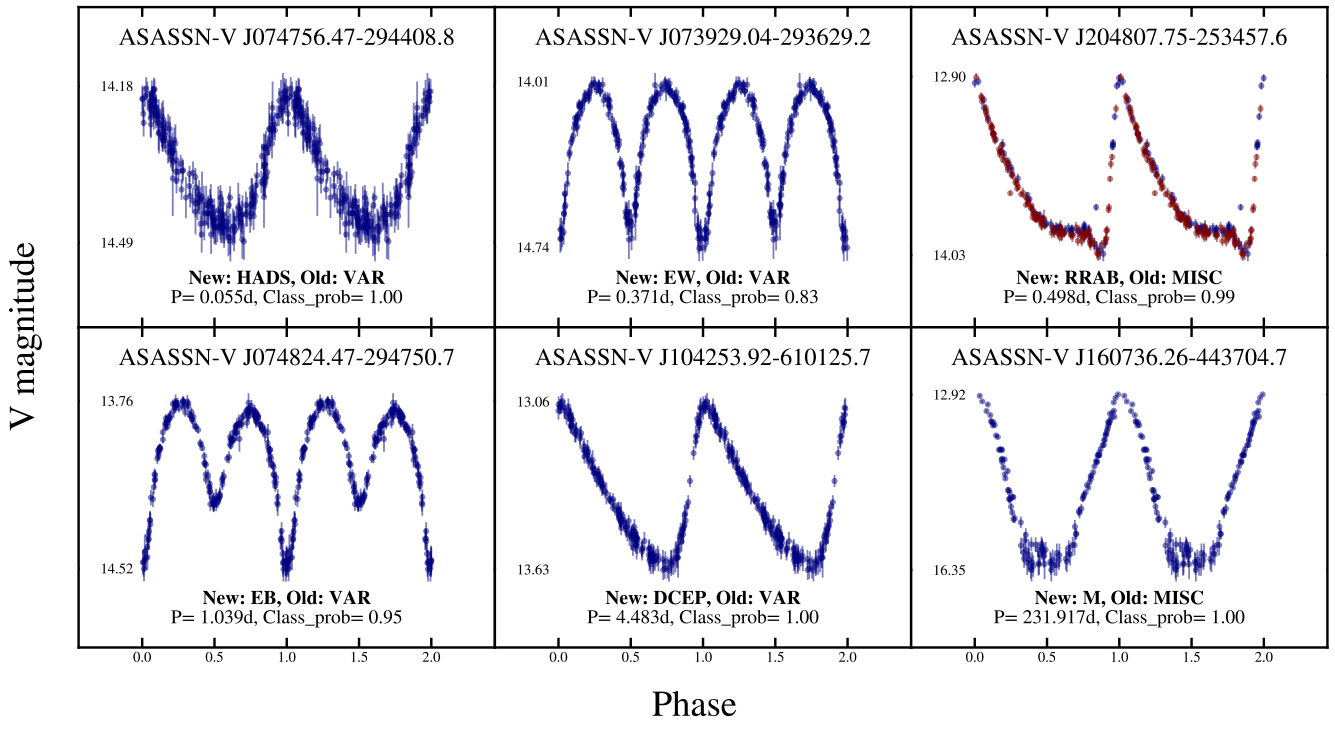

Figure 32. Examples of miscellaneous VSX variables with high probability classifications. The format is the same as Figure 8.

variables that were previously classified as Mira variables are reclassified as semi-regular (irregular) variables in ASAS-SN. It is likely that the majority of these sources are actually Mira variables but have diminished amplitudes in ASAS-SN due to blending.

In addition, we have homogenized the sample of eclipsing binaries in this catalog by classifying their light curves into the photometric eclipsing binary classes defined in the VSX catalog (i.e, EA, EB and EW). We assigned new VSX classes to ~6,000 eclipsing binaries that were classified based on their physical configuration (i.e, EC, ESD and ED).

Of the ~66,000 ASAS-SN variables, ~61,000 were classified into variable types other than VAR in Paper I. From these ~61,000 sources, ~5,000 have different broad classes in this work, out of which ~1,400 have classification probabilities Prob > 0.9. We also reclassify the ~5,000 VAR variables in Paper I to other variable types in this work. We have also broken the degeneracy in the EA|EB classification and

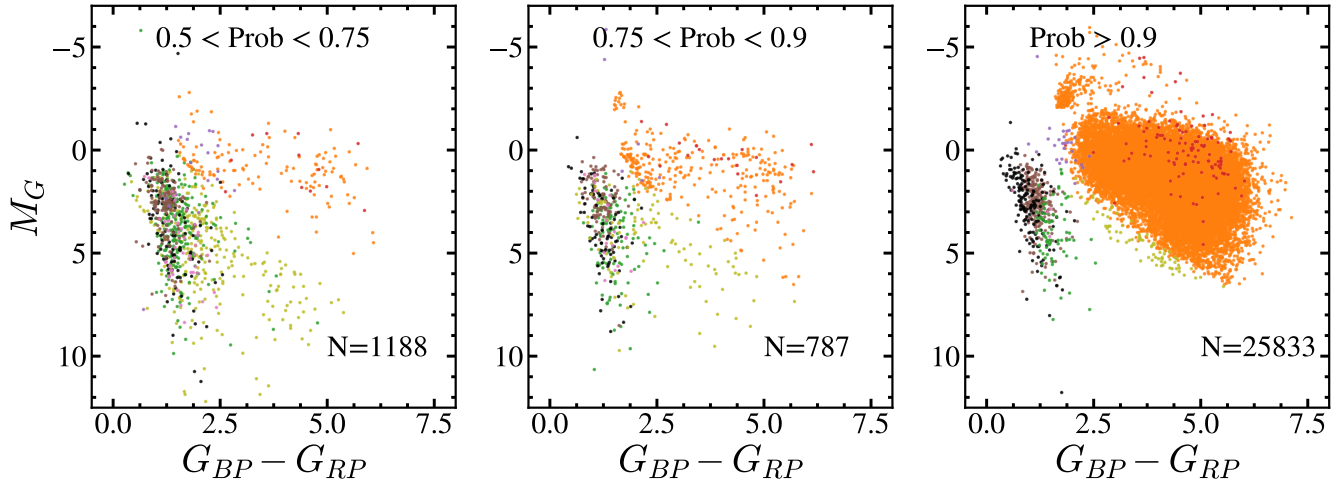

Figure 33. The Gaia DR2 M_G vs. $G_{BP} - G_{RP}$ color-magnitude diagram for the sample of OGLE variables that were analyzed with the classification pipeline. *Left*: Variables with classification probability 0.5 < Prob < 0.75, *Middle*: Variables with classification probability 0.75 < Prob < 0.9, *Right*: Variables with classification probability Prob > 0.9. The points are colored as in Figure 22.

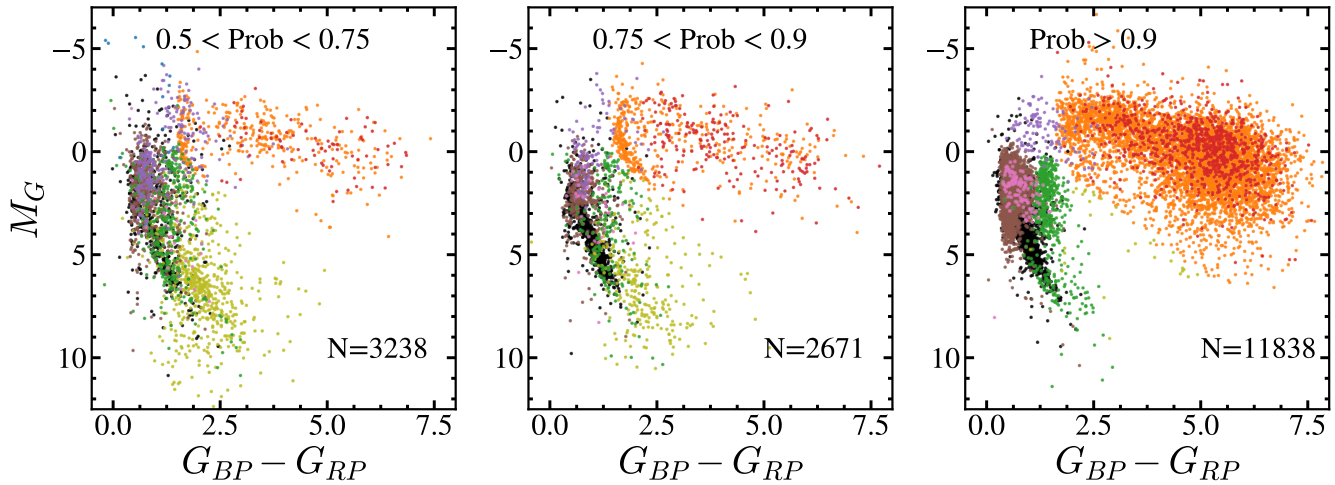

Figure 34. The Gaia DR2 M_G vs. $G_{BP} - G_{RP}$ color-magnitude diagram for the sample of variables with low V1 classification probabilities. *Left*: Variables with classification probability 0.5 < Prob < 0.75, *Middle*: Variables with classification probability 0.75 < Prob < 0.9, *Right*: Variables with classification probability Prob > 0.9. The points are colored as in Figure 22.

refined the classification of Cepheids and YSOs from Paper I.

6.2 Rare Variables

We also include the light curves of ~4,000 rare or transient variable types. This includes the light curves of cataclysmic variables, R Coronae Borealis variables, flare stars, variable white dwarfs and symbiotic variables. These have not been classified by our pipeline, however we have run periodograms, searched for best periods, and computed variability amplitudes through RF regression. We generally just retain the VSX classification, but opt to simplify degenerate classifications (ex: ZAND|EA) into a single classification (i.e, ZAND) for simplicity. Examples of these variables are shown in Figure 39.

During this work, we also identified a long period detached eclipsing binary system that was previously misclassified as an irregular variable (Jayasinghe et al. 2018b). ASASSN-V J192543.72+402619.0 is one of the longest period detached eclipsing binary systems known, with an orbital period of P~2679 d. The systematic variability analysis of the ~50 million V < 17 mag APASS sources in ASAS-SN will likely identify similar long period eclipsing binary systems. We also identified two other R Coronae Borealis (RCB) candidates during the analysis of the SR/IRR class (ASASSN-V J 043259.32+415854.0, ASASSN-V J 175700.51-213934.5). These sources and 17 other RCB candidates discovered in ASAS-SN are discussed in Shields et al. (2018).

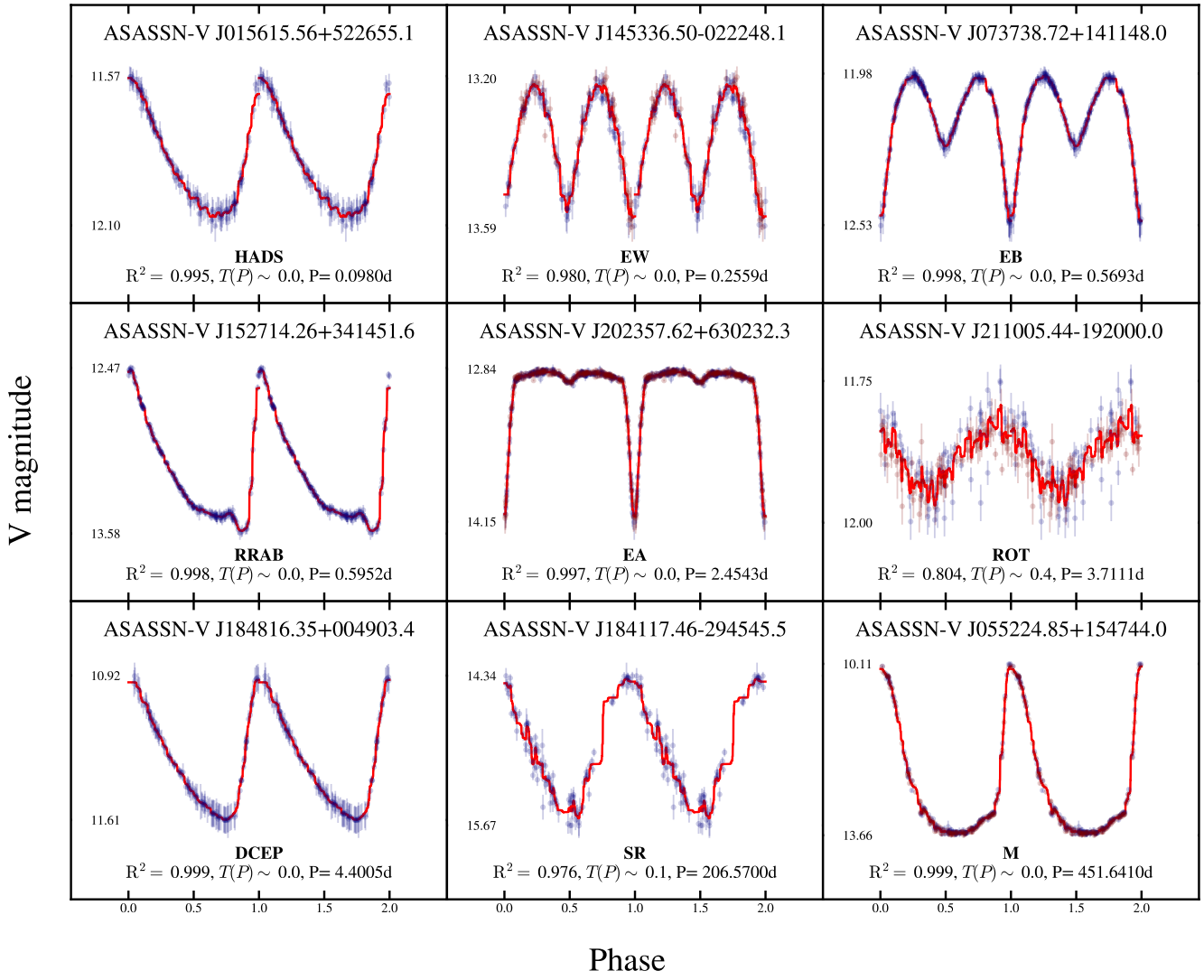

Figure 35. Random Forest Regression fits for periodic variables. The RF Regression model is plotted in red.

6.3 Spatial Distribution of the Variable Stars

The spatial distribution of the ∼412,000 classified variables is shown as a sky density plot in Figure 40. There is an abundance of sources towards the Galactic plane, and ASAS-SN's ability to provide truly all-sky coverage is evident. Lighter colors denote higher classification probability. We see that classification probabilities increase away from the Galactic plane. The effects of crowding hamper more accurate classifications closer to the Galactic disk and the Magellanic clouds.

6.4 Comparison to the Gaia DR2 Catalog of Variable Stars

In order to compare the classifications for the variables identified by Gaia DR2 and the ASAS-SN classifications, we cross-matched the ∼412,000 variables in this work to the list of ∼391,000 Gaia DR2 variables listed in the Specific Object Studies (SOS) variables list using the Gaia DR2 `source_id` (Holl et al. 2018). The mean G_{BP}-band magnitude for these sources ranges from G_{BP}∼16.4 mag to G_{BP}∼18.2 depending on the class of variable, suggesting that a large fraction of these sources are outside the ASAS-SN V-band detection threshold (Holl et al. 2018). We identified ∼23,000 variables that had both ASAS-SN and Gaia DR2 classifications. We group their classifications into broad classes for comparison and list the percentage of sources with matching ASAS-SN and Gaia DR2 classifications in Table 10. The SR/IRR and MIRA variables were grouped into a single class since Gaia DR2 classifications provided general classifications did not distinguish between them.

Most of the Gaia DR2 classifications agree very well with the ASAS-SN classifications, however the CEPH (71 %) and RRC/RRD (84%) classes show large discrepancies. The discrepancy for the CEPH class is largely due to sources with periods close to P∼1 d. Our classification pipeline does not enforce a lower bound on the periods of Cepheids at P∼1 d, but allows for sources falling on the Cepheid PLRs that are initially classified as RRAB with $P \gtrsim 0.9$ d to be reclas-

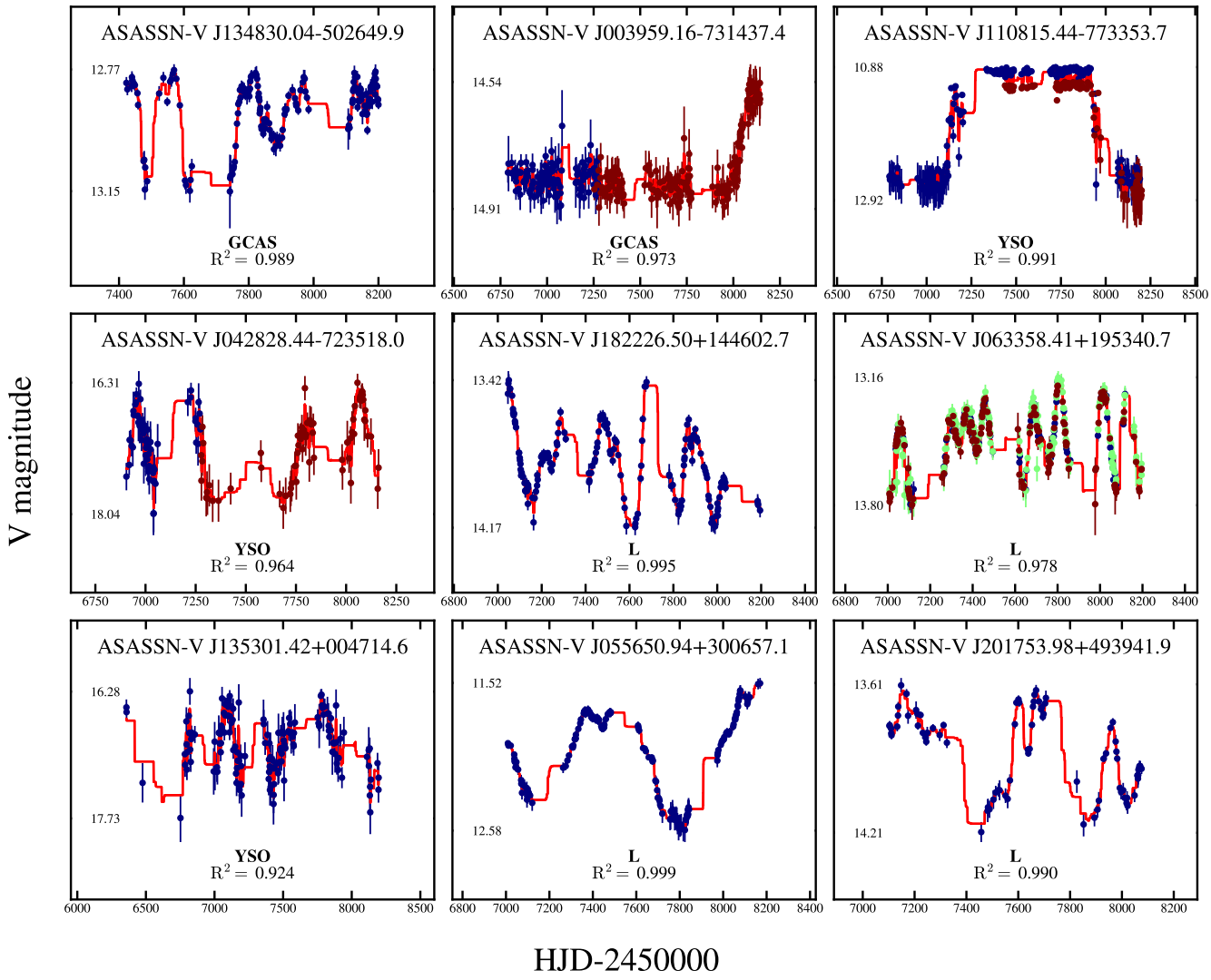

Figure 36. Random Forest Regression fits for irregular variables. The RF Regression model is plotted in red. The format is the same as Figure 35.

sified as Cepheids. These sources remain as RRAB in the Gaia DR2 catalog, and account for 64% of the discrepant classifications. However, we note that it is challenging to disentangle the PLRs of all-sky RR Lyrae and short period Cepheids near P~1 d owing to the distance uncertainties in the current Gaia DR2 catalog (Clementini et al. 2018). The remainder of the discrepancies are due to the classification of long period Cepheids as semi-regular/Mira variables in the Gaia DR2 catalog. The Gaia DR2 light curves are sparsely sampled when compared to the ASAS-SN light curves, thus it is likely that our classification of these long period variables as semi-regular/Mira variables is accurate. The discrepancy in the RRC/RRD class is largely due to sources classified as RRAB in the ASAS-SN pipeline.

6.5 Effects of Interstellar Extinction on the ASAS-SN Variability Classifications

Our variability classification pipeline uses observed colors and Wesenheit magnitudes. While we account for the effects of reddening in the absolute magnitudes with the use of Wesenheit magnitudes, we do not correct for extinction in the colors.

To evaluate the effects of extinction on our classifications, we selected a sample of ~167,000 variables with estimates of the extinction in Gaia DR2 (Gaia Collaboration et al. 2018a; Andrae et al. 2018). The extinctions in the J, H, K_s, $W1$ and $W2$ bands are calculated using the Gaia DR2 extinction estimate A_G as

$$A_\lambda = A_G \left(\frac{A_V}{A_G}\right)\left(\frac{A_\lambda}{A_V}\right), \quad (12)$$

where A_G/A_V = 0.85926, A_J/A_V = 0.29434, A_H/A_V = 0.18128, A_{K_s}/A_V = 0.11838, A_{W1}/A_V = 0.07134 and A_{W2}/A_V = 0.05511. We note that the relationship between

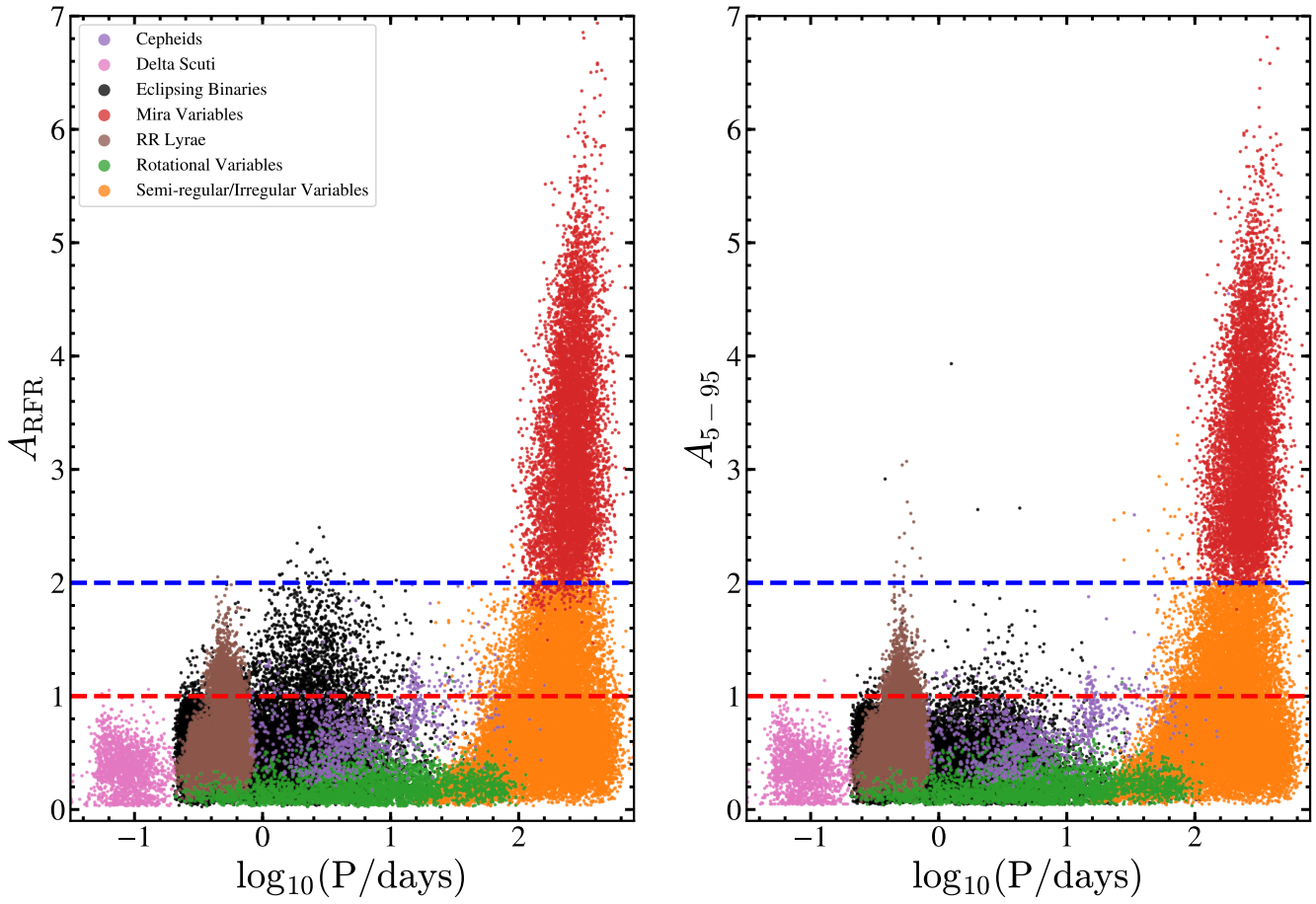

Figure 37. Period-amplitude plot for the variables in our training sample under the two methods of calculating amplitudes, the RFR method used in this paper ($A_{\rm RFR}$, left) and the 5-95% spread used in Paper I (A_{5-95}, right). Reference amplitudes of 1 and 2 mag are shown in red and blue respectively. The points are colored according to the prescription in Figure 22. The differences are most noticeable for eclipsing binaries.

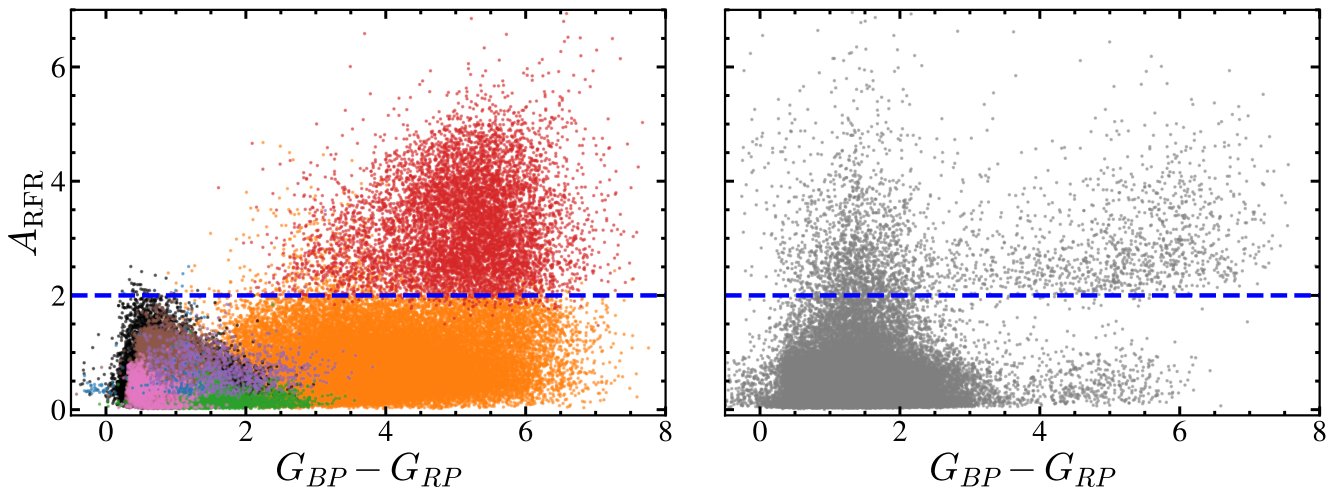

Figure 38. Color-amplitude plot for the variables with certain (left) and uncertain (right) classifications in our catalog. A reference amplitude of 2 mag is shown in blue. The points in the left panel are colored according to the prescription in Figure 22 and the variables with uncertain classifications are colored in gray.

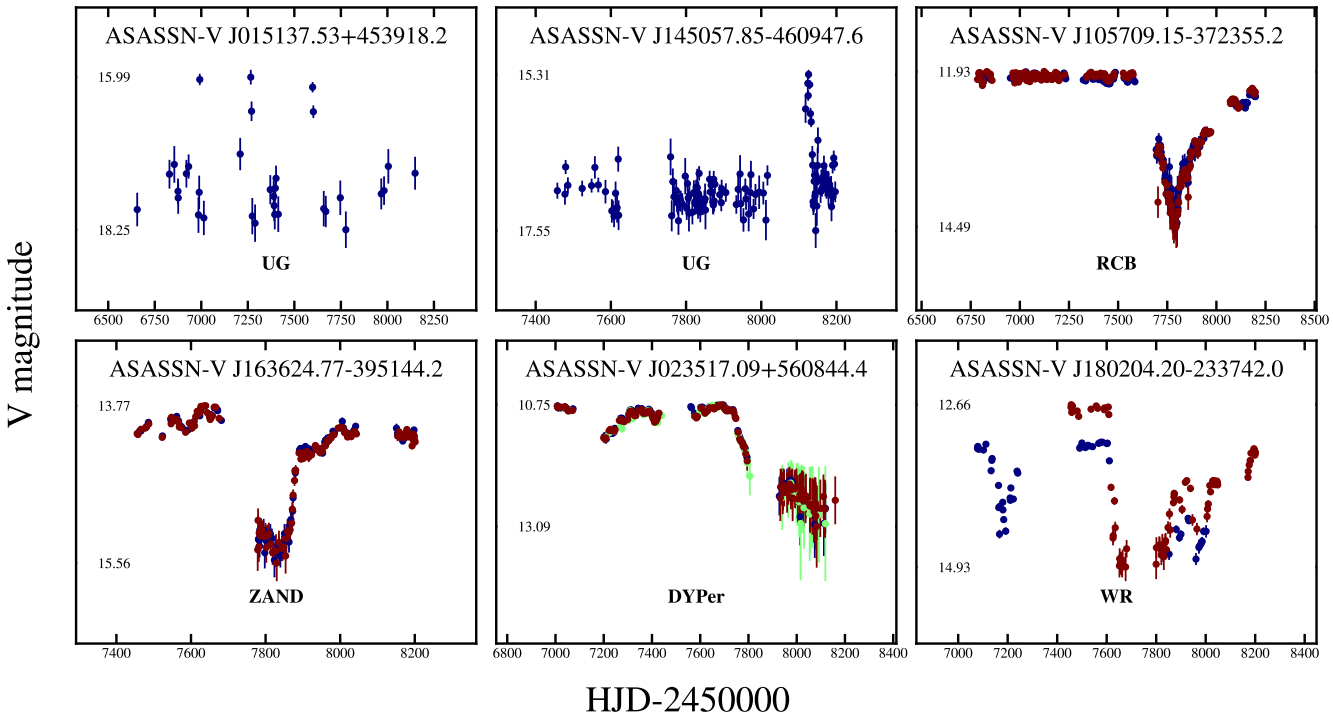

Figure 39. Light curves of sources included in the ASAS-SN variable stars database that were not classified in the ASAS-SN pipeline. The format is the same as Figure 8. The classifications used here are from the VSX catalog.

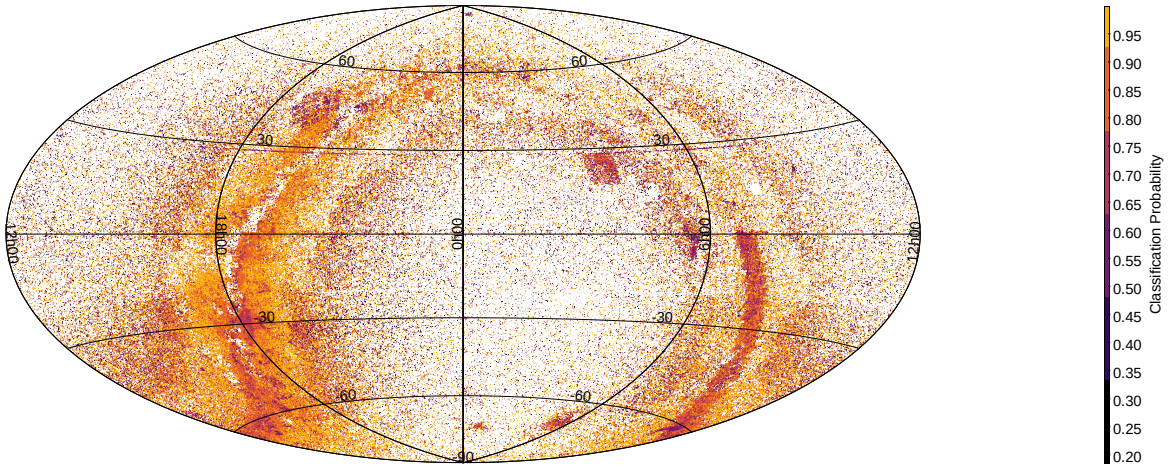

Figure 40. Density plot highlighting the spatial distribution of the ~412, 000 classified variables, shaded by their classification probability, in equatorial coordinates.

A_G and A_V is non-trivial (Andrae et al. 2018), but we have made this assumption to allow a simple evaluation of the problem.

Using the same variability classification pipeline, we re-classified these variables after correcting their $G_{BP} - G_{RP}$, $J - H$, $J - K_s$, and $W1 - W2$ colors for extinction. We only consider the ~108, 000 variables with Prob > 0.9 in order to select a test sample with well defined variable sources. The fraction of classifications which do not change is listed in Table 11. The RR Lyrae (RRAB, RRC, RRD), Cepheids (DCEPS, DCEP, CWA, CWB), eclipsing binaries (EA, EB, EW), δ Scuti (HADS), semi-regular variables (SR), Mira variables (M), rotational variables (ROT) and red, irregular variables (L) all have excellent recovery rates ($\gtrsim$ 96%).

On the other hand, sources with recovery rates < 96% include yellow semi-regular (SRD) and YSO variables. GCAS and RVA variables often have low RF classification probabilities and so were not included in the test sample. YSOs are typically located towards Galactic star forming regions, which by their nature have high extinction. Hence,

Table 7. Distribution of $A_{\rm RFR}$, in magnitudes, with variability type for the V2 classifier training sample. The median, standard deviation, 5$^{\rm th}$ percentile and 95$^{\rm th}$ percentile for $A_{\rm RFR}$ for each class is given.

VSX Type	Median	σ	5$^{\rm th}$ percentile	95$^{\rm th}$ percentile
CWA	0.87	0.26	0.46	1.22
CWB	0.81	0.26	0.40	1.27
DCEP	0.66	0.22	0.40	1.05
DCEPS	0.36	0.08	0.26	0.51
DSCT	0.08	0.03	0.04	0.14
EA	0.50	0.35	0.18	1.30
EB	0.39	0.20	0.17	0.80
EW	0.41	0.17	0.18	0.74
HADS	0.39	0.16	0.19	0.70
M	3.14	0.82	2.12	4.71
ROT	0.18	0.12	0.06	0.44
RRAB	0.81	0.25	0.37	1.19
RRC	0.46	0.12	0.25	0.67
RRD	0.72	0.21	0.37	1.07
RVA	0.96	0.50	0.46	1.41
SR	0.56	0.44	0.17	1.62
SRD	0.38	0.36	0.15	1.25
GCAS	0.36	0.40	0.30	1.3
L	0.57	0.40	0.26	1.45
YSO	0.82	0.51	0.14	1.77

the observed magnitudes for YSO variables are more likely to suffer from extinction when compared to other variability types. Furthermore, the Gaia DR2 extinction estimates for the YSO variables effectively also include the circumstellar extinction which drives the near/mid-infrared colors used to identify them. Hence, it is not surprising that the identification of YSOs is strongly affected by this test.

7 CONCLUSIONS

We uniformly analyzed the ASAS-SN light curves of ~412,000 known variables from the VSX catalog. We analyzed all the sources for periodicity and were able to determine periods for ~44,000 VSX variables lacking them. We homogeneously estimated the variability amplitudes using random forest regression. Using the RF classifier from Paper I and a series of classification corrections based in large part on using Gaia DR2 parallax information, we built a clean training sample of ~166,000 variables. We used this to build a refined RF classifier. The new classifier has an overall F_1 score of 99.4%, a considerable improvement over Paper I. We then use this V2 classifier on the complete sample of variables and provide new classifications for ~94,000 variables with miscellaneous classifications. We also classified the variables with mean magnitudes outside the magnitude range $11 < V < 17$ mag, but these should be used with caution.

We provide definite classifications for ~278,000 VSX variables, of which ~17,000 have different broad variability classifications than VSX to high confidence. Most of these changes are from the refinements in classifying RR Lyrae, δ-Scuti, eclipsing binaries and the semi-regular and irregular variables. We also include the light curves of ~4,000 rare and transient variables on the ASAS-SN Variable Stars Database (https://asas-sn.osu.edu/variables). We have updated the ASAS-SN Variable Stars Database with new photometric, Gaia DR2 distance, classification quality and light curve quality information. This sample provides an excellent, homogeneously classified training set of variables for both current and future all-sky surveys. A full variability analysis of the ~50 million APASS sources brighter than V~17 mag is currently underway.

ACKNOWLEDGEMENTS

We thank the Las Cumbres Observatory and its staff for its continuing support of the ASAS-SN project. We also thank the Ohio State University College of Arts and Sciences Technology Services for helping us set up and maintain the ASAS-SN variable stars database.

ASAS-SN is supported by the Gordon and Betty Moore Foundation through grant GBMF5490 to the Ohio State University and NSF grant AST-1515927. Development of ASAS-SN has been supported by NSF grant AST-0908816, the Mt. Cuba Astronomical Foundation, the Center for Cosmology and AstroParticle Physics at the Ohio State University, the Chinese Academy of Sciences South America Center for Astronomy (CAS- SACA), the Villum Foundation, and George Skestos.

TAT is supported in part by Scialog Scholar grant 24215 from the Research Corporation. Support for JLP is provided in part by FONDECYT through the grant 1151445 and by the Ministry of Economy, Development, and Tourism's Millennium Science Initiative through grant IC120009, awarded to The Millennium Institute of Astrophysics, MAS. SD acknowledges Project 11573003 supported by NSFC. Support for MP and OP has been provided by the PRIMUS/SCI/17 award from Charles University.

This work has made use of data from the European Space Agency (ESA) mission *Gaia* (https://www.cosmos.esa.int/gaia), processed by the *Gaia* Data Processing and Analysis Consortium (DPAC, https://www.cosmos.esa.int/web/gaia/dpac/consortium). Funding for the DPAC has been provided by national institutions, in particular the institutions participating in the *Gaia* Multilateral Agreement.

This publication makes use of data products from the Wide-field Infrared Survey Explorer, which is a joint project of the University of California, Los Angeles, and the Jet Propulsion Laboratory/California Institute of Technology, funded by the National Aeronautics and Space Administration.

This research was made possible through the use of the AAVSO Photometric All-Sky Survey (APASS), funded by the Robert Martin Ayers Sciences Fund. This publication makes use of data products from the Two Micron All Sky Survey, which is a joint project of the University of Massachusetts and the Infrared Processing and Analysis Center/California Institute of Technology, funded by the National Aeronautics and Space Administration and the National Science Foundation.

This research has made use of the VizieR catalogue access tool, CDS, Strasbourg, France. The original description of the VizieR service was published in A&AS 143, 23.

This research made use of Astropy, a community-

Table 8. Number distribution of the ~278, 000 variables with definite classifications by quality cuts and magnitude.

VSX Type	$N_{\rm tot}$	N(Prob > 0.9)	N(Prob > 0.5)	$N[T(\phi\|P)$ or $T(t) < 0.5]$
CWA	419	261	355	381
CWB	508	76	309	432
DCEP	752	588	706	705
DCEPS	160	129	150	154
DSCT	375	328	375	158
EA	17979	16135	17653	14144
EB	9557	8862	9443	8152
EW	37220	34683	36986	28352
GCAS	215	0	23	89
HADS	1521	1381	1519	1269
L	62655	60904	62202	37077
M	11029	10198	10995	9709
ROT	7824	4969	7114	3613
RRAB	29150	26575	28522	24362
RRC	7740	6758	7634	6269
RRD	450	355	439	150
RVA	121	15	99	101
SR	84593	82265	83701	39667
SRD	734	563	732	413
YSO	5315	322	4023	1562

Table 9. Number distributions of the ~78, 000 variables with uncertain classifications.

VSX Type	$N_{\rm tot}$	No Parallax	No 2MASS	No AllWISE	No Period	$N(G_{BP} > 19)$
DSCT:	460	193	9	38	0	7
GCAS:	735	0	0	7	383	2
M:	1106	0	0	17	635	76
ROT:	45709	1	1	2833	40334	3488
RRAB:	55	5	3	13	0	5
VAR	30047	11763	1186	2536	22628	1589

Table 10. ASAS-SN variability classification matches for the ~23, 000 variables also listed in the Gaia DR2 catalog

Variability Class	$N_{\rm tot}$	Matched
CEPH	219	71%
SR/IRR+MIRA	14273	99%
DSCT	173	88%
RRAB	6866	100%
RRC/RRD	906	84%
ROT	43	100%

Table 11. Recovery rate of the ~108, 000 variables with high classification probability after correcting for extinction in their colors using the Gaia DR2 extinction estimates.

VSX Type	Recovery Rate
CWA	98%
CWB	100%
DCEP	98%
DCEPS	100%
DSCT	91%
EA	100%
EB	99%
EW	100%
HADS	99%
L	99%
M	100%
ROT	97%
RRAB	100%
RRC	99%
RRD	96%
SR	96%
SRD	86%
YSO	75%

developed core Python package for Astronomy (Astropy Collaboration, 2013).

REFERENCES

Alard, C. 2000, A&AS, 144, 363

Alard, C., & Lupton, R. H. 1998, ApJ, 503, 325

Alcock, C., Allsman, R. A., Alves, D., et al. 1997, ApJ, 486, 697

Alksnis, A., Balklavs, A., Dzervitis, U., et al. 2001, Baltic Astronomy, 10, 1

Andrae, R., Fouesneau, M., Creevey, O., et al. 2018, A&A, 616, A8

Armstrong, D. J., Kirk, J., Lam, K. W. F., et al. 2016, MNRAS, 456, 2260

Astropy Collaboration, Robitaille, T. P., Tollerud, E. J., et al. 2013, A&A, 558, A33

Bailer-Jones, C. A. L., Rybizki, J., Fouesneau, M., Mantelet, G., & Andrae, R. 2018, AJ, 156, 58

Baraffe, I., & Alibert, Y. 2001, A&A, 371, 592

Bernhard, K., Otero, S., Hümmerich, S., et al. 2018, MNRAS, 479, 2909

Bhatti, W., Bouma, L. G., Wallace, J., et al. 2018, astrobase, v0.3.8, Zenodo, http://doi.org/10.5281/zenodo.1185231
Bonanos, A. Z., Stanek, K. Z., Sasselov, D. D., et al. 2003, AJ, 126, 175
Breiman, L. 2001, Machine Learning, 45, 1
Breger, M. 1979, PASP, 91, 5
Brown, T. M., Baliber, N., Bianco, F. B., et al. 2013, PASP, 125, 1031
Chen, X., Deng, L., de Grijs, R., Wang, S., & Feng, Y. 2018, ApJ, 859, 140
Clarke, D. 2002, A&A, 386, 763
Clementini, G., Ripepi, V., Molinaro, R., et al. 2018, arXiv:1805.02079
Cutri, R. M., & et al. 2013, VizieR Online Data Catalog, 2328,
Derue, F., Marquette, J.-B., Lupone, S., et al. 2002, A&A, 389, 149
Drake, A. J., Graham, M. J., Djorgovski, S. G., et al. 2014, ApJS, 213, 9
Gaia Collaboration, Brown, A. G. A., Vallenari, A., et al. 2018, arXiv:1804.09365
Gaia Collaboration, Eyer, L., Rimoldini, L., et al. 2018, arXiv:1804.09382
Graczyk, D., Pietrzyński, G., Thompson, I. B., et al. 2014, ApJ, 780, 59
Grady, J., Belokurov, V., & Evans, N. W. 2018, arXiv:1804.09186
Hamacher, D. W. 2018, The Australian Journal of Anthropology, Vol. 29(1), pp. 89-107, 2018., 29, 89
Heinze, A. N., Tonry, J. L., Denneau, L., et al. 2018, arXiv:1804.02132
Henden, A. A., Levine, S., Terrell, D., & Welch, D. L. 2015, American Astronomical Society Meeting Abstracts #225, 225, 336.16
Holl, B., Audard, M., Nienartowicz, K., et al. 2018, arXiv:1804.09373
Holoien, T. W.-S., Brown, J. S., Stanek, K. Z., et al. 2017, MNRAS, 471, 4966
Jayasinghe, T., Kochanek, C. S., Stanek, K. Z., et al. 2018, MNRAS, 477, 3145
Jayasinghe, T., Stanek, K. Z., Kochanek, C. S., et al. 2018, Research Notes of the American Astronomical Society, 2, 125
Jayasinghe, T., Kochanek, C. S., Stanek, K. Z., et al. 2018, Research Notes of the American Astronomical Society, 2, 18
Jetsu, L., Porceddu, S., Lyytinen, J., et al. 2013, ApJ, 773, 1
Kim, D.-W., & Bailer-Jones, C. A. L. 2016, A&A, 587, A18
Kinemuchi, K., Smith, H. A., Woźniak, P. R., McKay, T. A., & ROTSE Collaboration 2006, AJ, 132, 1202
Kiss, L. L., Szatmáry, K., Cadmus, R. R., Jr., & Mattei, J. A. 1999, A&A, 346, 542
Klusowski, J. M. 2018, arXiv:1805.02587
Kochanek, C. S., Shappee, B. J., Stanek, K. Z., et al. 2017, PASP, 129, 104502
Koenig, X. P., & Leisawitz, D. T. 2014, ApJ, 791, 131
Kovács, G., Zucker, S., & Mazeh, T. 2002, A&A, 391, 369
Lafler, J., & Kinman, T. D. 1965, ApJS, 11, 216
Lebzelter, T., Mowlavi, N., Marigo, P., et al. 2018, arXiv:1808.03659
Leavitt, H. S. 1908, Annals of Harvard College Observatory, 60, 87
Leavitt, H. S., & Pickering, E. C. 1912, Harvard College Observatory Circular, 173, 1
Lopez de Coca, P., Rolland, A., Rodriguez, E., & Garrido, R. 1990, A&AS, 83, 51
Ludendorff, H. 1928, Handbuch der Astrophysik, 6, 49
Madore, B. F. 1982, ApJ, 253, 575
Matsunaga, N., Fukushi, H., Nakada, Y., et al. 2006, MNRAS, 370, 1979
Mowlavi, N., Lecoeur-Taïbi, I., Lebzelter, T., et al. 2018, arXiv:1805.02035
Oelkers, R. J., Rodriguez, J. E., Stassun, K. G., et al. 2018, AJ, 155, 39
Olech, A., & Moskalik, P. 2009, A&A, 494, L17
Paczyński, B. 2000, PASP, 112, 1281
Paczyński, B., Szczygieł, D. M., Pilecki, B., & Pojmański, G. 2006, MNRAS, 368, 1311
Pawlak, M., Soszyński, I., Udalski, A., et al. 2016, Acta Astron., 66, 421
Pedregosa, F., Varoquaux, G., Gramfort, A., et al. 2012, arXiv:1201.0490
Pejcha, O., & Kochanek, C. S. 2012, ApJ, 748, 107
Pepper, J., Pogge, R. W., DePoy, D. L., et al. 2007, PASP, 119, 923
Percy, J. R., & Colivas, T. 1999, PASP, 111, 94
Pietrzyński, G., Graczyk, D., Gieren, W., et al. 2013, Nature, 495, 76
Pojmanski, G. 2002, Acta Astron., 52, 397
Poleski, R. 2014, PASP, 126, 509
Reimann, J. D. 1994, Ph.D. Thesis,
Ricker, G. R., Winn, J. N., Vanderspek, R., et al. 2015, Journal of Astronomical Telescopes, Instruments, and Systems, 1, 014003
Rodríguez, R., Schmidt, S. J., Jayasinghe, T., et al. 2018, Research Notes of the American Astronomical Society, 2, 8
Roth, Günter D. 1994, An Historical Exploration of Modern Astronomy in Compendium of Practical Astronomy, Springer-Verlag Berlin Heidelberg New York, 153
Rucinski, S. M. 1993, PASP, 105, 1433
Scargle, J. D. 1982, ApJ, 263, 835
Schaefer, B. E. 2018, Journal of Astronomical History and Heritage, 21, 7
Schwarzenberg-Czerny, A. 1996, ApJ, 460, L107
Shappee, B. J., Prieto, J. L., Grupe, D., et al. 2014, ApJ, 788, 48
Shields, J. V., Jayasinghe, T., Stanek, K. Z., et al. 2018, arXiv:1809.04075
Skrutskie, M. F., Cutri, R. M., Stiening, R., et al. 2006, AJ, 131, 1163
Soszynski, I., Udalski, A., Kubiak, M., et al. 2004, Acta Astron., 54, 129
Soszynski, I., Dziembowski, W. A., Udalski, A., et al. 2007, Acta Astron., 57, 201
Soszyński, I., Pawlak, M., Pietrukowicz, P., et al. 2016, Acta Astron., 66, 405
Soszyński, I., Udalski, A., Szymański, M. K., et al. 2017, Acta Astron., 67, 103
Stassun, K. G., Oelkers, R. J., Pepper, J., et al. 2018, AJ, 156, 102
Storm, J., Gieren, W., Fouqué, P., et al. 2011, A&A, 534, A94
Taylor, M. B. 2005, Astronomical Data Analysis Software and Systems XIV, 347, 29
Tonry, J. L., Denneau, L., Heinze, A. N., et al. 2018, PASP, 130, 064505
Torres, G., Andersen, J., & Giménez, A. 2010, A&ARv, 18, 67
Tucker, M. A., Shappee, B. J., Holoien, T. W.-S., et al. 2018, arXiv:1808.07875
Udalski, A. 2003, Acta Astron., 53, 291
Vanderplas, J. 2015, gatspy: General tools for Astronomical Time Series in Python (Version v0.1.1), Zenodo, http://doi.org/10.5281/zenodo.14833
VanderPlas, J. T. 2018, ApJS, 236, 16
Von Neumann, J., Kent, R., Bellinson, H., & Hart, B. T. 1941,The Annals of Mathematical Statistics, 12, 153
Watson, C. L., Henden, A. A., & Price, A. 2006, Society for Astronomical Sciences Annual Symposium, 25, 47
Whitelock, P. A., Feast, M. W., & Van Leeuwen, F. 2008, MNRAS, 386, 313
Windmark, F., Lindegren, L., & Hobbs, D. 2011, A&A, 530, A76

Wright, E. L., Eisenhardt, P. R. M., Mainzer, A. K., et al. 2010, AJ, 140, 1868
Woźniak, P. R., Vestrand, W. T., Akerlof, C. W., et al. 2004, AJ, 127, 2436
Zechmeister, M., & Kürster, M. 2009, A&A, 496, 577

APPENDIX A: SATURATED/FAINT SOURCES

Variables that maybe saturated ($V < 11$ mag) or faint ($V > 17$ mag) in ASAS-SN are not considered part of the primary analysis. However, we do include these ~56,000 sources in the ASAS-SN Variable Stars Database with classifications. We caution the reader to interpret these classifications carefully — saturation artifacts and noise hinder accurate variable classifications.

ASAS-SN uses an algorithm derived from the ASAS survey to correct the flux from the bleed trails of bright stars that saturate the detectors (Kochanek et al. 2017). In many cases, this leads to surprisingly good light curves for saturated sources. Figure A1 shows examples of periodic variables with $V < 11$ mag. Generally, acceptable light curves are obtained for periodic variables with mean magnitudes in the range $10 \leq V \leq 11$ mag. However, saturation artifacts are prominent in the sources with mean magnitudes $V < 9$ mag. We catalog ~34,000 variables with $V < 11$ mag.

ASAS-SN has a transient detection limit of $V \lesssim 17$ mag (see for e.g, Holoien et al. 2017). In some cases, sources with mean V-band magnitudes $V > 17$ mag provide useful information, particularly in the cases of high amplitude Mira variables and semi-regular variables (Figure A2). The detection of lower amplitude variables is increasingly difficult, and the light curves are noisy. We catalog ~22,000 variables with $V > 17$ mag.

Only ~30% (~26%) of these variables have classification probabilities of >0.9 (>0.75), while a majority (~64%) of these sources have uncertain classifications. We derive periods for ~6,000 saturated/faint variables that do not have a period in the VSX catalog.

This paper has been typeset from a TEX/LATEX file prepared by the author.

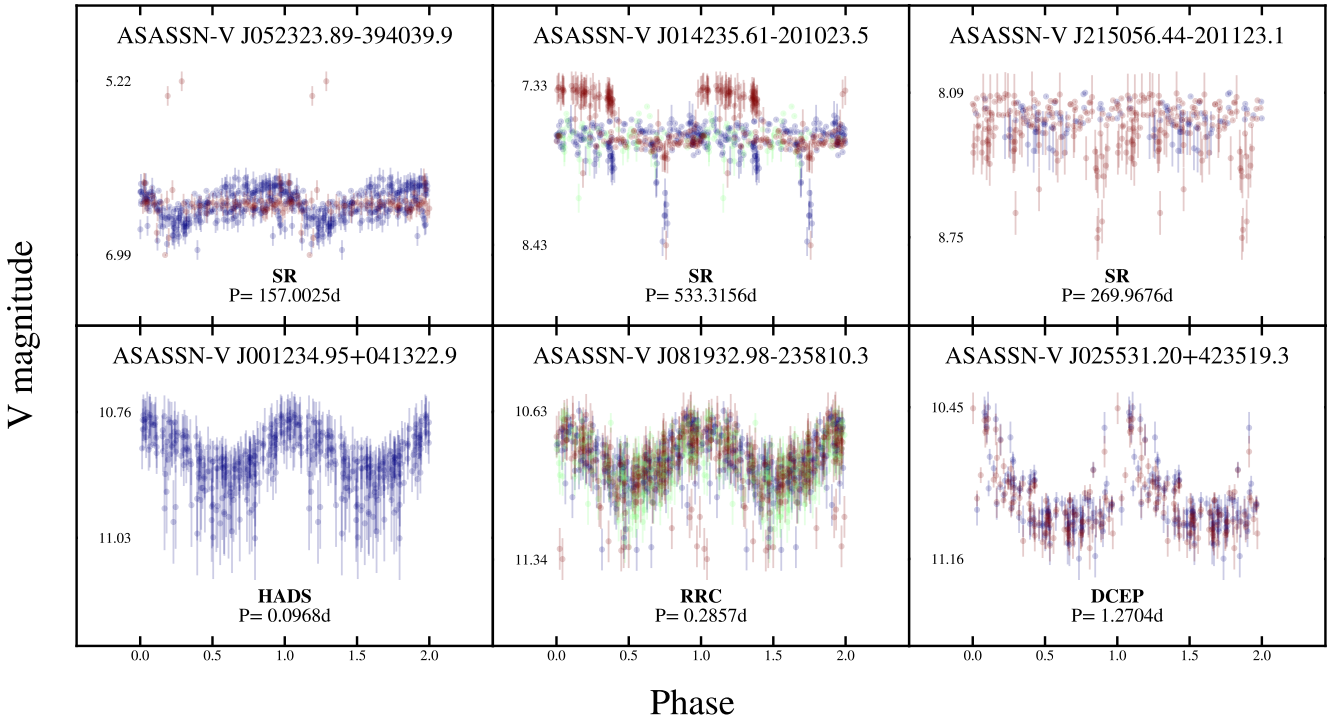

Figure A1. Examples of periodic variables in the saturated regime ($V < 11$ mag). The format is the same as Figure 8.

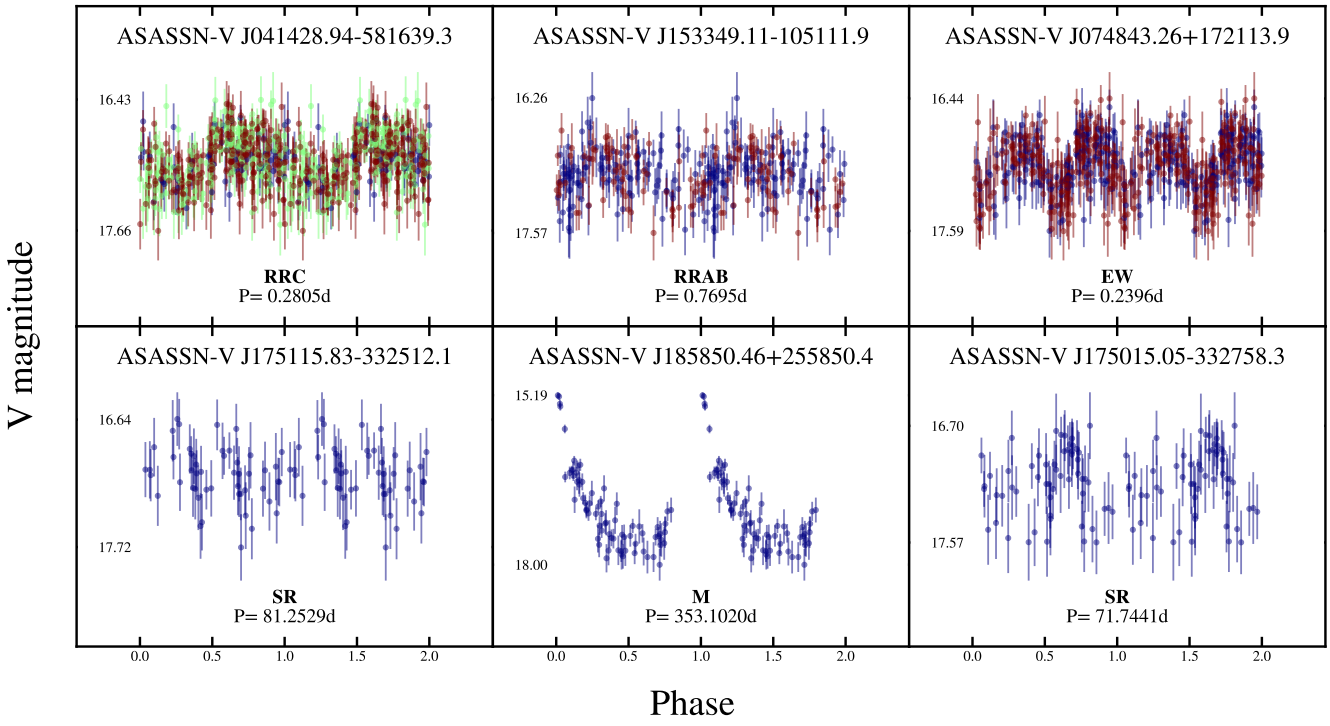

Figure A2. Examples of periodic variables with mean magnitude $V > 17$ mag. The format is the same as Figure 8.